UNIVERSIDAD COMPLUTENSE DE MADRID

FACULTAD DE CIENCIAS FÍSICAS
Departamento de Física de la Tierra, Astronomía y Astrofísica II
(Astrofísica y Ciencia de la Atmósfera)

TESIS DOCTORAL

Formation and evolution of galactic bulges: the importance of secular processes

Formación y evolución de bulbos galácticos: la importancia de los procesos seculares

MEMORIA PARA OPTAR AL GRADO DE DOCTOR

PRESENTADA POR

Raúl Cacho Martínez

Directora
Patricia Sánchez Blázquez

Madrid, 2016

Formation and evolution of galactic bulges: the importance of secular processes.
Formación y evolución de bulbos galácticos: la importancia de los procesos seculares

DOCTORAL THESIS

Raúl Cacho Martínez

FACULTAD DE CC. FÍSICAS
Departamento de Astrofísica y CC. de la Atmósfera

Madrid, November 2015

Formation and evolution of galactic bulges: the importance of secular processes.
Formación y evolución de bulbos galácticos: la importancia de los procesos seculares

Directed by:
Dra. Patricia Sánchez-Blázquez
Ramón y Cajal Researcher
Departamento de Física Teórica
Universidad Autónoma de Madrid

Memoria de tesis presentada por D. Raúl Cacho Martínez para aspirar al grado de Doctor en Astrofísica
Report submitted by Mr. Raúl Cacho Martínez for the Ph. D. in Atrophysics

FACULTAD DE CC. FÍSICAS
Departamento de Astrofísica y CC. de la Atmósfera

Madrid, November 2015

A Claudia

If my calculations are correct,
when this baby hits 88 miles per hour,
*you're gonna see some serious s****
D. E. Brown

Acknowledgements

El trabajo desarrollado durante estos últimos años y que da lugar a esta Tesis Doctoral ha supuesto un gran esfuerzo individual que no habría sido realizado sin la ayuda y el apoyo de muchas personas a mi alrededor.

En primer lugar, la Dra. Patricia Sánchez Blázquez, cuya supervisión, consejos y saber hacer han sido fundamentales para la obtención de los resultados científicos en esta memoria. También quiero agradecer la claridad de ideas que siempre ha tenido y que han llevado a buen puerto esta Tesis Doctoral. No menos importante es el papel del catedrático Javier Gorgas. Ambos me brindaron la oportunidad de pertenecer a su proyecto y desarrollar este trabajo. El apoyo de ambos ha sido siempre incondicional, con intensas conversaciones científicas, en las que su experiencia y conocimiento han sido imprescindibles.

También quiero agradecer su apoyo a todos los estudiantes de doctorado con los que he compartido esperanzas y desesperanzas doctorales durante este tiempo en el departamento. Gracias a vosotros he crecido como persona y como científico, compartiendo aficiones, gustos y, siempre, aprendiendo de vosotros. Dentro de este grupo quiero destacar a Jaime Izquierdo, Cristina Catalán Torrecilla y Alejandro Sánchez de Miguel, mis compañeros de despacho, con los que estas conversaciones han sido más frecuentes. Pero también muy enriquecedora ha sido la experiencia con Raffaella Marino, Lucía Rodríguez Muñoz, Néstor Espino Briones, Alexandre Bouquin, Belén Alcalde Pampliega, Magdalena Hernán Obispo, Miguel Ángel López García, Javier Alonso Floriano, Miriam Cortés Contreras, Víctor Pereira Blanco, Hugo Tabernero Guzmán, Carlos Gómez Guijarro, José Manuel Martín Hernández, Francisco Ocaña González y Carlos Tapia Ayuga.

No quiero olvidarme del apoyo recibido desde el primer momento por parte de todo el departamento de Astrofísica. Empezando por los postdocs Sergio Pascual, Carmen Eliche, Víctor Villar, Pilar Esquej, Helena Domínguez, Antonio cava, Jose Antonio Caballero, Javier López... Todos ellos, en mayor o menor medida, me han ayudado a finalizar con éxito este trabajo. Desde el primero hasta el último de los profesores de este Departamento

me han mostrado siempre su apoyo, y siempre con una sonrisa. A los catedráticos D. Javier Gorgas, Da. Mł José Fernández Figueroa, y Da. Elisa de Castro, y al resto de profesores no mencionados aun, D. Jaime Zamorano, D. Jesús Gallego, D. Nicolás Cardiel, D. Armando Gil de Paz, D. Pablo Pérez González, Da. África Castillo Morales y D. David Montes, sin olvidarme de los recientemente jubilados D. Manuel Rego Fernández y D. Manuel Cornide Castro-Piñeiro.

Parte de esta tesis se ha desarrollado en el extranjero. Quiero agradecer todo su apoyo a la *Research School for Astronomy and Astrophysics of the Australian National University* por todos los medios que puso a mi disposición, y en particular al Dr. Kenneth C. Freeman y a su esposa, Da. Margaret Freeman por haberme hecho sentir como en casa durante mi estancia en Australia. En Chile, sin la infraestructura técnica y humana del *European Southern Observatory* no habría sido posible desarrollar el trabajo allí realizado; es mi deseo enfatizar el apoyo recibido por Dimitri gadotti, Juan Carlos Muñoz Mateos, Paulina Jirón y Claudio Melo.

Quiero agradecer al Ministerio de Ciencia e Innovación primero, y Ministerio de Economía y Competitividad el haberme proporcionado ayuda económica para la realización de esta Tesis Doctoral a través de la ayuda BES-2011-045248 enmarcada en los proyectos AYA2010-21322-C03-03 y AYA2013-48226-C3-3-P y por la ayuda a la movilidad EEBB-I-15-09395.

Quiero agradecer también a todo el grupo RAVET, por haberme hecho sentir uno más desde el principio, Alejandro Vazdekis, Jesús Falcón Barroso, Reynier Peletier, Vicent Quilis, Santos Pedraz, Javier Cenarro, Carlos Allende, Elisa Toloba, Adriana de Lorenzo Cáceres Anna Ferré Mateu, Esther Mármol, Ignacio Martín Navarro, Marja Seidel, Jairo Méndez Abreu...

Por supuesto, guardo un rinconcito para todos aquellos nuevos amigos en la Winter School 2011 en Tenerife. Me olvidaré de muchos, pero quiero destacar a Tomás Ruiz Lara (y a su directora, Isabel Pérez), a Javier Blasco Herrera a Bruno Rodríguez del Pino, Marja Kristin Seidel...

En el ámbito personal, quiero agradecer a todos mis amigos, los cuales me apoyaron siempre a la hora de emprender esta aventura doctoral. Gracias a Gaspar, Benjamín, Aitor, Mario, Andrea, Iris, Héctor, Sergio...

Finalmente, quiero agradecer el apoyo de mi familia, mis padres Javier y Rosa, mi abuela Delfina, mi hermano Jorge y todos mis tíos y primos. Por supuesto un lugar especial lo tiene Claudia que estos últimos 8 años ha sido mi mayor apoyo y uno de los motivos para seguir adelante.

Muchísimas gracias a todos por haberme animado y apoyado. Sin vosotros este trabajo no habría sido terminado, y yo no sería la persona que soy. gracias de todo corazón.

Resumen

0.1. Objetivos

El objetivo principal de este trabajo es entender la formación y evolución de los bulbos de galaxias. Enfrentamos este problema desde diferentes puntos de vista, cumpliendo metas parciales:

- El análisis comparativo entre galaxias barradas y no barradas procedente de una muestra de galaxias tomadas del *Sloan Digital Sky Survey* nos permitirá entender las diferencias (si las hay) acerca de cómo las galaxias barradas y no barradas forman sus bulbos.
- Los bulbos en las galaxias están formados por diferentes componentes estelares, cada una de ellas con diferentes propiedades (edad, metalicidad y cinemática). Estas porpiedades vienen determinadas por los procesos físicos que dieron lugar a su formación, los cuales queremos entender.
- Para profundizar en el análisis de estas subcomponentes, intentaremos desentrañar las componentes estelares de los bulbos a partir de los espectros integrados. Para ello debemos desarrollar una nueva técnica que nos permita obtener la cinemática, la edad y la metalicidad de cada una de las componentes que contribuyen al bulbo.

0.2. Metodología

La comparación entre galaxias barradas y no barradas se realiza tanto desde el punto de vista del gas como desde el punto de vista estelar. Para el gas se calculan las metalicidades, utilizando un proceso iterativo que combina diferentes cocientes de líneas de emisión (este método está descrito en profundidad en Kewley and Dopita, 2002). La metalicidad estelar se calcula por medio de síntesis espectral. En particular usamos el código `STECKMAP`

(Ocvirk et al., 2006a,b), que describimos en el Apéndice A. Comparamos los resultados obtenidos con este código con uno de lo procedimientos más empleados en la literatura, `STARLIGHT` (Cid Fernandes et al., 2005) y con los obtenidos con métodos clásicos de comparación de características espectrales con poblaciones estelares simples (Worthey et al., 1994).

Para profundizar en este análisis, desarrollamos una técnica para descomponer, simultáneamente, la cinemática, la edad y la metalicidad de las poblaciones estelares que componen los bulbos, sin asumir *a priori* el número de poblaciones que los forman.

0.3. Resultados

Comparamos la metalicidad entre galaxias barradas y no barradas. Encontramos que las galaxias barradas, en promedio, son ligeramente más ricas en metales que las no barradas. Sin embargo, estas diferencias no son siginificativas si consideramos galaxias de la misma masa. Un análisis más profundo revela que, aunque la metalicidad del gas no es diferente en galaxias barradas y no barradas, las propiedades físicas sí lo son, al encontrar valores superiores para el parámetro de ionización y para la tasa de formación estelar por unidad de masa en galaxias barradas.

Realizamos un estudio de las poblaciones estelares utilizando datos de espectroscopía de campo integral en tres galaxias con bulbos de diferentes complejidades: NGC5701, NGC6753 y NGC7552. El análisis de poblaciones estelares desvela que diferentes morfologías están ligadas a diferentes historias evolutivas. Sin embargo la muestra utilizada es pequeña y no es suficiente para obtener conclusiones estadísticas. Gracias a este análisis también podemos determinar que, a pesar de las diferencias en las características de los tres bulbos analizados, todos tienen en común que formaron, al menos, un 50 % de su masa hace 10 Gyr.

Desarrollamos una técnica para la descomposición de diferentes poblaciones estelares (en función de su cinemática, edad y metalicidad) subyacentes en el espectro integrado de estas tres galaxias. Aplicando esta técnica recuperamos las poblaciones del bulbo para las tres galaxias, estando este formado por dos componentes con propiedades diferentes en NGC5701 y NGC6753. Para NGC6753 y NGC7552 también obtenemos poblaciones sustentadas por rotación, no apareciendo esta población en NGC5701. En esta descomposición también obtenemos información acerca de las poblaciones jóvenes, destacando una espiral nuclear en NGC5701, y anillos de formación estelar en NGC6753 y NGC7552.

Gran parte del trabajo de esta tesis está basado en el uso de modelos de poblaciones estelares, basados en librerías estelares. Una de las librerías más populares es MILES, que, siendo una biblioteca empírica, su cobertura está limitada a estrellas de la vecindad solar. Seleccionamos y observamos una muestra de estrellas para ampliar la cobertura del diagrama [Mg/Fe]-[Fe/H]. Hemos llevado a cabo la reducción de estas estrellas y, actualmente, se están calculando sus parámetros estelares para ser incluidas en una futura extensión de la librería estelar MILES.

0.4. Conclusiones

- Demostramos que las barras contribuyen a la evolución de las galaxias, transfiriendo masa a los centros de las galaxias y redistribuyendo momento angular. Sin embargo esta contribución es menor que la predicha por las simulaciones
- A pesar de que las barras transfieren material, y aumentan la eficiencia de la formación estelar, las galaxias barradas no muestran propiedades centrales significativamente diferentes que las galaxias no barradas.
- Como parte de este análisis, comparamos nuestros resultados con resultados obtenidos por otros autores. Gracias a ello encontramos que las diferencias entre diferentes estudios pueden deberse tanto a efectos de selección de la muestra como a diferencias procedentes de los métodos utilizados.
- Encontramos que, al menos el 50 % de la masa de las galaxias está formada por estrellas con una edad superior a 10 Gyr, lo cual sirve de cota a los modelos de evolución de galaxias.
- Se ha desarrollado una técnica nueva para descomponer los bulbos en sus componentes, siendo capaces, por primera vez, de caracterizar simultáneamente la edad, metalicidad y cinemática de cada una de ellas. Gracias a ello podremos determinar la importancia de diferentes procesos físicos en la formación de bulbos galácticos, una vez aplicada a una muestra completa de galaxias.
- Se ha contribuido a la ampliación de la biblioteca estelar MILES con la observación y reducción de un 25 % de estrellas nuevas, dedicadas a aumentar la cobertura de [Mg/Fe] a diferentes metalicidades. Esto permitirá, por primera vez, obtener modelos de poblaciones estelares con diferente [Mg/Fe] basados completamente en librerías empíricas y

testear aquellos modelos basados en librerías construidas con modelos de atmósferas.

Summary

0.5. Objectives

The main goal of this work is to understand the formation and evolution of galactic bulges. We face this problem from different points of view, achieving partial objectives:

- The comparative analysis between two samples of barred and unbarred galaxies from the *Sloan Digital Sky Survey* (SDSS) will allow us to understand the differences (if exist) about how barred and unbarred galaxies form their bulges.
- Bulges in galaxies are formed by different stellar components, each one with different properties (age, metallicity and kinematics). These properties are determined by the physical processes which gave place to their formation, which we want to understand.
- For a better comprehension of these subcomponents, we will try to disentangle the stellar populations in bulges from their integrated spectrum. To do this we have to develop a new technique which will allow us to derive the kinematics, age and metallicity of each individual components contributing to the bulge.

0.6. Methodology

The comparison between barred and unbarerd galaxies is performed taking into account both, the gas and stellar populations. The metallicity of the gas is calculated using an iterative process which combines different emission line ratios in (this method is described in detail in Kewley and Dopita, 2002). The stellar metallicity is derived by means of full spectral fitting. In particular we use the code `STECKMAP` (Ocvirk et al., 2006a,b), described in Appendix A. We compare the results with one of the most used procedures in

the literature, (`STARLIGHT, Cid Fernandes et al., 2005`) and with those obtained with classical methods of comparison of spectral features with single stellar populations (Worthey et al., 1994)

For a deeper analysis we develop a technique to decouple, simultaneously, the kinematics, the age and the metallicity of the stellar populations which form the bulges, without assuming *a priori* the number of stellar population contributing to them.

0.7. Results

We compare the metallicity between barred and unbarred galaxies. We find that, on average, barred galaxies are slightly more metal rich than unbarred galaxies. However, these differences are not statistically significant if we consider galaxies with the same stellar mass. A deeper analysis reveals that, despite the metallicity of the gas is the same in barred respect to unbarred galaxies, the physical properties are different, finding higher values for the ionization parameter and for the star formation rate per unit mass in barred galaxies.

We perform a study about the stellar populations using integral field spectroscopy data in three galaxies with bulges of different complexities: NGC5701, NGC6753 and NGC7552. The analysis of the stellar populations unveils that different morphologies are linked to different evolutionary histories. However, our sample is small to obtain statistical conclusions. With this analysis we also determine that, despite the differences in the properties of the three analysed bulges, all of them have in common that they formed, at least, 50 % of their mass more than 10 Gyr ago.

We develop a technique for the decomposition of different stellar populations (each one with its own kinematics, age and metallicity) underlying the integrated spectra of these three galaxies. With this technique we recover the populations in the bulge for the three galaxies, being this formed by two components with different properties in NGC5701 and NGC6753. For NGC6753 and NGC7552 we also obtain rotationally-supported populations, which does not appear in NGC5701. In this decomposition we also obtain information about the young populations, in particular a nuclear spiral in NGC5701 and star forming rings in NGC6753 and NGC7552

A large part of this work is based on stellar population models, based on stellar libraries. One of the most popular stellar library is MILES that, being an empirical library, is limited to stars observable from the Earth. We select a sample of stars with parameters covering empty spaces in the [Mg/Fe]-

[Fe/H] diagram. These stars were observed in two campaigns in 2011. We have reduced the data of these stars and, at present, their stellar parameters are being derived, in order to be included in a future extensin of the MILES stellar library.

0.8. Conclusions

- We demonstrate that bars contribute to the evolution of galaxies, transferring mass to the centres of galaxies and redistributing angular momentum. However, this contribution is smaller than simulations predict.
- Despite this transfer of mass, and the higher efficiency in forming stars, barred galaxies do not show significantly different central properties compared to unbarred galaxies.
- As part of this analysis we compare our results with the results obtained by other authors. We find that the differences among studies may owe to both selection effects and differences arising from the different methodologies.
- We find that, at least 50 % of the stellar mass was formed more than 10 Gyr ago, which is a constrain to galaxy evolution models.
- We develop a new technique for decomposing the bulges in their components, being able, for the first time, of characterizing simultaneously, the age, metallicity and kinematics of each component.Thank you to this we can determine the importance of the different physical processes in the formation of galactic bulges, once applied on a full sample of galaxies.
- We contribute to the extension of the MILES stellar library with the observation and reduction of 25 % of new stars, devoted to improve the coverage in [Mg/Fe] at different metallicities. This will allow, for the first time, to obtain stellar population models with different [Mg/Fe] completely based on empirical libraries, and to test models based on libraries built on stellar atmospheres models.

Index

List of Figures

List of Tables

Chapter 1

Introduction

Bulges are one of the most prominent structure in galaxies, contributing sometimes to a large fraction of its total flux. Therefore, the analysis of these structures is necessary to understand the evolution of the whole galaxy. These structures, considered as the deviation from the exponential profile in the centre of a galaxy, seem to be one of the keys to understand galaxy evolution processes (*e.g.,* Ferrarese and Merritt, 2000; Gebhardt et al., 2000). Yet, the details of their formation remains unsolved.

We distinguish different classes of bulges attending to their morphology and their kinematical and structural properties. *Classical bulges* are those which have kinematic and photometric properties following the fundamental plane of elliptical galaxies (*e.g.,* Athanassoula, 2005; Fisher and Drory, 2008; Gadotti, 2009; Fisher and Drory, 2010). They are believed to have formed via dissipative collapse at early times, by the merge of giant clumps in the early stages of disc formation, via minor accretion events or by major mergers. We also distinguish observationally bulge structures that follow more disc-like properties. These bulges are believed to have formed slowly through internal processes (*i.e.*, through secular evolution. *e.g.* Simkin et al., 1980; Pfenniger and Friedli, 1991; Hopkins et al., 2010) and are sometimes called *pseudo-bulges*. Recent works also propose the formation of these type of bulges by the secular accretion of satellites into the galaxy disc (Eliche-Moral et al., 2011). Athanassoula (2005) proposes a third type of central structures, those with a boxy/peanut morphology that would correspond to the central part of a bar see edge-on. However, all types of bulges can coexist and the observed properties sometimes depend on the geometry chosen to derive the bulge properties (Obreja et al., 2013; Fisher and Drory, 2008; Peletier et al., 2007; Méndez-Abreu et al., 2014). In this case, the different components of the bulge will have different kinematics, ages and metallicities, as they form in

different ways. The problem then lies in the lack of a knowledge of how much of their properties are due to secular or to fast processes, both of which could have external or internal causes.

Bars are believed to be the main agents building *pseudobulges*. Bar torques on the gas can make it to lose angular momentum and flow to the centre, where stars can be formed. Numerical simulations predict that this mechanism is very efficient at producing central structures that retain kinematical properties of a disc (Kormendy and Kennicutt, 2004; Cheung et al., 2013). Observationally, one would expect then to see that barred galaxies have central gas fractions and star formation rates. If this mechanism operates for long timescales then we would also expect higher central metallicities on both, gas and stars. Observational studies, however, do not see these differences clearly and there is still considerable controversy (*i.e.* Henry and Worthey, 1999; Dutil and Roy, 1999; Considère et al., 2000; Ellison et al., 2011).

The main sources of the discrepancies are due to differences in the sample selection. Furthermore, much of recent observational effort to understand the nature of bulges has been placed in determining the stellar properties of the bulge, their variation with radius and the comparison of these stellar properties with those of the discs (*e.g.* Prugniel and Soubiran, 2001; Proctor and Sansom, 2002; Sil'Chenko, 2004; Moorthy and Holtzman, 2006; Morelli et al., 2008; Peletier et al., 2007; Jablonka et al., 2007; Ganda et al., 2007; MacArthur et al., 2009; Pérez et al., 2009; Sánchez-Blázquez et al., 2009, 2014; Pérez and Sánchez-Blázquez, 2011; Williams et al., 2012; Coelho and Gadotti, 2011). These studies have revealed that bulges are not simple systems and that they, in many cases, host different subcomponents. An analysis of the different kinematic populations is needed to comprehend the origin of how bulges (and galaxies) form and evolve. It is difficult to obtain a reliable determination of how many components co-live spatially in the bulge from integrated spectra where both the kinematics and the stellar properties of the different components are coupled. Recently, inversion algorithms (*e.g.* STARLIGHT: Cid Fernandes et al. 2005; STECKMAP: Ocvirk et al. 2006a,b; FIT3D: Sánchez et al. 2006; ULySS: Koleva et al. 2009) have been developed to perform full-spectral fitting to the data comparing it with a set of synthetic model spectra for a range of ages and metallicities. These codes are a new approach to analysing stellar properties in complex systems and could be potentially used to decouple different kinematic components. Some attempts to break this problem have been proposed using examples where some *a priori* knowledge of the system existed and/or a number of sub-populations was assumed, for instance counter-rotating discs (Coccato

et al., 2013). Ocvirk et al. (2008) also used full spectral fitting to disentangle the kinematics and ages of the disc and bulge components in NGC4030. They allowed each population to have their own kinematics, but the metallicity was fixed, which can bias the age due to the age-metallicity degeneracy. These previous studies assumed that only two different populations in the galaxy could be distinguished.

Stellar population studies of bulges date back to the 90's. The first photometric studies (Balcells and Peletier, 1994; Hernquist, 1990; Terndrup et al., 1994; Peletier and Balcells, 1996; de Jong, 1996; Trager et al., 2000; Bell and de Jong, 2000, among others) concluded that the colour of the bulge is related to the global properties of galaxies (like luminosity, or mass). In fact, the bulges in early-type galaxies have similar colors (esentially red) than elliptical galaxies. As a consecuence of this, bulges were thought to have similar properties to that of elliptical galaxies (Sansom et al., 1998; Proctor and Sansom, 2002).

Also from the 90's are the first spectroscopic studies of bulges. The comparison of Lick/IDS indices (Gorgas et al., 1993; Worthey et al., 1994) with the central velocity dispersion (σ_c, as a proxy of the stellar mass of the galaxy) confirmed that the stellar population properties of bulges in early-type galaxies are similar to elliptical galaxies (Bender et al., 1993; Fisher et al., 1996; Idiart et al., 1996). An index is a measurement of the depth of an absorption line which traces a particular feature of the stellar population (age, metallicity, abundances of individual chemical elements...). This is done by defining the region where the absorption line is and two adjacent regions where a stellar *pseudocontinuum* is measured[1]. While several sets of indices exist, the most used are the Lick/IDS indices system (Faber et al., 1985; Worthey et al., 1994; Worthey and Ottaviani, 1997) which consists in 25 indices defined in the optical range. These indices (or, more specifically, a combination of them) allows to estimate simultaneously the average age and the metallicity of the stellar populations contributing to a spectrum. One of the main problems concerning the analysis of stellar populations is that, in the integrated light of a single age, single metallicity stellar population, an age change can be countered by a metallicity change so that almost every colour and spectral index remain the same. This is known as the age-metallicity degeneracy.

Other problem in the study of bulges are the effects of extinction by dust and the emission lines from ionized gas. The extinction changes the observed color and depends on the inclination, while emission lines (in particular those

[1]It is not a real continuum as the side pass bands are used to calculate a straight line estimating the level of the continuum in the central band.

from HII) affect the Balmer absorption features, which are the best tracers of the age of the stellar populations.

These results are obtained for early type galaxies (T-type[2]<4) to minimize the already mentioned effects of gas, dust and inclination. The similarity between bulges and early-type galaxies may obey to this selection effects.

In the last fifteen years, bulges in late type galaxies have been included in the samples. In particular, a comparison of the central velocity dispersion with indices sensitive to variations in Mg show differences between bulges and elliptical galaxies if late-type bulges are included. These differences appear as a different relation between Mg and σ_c in bulges than in E-S0 galaxies (Prugniel and Soubiran, 2001; Chiappini et al., 2002; Ganda et al., 2007; Morelli et al., 2008), different slopes of this relation (Falcón-Barroso et al., 2002) or larger scatter in this relation in bulges than in ellipticals (Moorthy and Holtzman, 2006; Peletier et al., 2007). These discrepancies can be explained by different reasons:

- Differences in the mass distribution. Fig. 1.1 shows Mgb$'$ and Hβ' as a function of σ_c for two samples of galaxies, one with E, S0 and Sa galaxies in SAURON sample and other with late-type galaxies from Ganda et al. (2007). The relations for early- and late-type galaxies appear to be parallel, but the differences can be due to differences in the central velocity dispersion (Thomas et al., 2005).

- When comparing low-mass (usually late-type) bulges with the Mg-σ relations obtained by massive elliptical galaxies, an offset exists. This offset can be removed considering the missing rotational support expected in these late-type bulges. As the rotational support of some bulges increases, the measured velocity dispersion is no longer a reliable tracer of their motion.

- Peletier et al. (2007) studied the Mg-σ relation obtained by different authors (Fig. 1.2) concluding that the scatter is much larger in low inclination samples. They showed that the reason for this was that, when present, young components are located in flattened discs or rings that cannot be seen in high-inclined samples.

[2]Morphological classification in the Hubble sequence, which spans from -6, for E galaxies, to 10 for irregular galaxies, with 4 corresponding to Sbc, following the classification by de Vaucouleurs (1959)

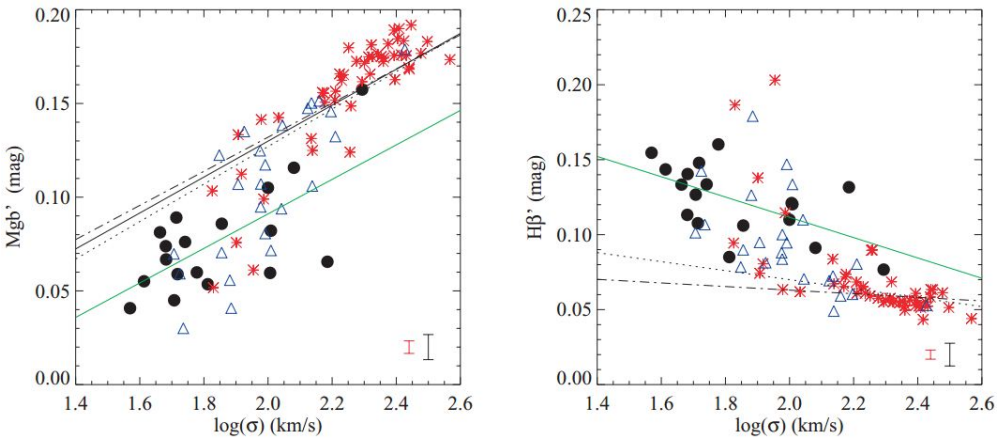

Figure 1.1: Figure taken from Ganda et al. (2007).Indices Mgb′ and Hβ' as a function of σ_c for a sample of E to Sa galaxies (asterisks and triangles) in the SAURON sample and a sample of late-type galaxies from Ganda et al. (2007) (black circles). Black solid lines represent the predictions for these relations found by Jorgensen et al. (1996), dotted and dash-dotted lines represent the predictions for low and high density environments by Sánchez-Blázquez et al. (2006a), and the green line the fit to the black circles by Ganda et al. (2007).

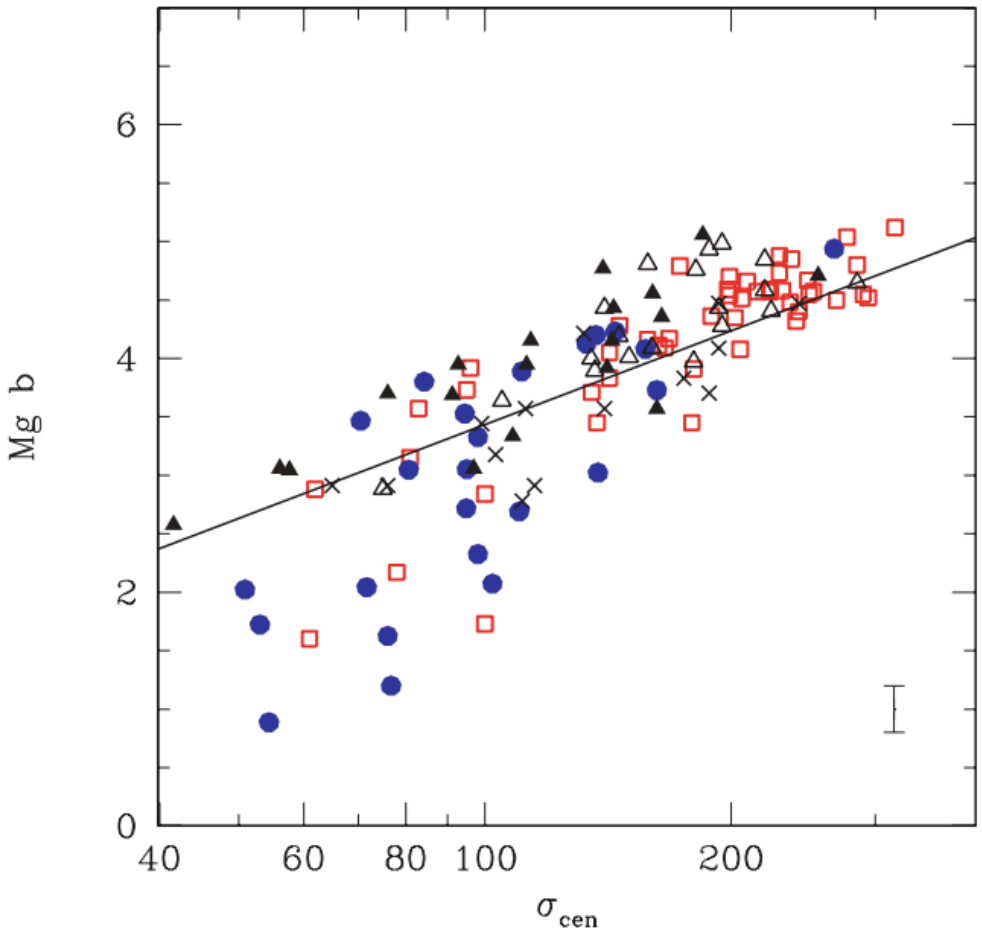

Figure 1.2: Figure taken from Peletier et al. (2007). Indices Mgb′ and Hβ' as a function of σ_c for a sample of E to Sa galaxies (asterisks and triangles) in the SAURON sample and a sample of late-type galaxies from Ganda et al. (2007) (black circles). Black solid lines represent the predictions for these relations found by Jorgensen et al. (1996), dotted and dash-dotted lines represent the predictions for low and high density environments by Sánchez-Blázquez et al. (2006a), and the green line the fit to the black circles by Ganda et al. (2007).

1.1. Classical bulges and pseudobulges

Bulges are now understood as complex structures, formed not only in the early stages of galaxies, but in a continuous evolution and formation from different sources, like *in situ* star formation, mass redistribution by bars (or other axisymmetric components) or stellar accretion of both satellites and stars from the outskirts of galaxies passing nearby.

These three types of bulges can coexist in the same host galaxy. This complicates tremendously the analysis and characterization of bulges.

The study of resolved stellar populations is the ideal technique to disentangle these subcomponents in galactic bulges and to quantify the contribution of each one to the total mass of the bulge. However, this can only be done for a few galaxies in the Local Group (Tolstoy et al., 2009; Frebel et al., 2010). An alternative is to use the integrated light of galaxies.

Photometry (using wide or narrow-band filters, colours or a combination of them) allows to observe different substructures by decomposing the light profiles in several components (de Souza et al., 2004; Laurikainen et al., 2007), characterize stellar populations (Bell and de Jong, 2000; MacArthur et al., 2004; Gadotti and de Souza, 2006; Muñoz-Mateos et al., 2007; Roediger et al., 2012) and even associate star formation rates and masses to different types of bulges (Fisher and Drory, 2011). These techniques also allow to associate the stellar properties to different regions in the galaxy.

Spectroscopy, in addition, allows to determine kinematical properties (Falcón-Barroso et al., 2006; Ganda et al., 2006) and how stellar populations distribute in these galaxies (Trager et al., 2000; Kuntschner, 2000; MacArthur et al., 2009; Sánchez-Blázquez et al., 2011). This is the approach we use in the analysis of galactic bulges. The advantage of spectroscopy against photometry is the posibility of breaking degeneracies (for example, among extinction, ages, metallicities, kinematics...) and the derivation of relative abundances. Also a better analysis of emission and absorption features can be performed, as they can be separated easily using the information of the stellar continuum in the regions where no emission liens are present.

The increase of computational power of desktop computers, and the improvement of stellar libraries (e.g., STELIB, Le Borgne et al. 2003; MILES, Sánchez-Blázquez et al. 2006b, Vazdekis et al. 2010; Indo-US, Valdes et al. 2004) have impulsed the use of spectral synthesis. Spectral synthesis uses information from the whole spectrum, maximizing the use of information one can obtain with a given time at the telescope. This helps to minimize the effects of degeneracies (Sánchez-Blázquez et al., 2011). In the last decade, several groups have published software to extract the star formation history

and the age-metallicity relation of a galaxy using full spectral fitting. This inversion problem is very ill-conditioned (Moultaka and Pelat, 2000; Moultaka et al., 2004) and different codes follow different approaches to deal with this problem (among others, `STARLIGHT`, Cid Fernandes et al. 2005; `STECKMAP`, Ocvirk et al. 2006a,b; `FIT3D`, Sánchez et al. 2006; `ULySS`, Koleva et al. 2009).

1.2. Bars and secularly evolved bulges

Numerical simulations predict that bars are efficient transporters of matter (Weinberg, 1985; Debattista and Sellwood, 1998, 2000; Athanassoula, 2002; Berentzen et al., 2006) to the central regions of disc galaxies. Gas is supposed to be efficiently transported by bars. Models predict that this gas feeds central starbursts, increasing the metallicities of the gas and the stellar populations in the central regions of galaxies (Elmegreen, 1994; Knapen et al., 1995; Hunt et al., 1999; Jogee et al., 1999, 2005; Jogee, 2006). These processes can contribute to the formation of pseudobulges.

Different observational studies have attempted to confirm these theoretical predictions by comparing the star formation rate (SFR) and the central metallicity (usually of the ionized gas) of galaxies with and without bars. However, so far, the results are contradictory. For example, while some authors have observed higher SFRs in barred galaxies (Hummel et al., 1990; Martin, 1995; Hawarden et al., 1996; Huang et al., 1996; Ellison et al., 2011) a bar may not be the most important mechanism to enhance the star formation rate (Pompea and Rieke, 1990; Martinet and Friedli, 1997; Chapelon et al., 1999). The results for the metallicity of the gas in the central regions of galaxies are even more controversial. Henry and Worthey (1999) reported that the barred and non-barred galaxies have the same metallicity, at a given magnitude (M_B). Dutil and Roy (1999) and Considère et al. (2000), however, obtained lower metallicities (about 0.5 dex, at the same magnitude M_B) in barred galaxies than in unbarred or weakly barred galaxies. A more recent study, with a much larger sample of galaxies (Ellison et al., 2011), finds that barred galaxies are more metal-rich (~ 0.06 dex) than unbarred galaxies with the same stellar mass.

Compared to the number of studies focusing on the gas phase metallicity, there is a lack of studies worrying about the metallicity of the stars in the central parts of galaxies depending on the presence or absence of bars. Moorthy and Holtzman (2006) found evidence that, at a given velocity dispersion, the metallicity of stars in the central parts of barred galaxies is higher than that of non-barred galaxies. This result is consistent with the findings of Pérez and Sánchez-Blázquez (2011), although the differences are not statistically

significant in any of the studies. Coelho and Gadotti (2011) reported that the stellar metallicity at the centre of barred and unbarred galaxies are equivalent, but found significant differences ($\sim 4\sigma$, but only for the most massive bulges) in the age distributions of both subsamples.

1.3. Goals

The main goal of this work is to improve the understanding of how bulges grow and its link to the evolution of the galaxy. We face this problem from different points of view, and try to improve the tools and techniques for a better comprehension of these galaxy components.

The properties of the gas and stars in the central regions of galaxies is thought to be linked to its evolution. We study a large sample of barred and unbarred galaxies from Sloan Digital Sky Survey to understand the differences about how barred and unbarred galaxies build their bulges.

We try to understand the composition of bulges by studying the stellar components and their characteristics, like age, metallicity and kinematics. An analysis of the star formation history of the stellar populations in the bulges should help to understand its evolution and their formation processes.

We aim to developing a technique to extract the properties of these stellar populations and calculate the properties of each population in the bulge, obtaining simultaneously, for the first time, the age metallicity and kinematics of the stellar components of the bulge.

Most of our work is based in the use of stellar populations models. The stellar population models, while experiencing a large improvement in the las years, are still incomplete. In particular the stars in MILES (Sánchez-Blázquez et al., 2006b), from which the stellar population models are derived (Vazdekis et al., 2010), does not cover the whole range of metallicities. We improve the stellar library with more observations.

Chapter 2

Central metallicities in barred and unbarred galaxies

2.1. Introduction

As we mentioned in the introduction, in the absence of an interaction, the most effective mechanism for radial motions of gas (important for bulge growth) is likely to be the presence of a galaxy bar. Simulations predict that bars facilitate gas inflow, enhancing central star formation and metallicity (Friedli et al., 1994). Studies of the star formation rates and metallicities of barred galaxies have yielded complex results. For example, whilst many studies have found an increased star formation rate in barred galaxies (Hummel et al., 1990; Martin, 1995; Hawarden et al., 1996; Huang et al., 1996), bars are apparently neither required nor guaranteed to yield high star formation rates (Pompea and Rieke, 1990; Martinet and Friedli, 1997; Chapelon et al., 1999).

Similar controversies apply to the central metallicities, with some works finding higher metallicities in barred galaxies (Ellison et al., 2011), in unbarred galaxies (Considère et al., 2000) or no differences (Henry and Worthey, 1999). With respect to the stellar properties, there is more agreement among works, with hints of slightly higher metallicities in barred galaxies (Moorthy and Holtzman, 2006; Pérez and Sánchez-Blázquez, 2011). However, the differences found are small and not statistically significant. Apart from the differences in the metallicities, Coelho and Gadotti (2011) also found different age distributions in both subsamples.

In this Chapter we explore the differences in the metallicity between barred and unbarred galaxies in both, the gas and the stellar metallicities. We also analyse the differences in some other related properties, as the star for-

mation rate and the ionization parameter and in the age of the stellar populations. We also compare our results with previous works, trying to conciliate the results in the literature.

2.2. Sample selection

The sample was obtained from the catalog of Nair and Abraham (2010). This catalog contains a (visual) morphological classification for more than 14000 galaxies in the Sloan Digital Sky Survey (SDSS) with redshifts less than 0.1 and g-band magnitude lower than 16. Nair and Abraham (2010) determined the presence of a bar by a visual inspection of the images in the g-band and r-band. With this visual inspection, they catalogued the structures in galaxies, such as bars, (internal and external) rings, shells, etc.

From the galaxies available in this catalogue, we select disc and irregular galaxies, *i.e.*, those with a Hubble morphological type $T \geq -2$. In this study we consider only galaxies in which there are not dominant structures (apart from bars) which may interfere in the results, so we select only those galaxies that have code 0 (no bar), 2 (high bar), 4 (intermediate bar) and 8 (weak bar, although such bars are considered strong bars in other catalogues such as RC3).

The observation of bars (or the lack of them) is severely affected by the inclination of galaxies. To reduce this selection effect, the catalogue only includes slightly inclined galaxies, *i. e.* with an axial ratio $b/a \geq 0.4$ ($\sim 68°$; in Appendix C we will check the validity of this criterion), which also minimizes the contribution of the disc to the spectrum collected by the fibre of the instrument.

We take the fluxes of the emission lines from the OSSY (Oh et al., 2011) database. we have checked that the fluxes from this catalogue are well reproduced by measuring them in a subsample of galaxies (Florido et al., 2015, in preparation). The line fluxes in OSSY are measured using `GANDALF` (Sarzi et al., 2006). `GANDALF` is a softwre to fit, simultaneously, the stellar continuum and the emission lines, assuming the latter as Gaussians. The authors use as templates the MILES library of stellar populations (Sánchez-Blázquez et al., 2006b; Vazdekis et al., 2010). At the same time, the code corrects the spectrum from dust attenuation using the Balmer decrement.

Before doing any measurement, we checked if the results could be de-

pendent on the chosen database. One popular database is MPA/JHU data[1] (Tremonti et al., 2004). Both databases use spectra from the *data release* 7 (DR-7) of SDSS, but in the analysis of the spectra different models and codes for the continuum removal (MILES and `GANDALF` in OSSY and Bruzual and Charlot, 2003, in MPA/JHU) and different models to correct for dust attenuation (two componentes in OSSY by only one in MPA/JHU) are chosen.

Figure 2.1 shows a comparison between emission lines flux ratios used in different metallicity calibrations (for the ionized gas) in the two databases described previously. The panels on the left show that the ratios are in good agreement with lower dispersion than expected by uncertainties in the measurements of fluxes. To verify that the differences are the same for barred and non-barred galaxies we conducted Kolmogorov-Smirnov (KS, hereafter) tests comparing the residuals of the ratios respect to the line 1:1. Right panels show the distributions of the residuals and the probability that the differences between distributions arise from random effects (P-value) in a KS test. As can be seen, for every ratio, except for $\log([OIII]\lambda\lambda 4959,5007/[OII]\lambda 3727)$, the associated P-value is larger than 0.0027, which is associated to a significance level of 3σ[2]. This indicates that the distributions of the emission line ratios are the same in barred and non-barred, except for the already mentioned case of $\log([OIII]/[OII])$. This ratio is closely related to the ionization of the gas, which is higher in barred galaxies, as will be explained later.

In our sample, we only selected galaxies with a S/N greater than 3 (in OSSY) in the more intense emission lines (this is, [OII]λ3727[3], Hβ, [OIII]λ5007, Hα and [NII]λ6584) to ensure that the measurements are not dominated by noise. Because the observation of the [OII]λ3727 line is required in our selection, and due to the SDSS wavelength coverage, our sample is restricted to galaxies with $z \geq 0.02$.

It is well known that galaxies follow a mass-metallicity relation and that metallicity evolves with redshift (Pilyugin et al., 2013, and references therein). These effects may be stronger than the effect produced by the bar. If we want to study the differences induced by bars in the central properties of galaxies it is important that our sample of barred and unbarred galaxies show the same distributions in mass, redshift and morphological type. Also, inclination can modify the results, as the contribution of the disc can be higher for highly inclined galaxies.

The mass of the galaxies plays a key role in its evolution and, therefore,

[1] http://www.mpa-garching.mpg.de/SDSS/DR7/

[2] 3σ is the significance level chosen in this analysis

[3] This line is actually a doublet at 3726 and 3729, with a ratio 1:1

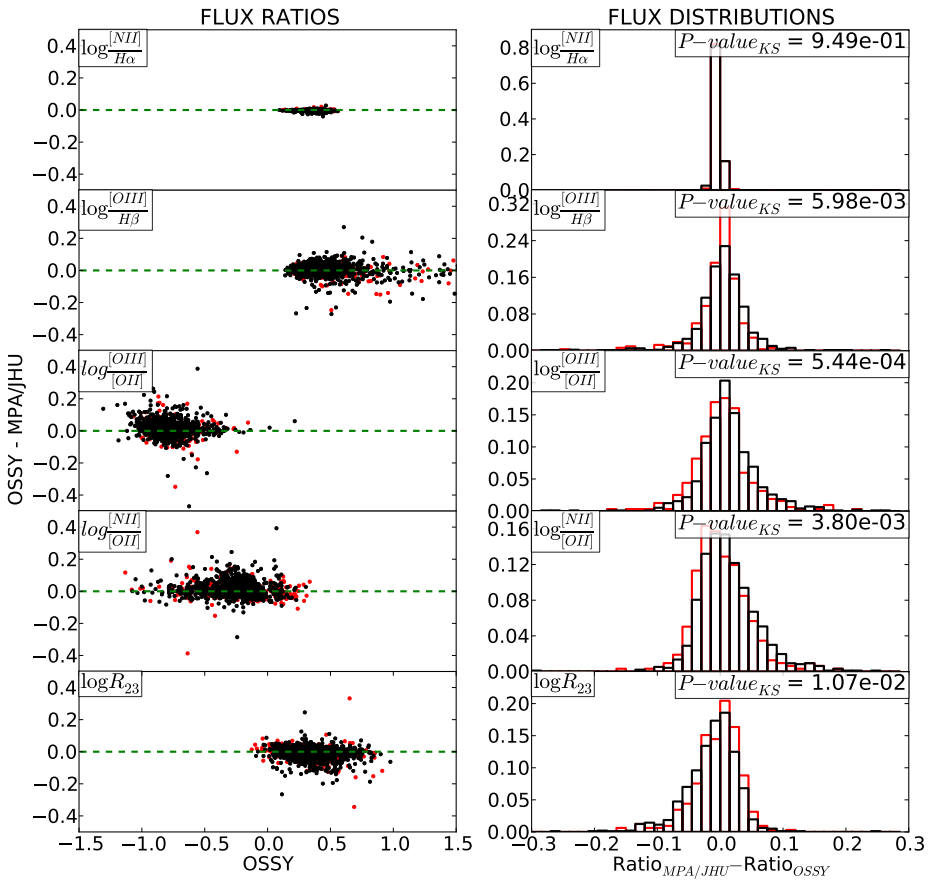

Figure 2.1: Left panels: comparison between flux ratios of the emission lines used in the calculation of the gas-phase metallicity in OSSY and MPA/JHU databases. On the right, the distributions of the differences between them and the P-values of the KS test on the distributions. From top to bottom, comparisons of $\log([NII]\lambda6584/H\alpha)$, $\log([OIII]\lambda\lambda4959,5007/H\beta)$, $\log([OIII]\lambda\lambda4959,5007/[OII]\lambda3727)$ y $\log(R_{23})$. Red color corresponds to barred galaxies and black to non-barred galaxies. The green line represents the line of equality in the values of both databases. The shadowed green region indicates the uncertainties in the differences between MPA/JHU and OSSy databases. As can be seen, the majority of the points are in this region, indicating that the scatter is within the uncertainties.

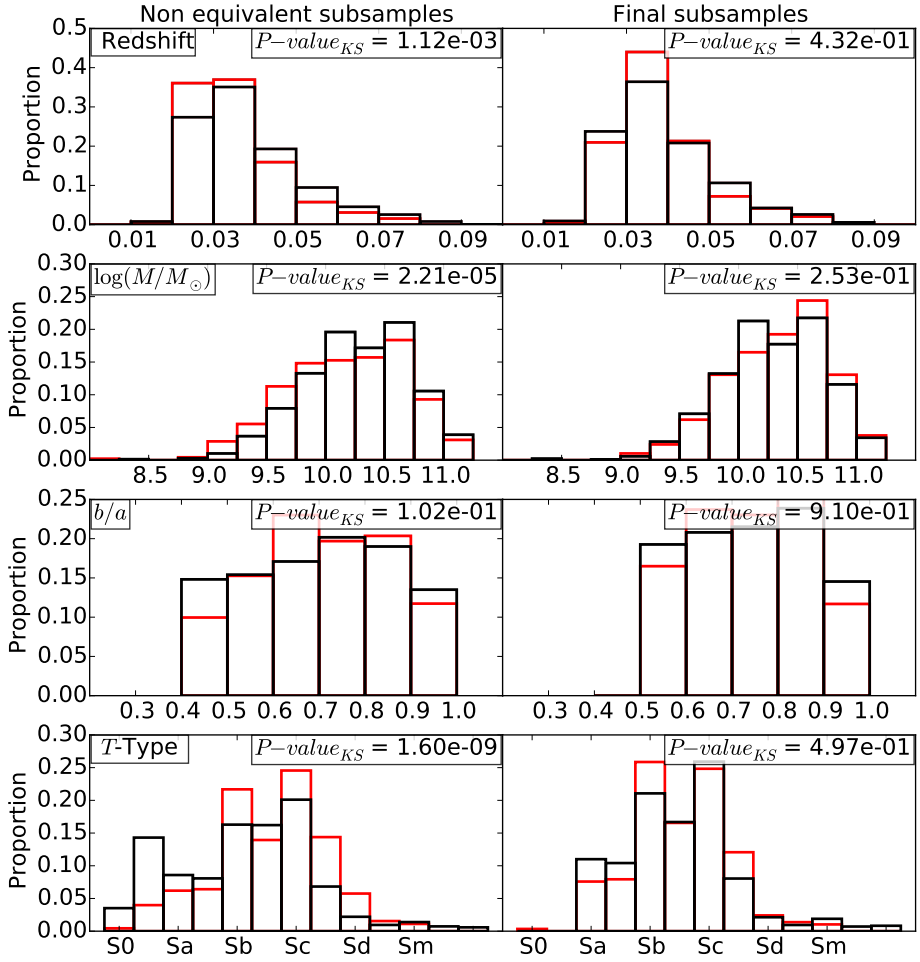

Figure 2.2: The left panels show the distributions of redshift, mass, axial ratio and morphological type for the original sample of galaxies, in which the distributions of barred galaxies (red) and galaxies barred (black) are not equivalent. The right panels show the same distributions for the final sample, after subtracting random galaxies, in which the distributions are compatible with each other, as indicated by P-values of the KS tests conducted to compare samples.

it is important to characterize them well. The masses of the galaxies in this study were taken from the catalogue of Nair and Abraham (2010), which, in turn, takes them from Kauffmann et al. (2003a), where stellar masses are calculated using a synthetic library of star formation histories and the indices D_n4000 (Balogh et al., 1999) y $H\delta_A$ (Worthey and Ottaviani, 1997). With these indices and comparing with the star formation histories library, a mass-luminosity ratio can be derived for each individual galaxy, with an uncertainty of $\sim 40\,\%$ for a confidence interval of $95\,\%$. Since the mass is an indirect measurement (obtained through the light), we check that the results are maintained using the luminosity of galaxies rather than mass as the independent variable.

Left panels in Fig. 2.2 show the distributions of the galaxy parameters after applying the selection criteria explained previously. The P-values of the KS tests comparing the distributions are also shown. These P-values are smaller than the significance level chosen for this analysis (3σ), so we consider that these distributions are not compatible with being taken randomly from the same sample. To homogenize the subsamples, we remove galaxies in a random way (but imposing the probability of a galaxy to be removed increasing if it lies in the regions of the histograms where the differences are larger). We repeat this process until the distributions are statistically compatible, as shown in the right panels in Fig. 2.2.

After applying the selection criteria and the elimination of galaxies explained in the preceding paragraph, we end up with 1594 galaxies, of which 414 are barred galaxies. This constitutes a $26\,\%$ of barred galaxies, which is the same percentage as in the original catalogue.

2.3. Analysis of the gas phase metallicity

The methodology used to calculate the metallicity of the gas phase is only applicable if the emission lines are produced by photoionization, so we must remove galaxies which contribution is (partially or totally) due to the emission by an active galactic nuclei (AGNs). To remove these galaxies we use a BPT diagram (named after the initials of its authors Baldwin, Phillips and Terlevich, 1981) in which [OIII]λ5007 is plotted *vs.* [NII]λ6584 (divided by Hβ and Hα respectively to avoid effects of extinction). Figure 2.3 shows the diagram for the galaxies in our sample, in which AGN and star forming galaxies are separated. Since this separation is diffuse, it is necessary to apply a separation criterion. The two most common criteria are those by Kauffmann et al. (2003b) and Kewley et al. (2001). Traditionally galaxies above and to the right of Kewley criterion are considered AGNs and those

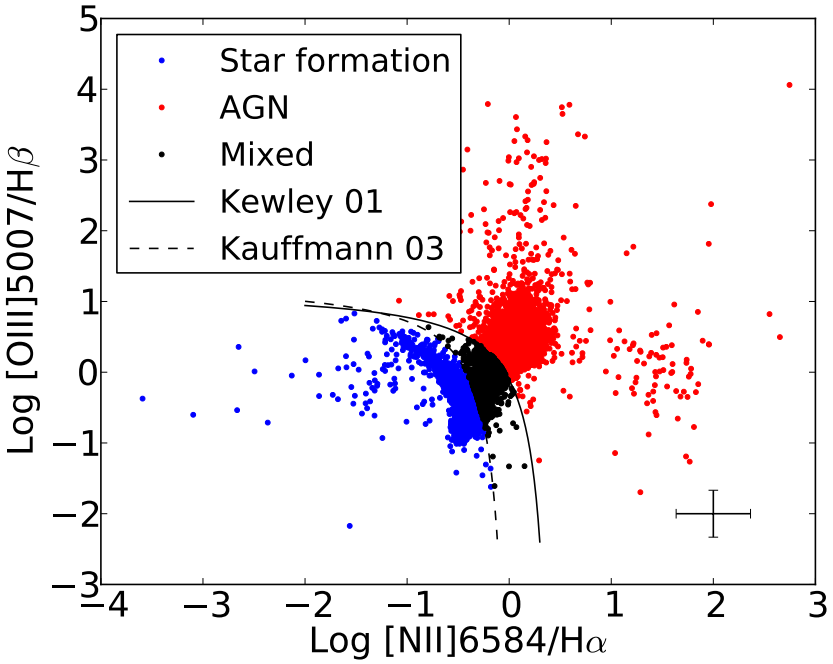

Figure 2.3: BPT diagram of all the galaxies in the sample. The solid line represents the Kewley criterion, while the dashed line represents the Kauffmann criterion (see text for details). These criteria divided AGN galaxies (red), composed galaxies (black) and pure star-forming galaxies (blue). Error bars show the typical uncertainties in the parameters represented.

below Kauffmann criterion are pure star-forming galaxies. Galaxies between both criteria are considered composite galaxies, whose emission lines derived from both photoionization and AGN. We decided to be restrictive and select those galaxies meeting the Kauffmann criterion.

To derive the metallicity of the ionized gas, we use the methodology based on R_{23} described in Kewley and Dopita (2002). R_{23} is a metallicity calibration based on hydrogen and oxygen lines, with the following expression:

$$R_{23} = \frac{[OII]\lambda 3727 + [OIII]\lambda\lambda 4959,5007}{H\beta}$$

We use the metallicity derived from R_{23} because it takes into account the ionization parameter, which, as will be discussed in section 2.5.4 is different for barred and unbarred galaxies. For the analysis of the discrepancies between previous studies we also compared the results using both calibrations in section 2.7.1.3

The calculation of the metallicity using R_{23} consists in an iterative process which comprises several steps:

- Using the ratio [NII]λ6584/[OII]λ3727 to obtain a first estimate of the metallicity, since the dependence of this ratio with the ionization parameter is low. The metallicity dependence of the [NII]/[OII] is due to the secondary nitrogen, *i.e.* nitrogen formed by stellar nucleosynthesis. For low metallicities (12 + log(O/H) $<$ 8.6), primary nitrogen (formed in the primordial nucleosynthesis) is dominant, and the measured metallicities in this range have very high uncertainties and this calibration can be used only as estimator in this region.

- With this first estimate of the metallicity and [OIII]λ5007/[OII]λ3727 the ionization parameter is calculated (q).

- We obtain the value of the metallicity using the coefficient R_{23} and interpolating the polynomials for this calibration in Kewley and Dopita (2002). R_{23} is bivaluated with the metallicity. To discriminate the range of high and low metallicities we use the value estimated in the first step.

- This new value of the metallicity is used to recalculate q. The iterative process is repeated until q and 12+log(O/H) converge to within 0.01 dex, which typically happens in one or two iterations.

This iterative process is applied to each galaxy several times for calculating uncertainties. In each of the executions the input values of the line ratios are slightly modified following a Gaussian distribution centred on the

calculated value and a width equal to the uncertainty of the parameter. This returns a distribution of output parameters (Z and q). The final values of metallicity and ionization parameter are considered as the average of the distributions, while we use as uncertainty the dispersion of the distribution.

2.4. Analysis of the stellar phase

For the calculation of the stellar population parameters, we use the code `STECKMAP` (Ocvirk et al., 2006a,b). `STECKMAP` is a Bayesian method that recovers, simultaneously, the kinematics and the stellar population properties. To do this it uses a *maximum a posteriori algorithm*. Whis method is not parametric, which means that no distributions are assumed for the line-of-sight velocity (LOSVd), the stellar age (SAD), the age-metallicity relation (AMR) or the mass-age relation (which are the outputs of `STECKMAP`). The only conditions are that these distributions have to be positive and smooth, in order to avoid high frequency oscilation qhich are not physical in most cases. `STECKMAP` minimizes the objective function, which is:
$Q_\mu = \chi^2(s(x, Z, g)) + P_\mu(x, Z, g)$,
where: x, Z, g are the SAD, AMR and LOSVd, respectively; s is the model spectrum fitting the data and P is a penalization function which is a linear combination of three penalization functions ($P_\mu = \mu_x P(x) + \mu_Z P(Z) + \mu_g P(g)$). This penalization functions (combined with the smoothing parameters μ_x, μ_Z, μ_g) result in higher values when the solutions are not smooth. Including these functions is equivalent to impose a Bayesian *prior* with a probabilty function: $f_{prior}(x) = e^{-\mu_x P(x)}$. More details about how `STECKMAP` works can be found in Appendix sA and in Ocvirk et al. (2006a,b); Sánchez-Blázquez et al. (2011).

From the star formation history (SFH) and the age-metallicity relation, we can obtain average values of age, velocity and metallicity weighting with the luminosity or with the stellar mass as `STECKMAP` also returns the contribution in mass of the stellar populations at each age. In our case, we use luminosity-weighted values, as they are more robust (see, for example Sánchez-Blázquez et al., 2011). To test the robustness of the result to the chosen software to calculate the SFHs we also calculate the stellar properties using `STARLIGHT` (Cid Fernandes et al., 2005). In Appendix B we show a comparison between the results obtained with each of the codes, but we can anticipate that, despite the differences in the mass-weighted values, luminosity-weighted values obtained with both codes are very similar and the differences compatible with the uncertainties. Appendix B also compare the spectral synthesis with the results obtained with Lick/IDS indices (Worthey

et al., 1994). The comparison here is not straightforward and we do not expect a 1:1 correlation. However, it is clear that there is a strong correlation between the two methods so, although the absolute values are not accurate, the relative values are comparable.

2.5. Results

2.5.1. Mass-metallicity relation

We fit the whole sample to a polynomial obtaining $-9.92 + 4.15x - 0.28x^2 + 0.0051x^3$ for the gas phase, and $-1.42 + 0.086x + 0.0025x^2$ for the stellar phase (with $x = \log M_*$). Fig. 2.4 shows the fits together with the relation obtained by Kewley and Ellison (2008) and Vale Asari et al. (2009) for comparison.

To study the possible differences between the two samples (barred and unbarred) we measure the differences with respect to these polynomial and compare the residuals.

We find that, on average, barred galaxies have a higher metallicity (0.02 dex) that unbarred galaxies, which is significant after a KS test between the distributions of the differences ($P-$value$=8.8\times10^{-5}$).

Some authors find that the amount of gas in barred galaxies is higher than in barred galaxies. This higher amount only happens for massive galaxies (Ho et al., 1997; Coelho and Gadotti, 2011). Therefore, the differences may exist only for massive galaxies. To explore this scenario we separate galaxies in mass intervals with a width $\Delta \log(M/M_\odot)$ =0.2. First we check (using KS tests) that barred and unbarred galaxies in each mass interval have the same distributions of redshift, axis ratio (b/a) and morphological type. For each interval we calculate the average mass and metallicity (of gas and stars) of barred and unbarred galaxies. The differences in the metallicity of barred and unbarred galaxies are analysed by comparing the distributions of the residuals of both subsamples to a polynomial fit of the points of unbarred galaxies. This analysis is shown in Fig. 2.5.

As can be seen, in each mass range, the differences are small and, in fact, are not statistically significant in any of the intervals (considering a confidence level of 3σ). Although not significant, it is seen that the ionized gas in barred galaxies has, systematically, higher metal content than the gas in unbarred galaxies. Averaging the differences in each mass range, a value of 0.019 is obtained $\pm$ 0.002 dex, which is compatible with the differences found globally, that we found to be statistically significant.

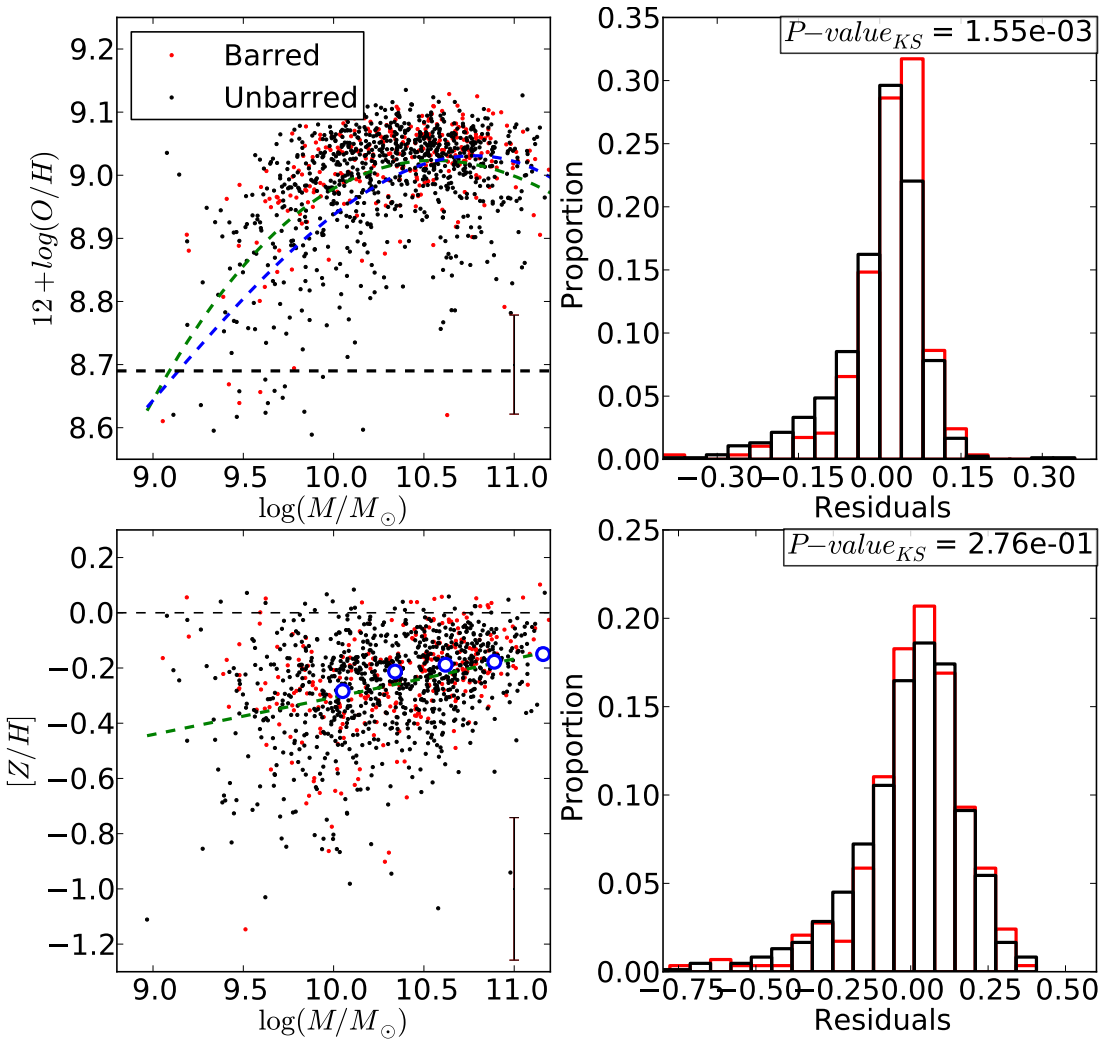

Figure 2.4: Mass-metallicity relation. In the upper left panel we plot the metallicity of the gas *vs.* the stellar mass (from Nair and Abraham, 2010) of the whole sample of galaxies (barred galaxies in red, unbarred galaxies in black). Dashed green and blue lines represent our polynomial fit and that found by Kewley and Ellison (2008), respectively. Error bars represent the typical uncertainty in the metallicity. Lower left panel is the same as upper panel but for the stellar metallicity. In this panel, blue circles represent the mass-metallicity relation found by Vale Asari et al. (2009) shifted −0.25 dex. Right panels show the distributions of the residuals of barred (red) and unbarred (black) galaxies respect to the fitting polynomial. Text boxes in the plots show the P-value obtained in the KS tests.

We repeated the same analysis for the stellar metallicity. In this case (see Figure 2.4) the overall difference between barred and unbarred galaxies (0.015 dex) is not significant, as shown by the KS test. As we did with the mass-metallicity ratio for the gas, we compare the MZ relation of the stars with that found by Vale Asari et al. (2009). Despite the differences between works -different techniques (`STECKMAP` in our case and `STARLIGHT` in theirs), different sample selection (SDSS-DR4 instead of SDSS-DR5, different limiting magnitudes, ranges redshift, cuts in S/N, etc.) and different models of stellar populations- we find an offset of just 0.25 dex between the two relationships, which can be explained simply by the use of different models of stellar populations[4].

Lower panels in Fig. 2.5 show the differences in the stellar metallicity for different mass ranges, as we did for the metallicity of the gas. The differences are compatible with the uncertainties, with a P-value = 0.045. Therefore, we do not find significant differences in the stellar metallicity between barred and unbarred galaxies. It is important to remark that the errors in the determination of stellar metallicities are larger than those of the gaseous metallicities. In fact, given the size of the samples in each bin and considering a significance level of 3σ, the minimum differences which could be detected are about 0.04 dex, on average.

2.5.2. Morphology

Some authors have found that differences in the properties of barred and unbarred galaxies are related to the morphology of the host galaxies. in particular, that these differences are greater in early-type galaxies (Ho et al., 1997; Coelho and Gadotti, 2011). One reason for this could be that early-type galaxies seem to host stronger bars than late type galaxies (Erwin, 2005). To analyse the possible dependence of the differences in the metallicity with the morphology, we split the sample into two subsamples of galaxies, one with morphological types between S0 and Sb ($-2 \geq T \geq 3$) and other with morphological type Sb onwards ($T > 3$).

We perform a similar analysis than in the previous section. This can be seen in Fig. 2.6. For early types galaxies we find a mean difference in the gas metallicity between barred and unbarred galaxies of 0.027 ± 0.007 dex, which is statistically significant with P-value = 0.0018; while for late-type galaxies, this mean difference is only of $0{,}010 \pm 0{,}008$ dex, this is, the differences are

[4]We recalculated the metallicities for a subsample of random galaxies in our sample using Pegase-HR stellar population models. The differences between the results are 0.24 dex.

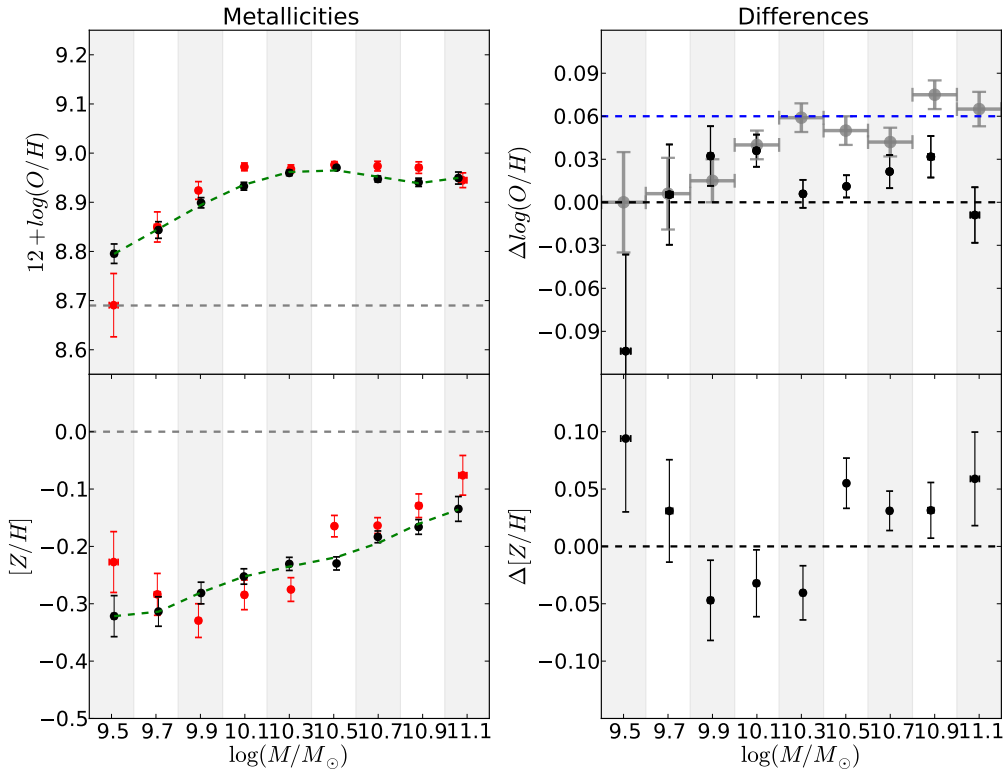

Figure 2.5: *Upper left panel*, Average metallicity against mean stellar mass in each mass interval for barred (red) and unbarred (black) galaxies. Green dashed line represents the polynomial fit to black points. *Lower right panel:*, shows the differences of the red points respect to the polynomial fit. Grey points indicate the differences found by Ellison et al. (2011). Error bars represent the uncertainties in the mean. *Lower panels:* same as upper panels but comparing the stellar metallicity.

larger for early-type galaxies. For the stellar-phase metallicity, the differences are not significant in any case.

We also explore the differences in early and late type galaxies at a given mass, as in the previous section. Fig. 2.7 shows this comparison. Although in none of the cases the differences are significant, in the gaseous metallicity the differences decrease with the mass of the galaxies in early-type galaxies, while the differences are constant with mass for late type galaxies. The smaller differences in late-type galaxies mean that a biased sample toward early-type galaxies may lead to significant differences in the metallicity.

2.5.3. Bar strength

Simulations predict that only strong bars are efficient funneling gas to the central kiloparsec region (Regan and Teuben, 2004), which could mean that differences in metallicity would only be significant in galaxies with strong bars. To test this possibility, we study the differences in the metallicity separating the sample of galaxies into four groups, depending on the label *Bar strength* which appears in the catalogue of Nair and Abraham (2010). In the catalogue, bars are classified as strong, weak or intermediate attending to the luminosity of the bar compared to the total luminosity of the galaxy. The definition of bar strength is based on the torque produced by the bar, which s the ratio between the radial and tangential forces produced by the alignment of stars and dust in the bar (Buta and Block, 2001). This forces are difficult to measure. However, the luminosity of the bar can be used as a proxy for the torque, as both are linked to the mass of the bar.

Figure 2.8 shows the metallicity of gas and stars *vs.* the stellar mass for the barred and unbarred subsamples divided in groups attending to the strength of the bar, as given by Nair and Abraham (2010) compared to the full sample. The analysis is based on the study of the residuals respect a polynomial fit to the points corresponding to the whole sample. For both gas and stellar metallicities, the residuals (*i.e.* the differences between barred galaxies and the whole subsample) tend to increase with the strength of the bar, but the differences are never significantly different from zero.

2.5.4. Star Formation Rate

The ionization parameter plays an important role in the calculation of metallicities of the ionized gas. In particular, it affects the ratio [OIII]$\lambda\lambda$4959, 5007/[OII]λ3727, ([OIII]/[OII] hereafter) which, as we saw in Section 2.2 is significantly different in barred and unbarred galaxies. We use this ratio to calculate meta-

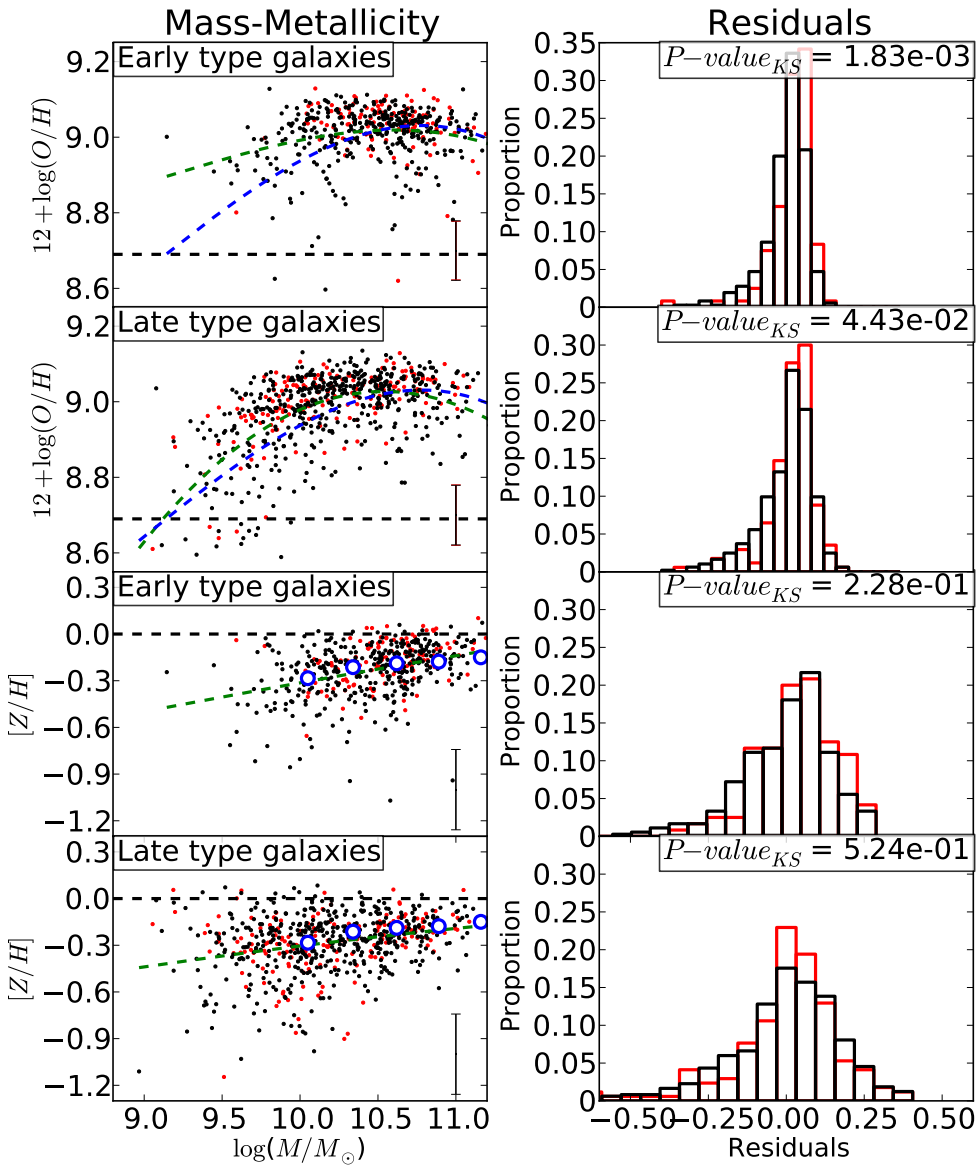

Figure 2.6: The top four panels show the results for the metallicity of the gas of early and late type galaxies. Left panels show the metallicity of barred (red) and unbarred (black) galaxies versus stellar mass. The green dashed lines show a polynomial fit to all points, while the blue dashed lines show the MZ relationship found by Kewley and Ellison (2008). Right panels show the histograms of the residuals of barred and unbarred galaxies respect to the polynomial fit, with the P-value found after a comparison with KS tests. Lower panels corresponde to the analysis of the stellar phase. Blue circles in the left panels correspond to the MZ relation found by Vale Asari et al. (2009) with the already mentioned shift of -0.025 dex.

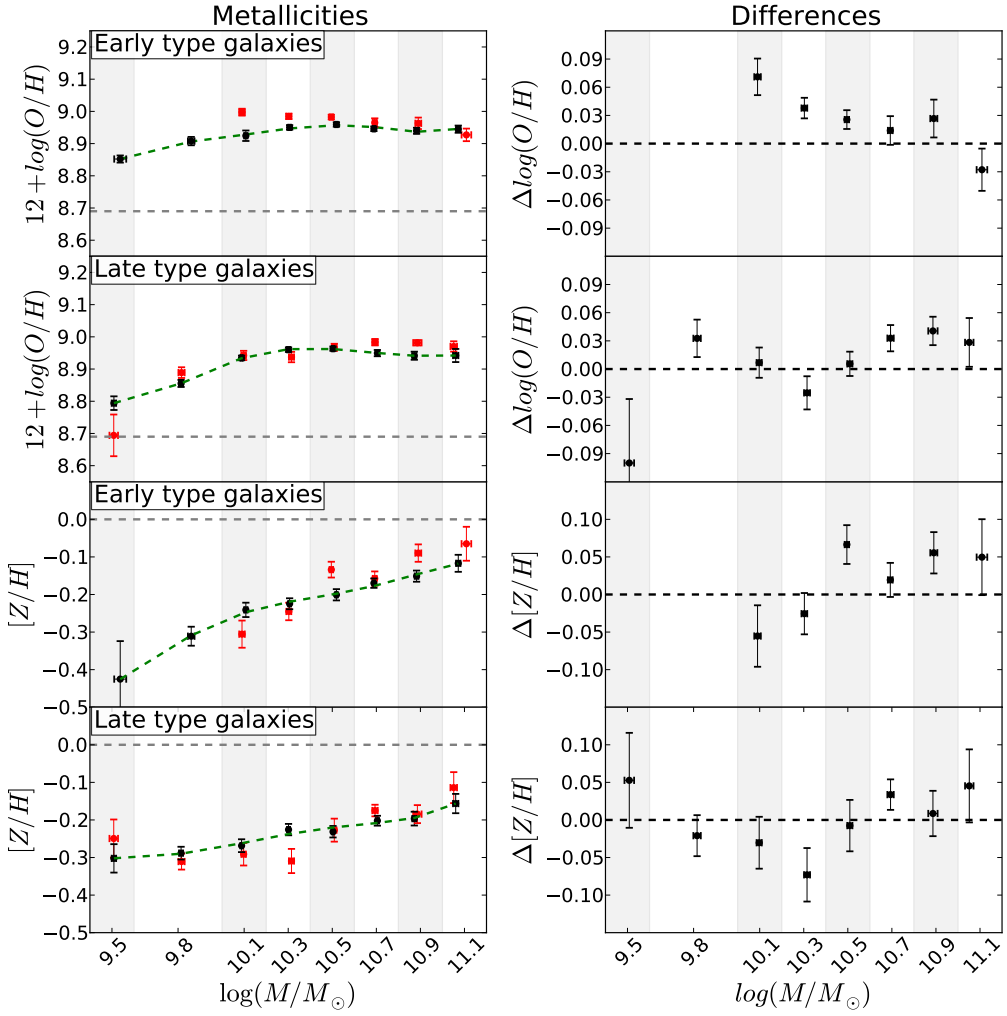

Figure 2.7: Mean metallicities per mass bin for early and late type galaxies. Coding and symbols have the same meaning as in Fig. 2.5 but referred to early (*upper panel*) and late (*lower panel*) type galaxies. The differences are not statistically significant for any of the cases (with a significance level of 3σ.

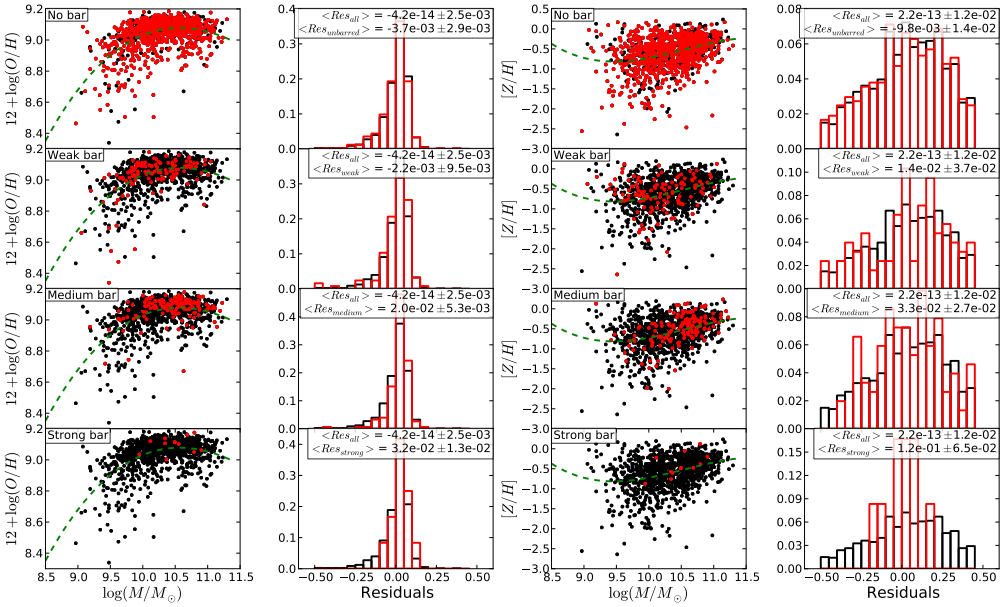

Figure 2.8: On the left, metallicities of gaseous and stellar phases versus the stellar mass for unbarred, weakly barred, intermediate barred and strongly barred galaxies (from top to bottom, in red). Black symbols represent the whole sample. A polynomial fit (green dashed line) to the whole sample is used as reference. On the right, we plot the histograms of the residuals of the corresponding subsample (red) and the whole sample (black) respect to the fit. On the top right corner of each panel, the mean value of the residuals can be found for each subsample and the sample. In none of these cases the differences are statistically significant (P-value > 0.05).

llicities, as showed in Sec. 2.3. First panel in Fig. 2.10 shows a comparison of the ionization parameter in barred and unbarred galaxies. As the P-value shows (for a KS test) the distribution of $\log q$ is different in both subsamples, being slightly higher in the sample of barred galaxies.

The ionization parameter is linked to the star formation rate (Elmegreen, 1994; Knapen et al., 1995; Hunt et al., 1999; Jogee et al., 1999, 2005; Jogee, 2006). Second panel in Fig. 2.10 shows the distributions of the SFR for the two samples of barred and unbarred galaxies. After a KS test, we can conclude that barred and unbarred galaxies have the same SFR distribution.

We also compare the specific star formation rate (sSFR, or SFR per unit stellar mass), which is shown in the bottom panel in Fig. 2.10. In this case, a KS test shows that the sSFR is higher in barred galaxies, which is into agreement with Hawarden et al. (1986) and Ho et al. (1997). At a face view, this result is not expected, as we have shown that the distribution of masses and SFRs is the same in barred and unbarred galaxies.

Figure.2.9 shows a comparison between the SFR in barred and in unbarred galaxies. The SFR is not significantly, but sistematically larger in the barred subsample. This explains the differences in the distribution of the sSFR, despite the SFR and mass distributions are equivalent in both subsamples.

We conclude that barred galaxies, based on its higher $\log q$ and sSFR, form stars more efficiently than unbarred galaxies. Bars are an efficient mechanism to funnel gas to the central regions, so a barred galaxy has more gas available to form stars than an unbarred galaxy with the same mass. Because of this, barred galaxies will form more high-mass stars than its unbarred counterpart, leading to higher ionization parameters in the barred sample.

2.6. Comparison of stellar and gaseous parameters.

2.6.1. Comparison of ages and stellar mass

Figure 2.11 shows the age of the stellar populations in the centre of the galaxies as a function of the stellar mass. Despite this is a comparison between local (age) and global (mass) parameters, there is a strong correlation between them. This is independent of galaxies being barred or unbarred, as proven by the small differences between the subsamples (shown in right panel in Figure 2.11.

We do not find the same results as Coelho and Gadotti (2011), that found that the distribution of ages in barred galaxies is bimodal, peaking at

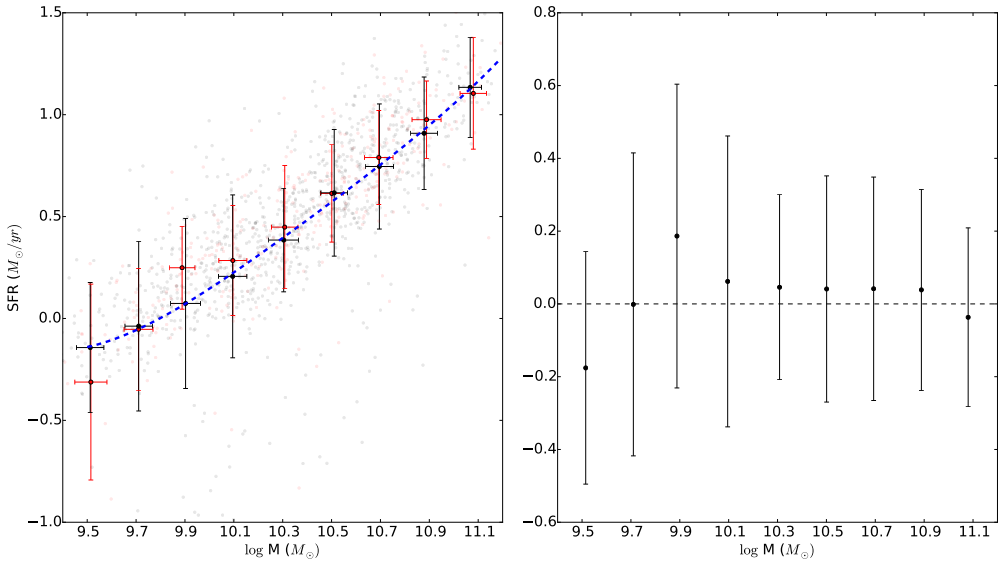

Figure 2.9: Comparison of the star formation rates in barred and unbarred galaxies. Left panel shows the star formation rate of barred (red) and unbarred (black) galaxies at a given mass. The not binned results are represented as light red and black points. The blue dashed line is a third order polynomial fitting the binned points for unbarred galaxies. The right panel shows the residuals of the barred galaxies (binned in mass) respect to that polynomial. The error bars represent the dispersion of the data in each bin

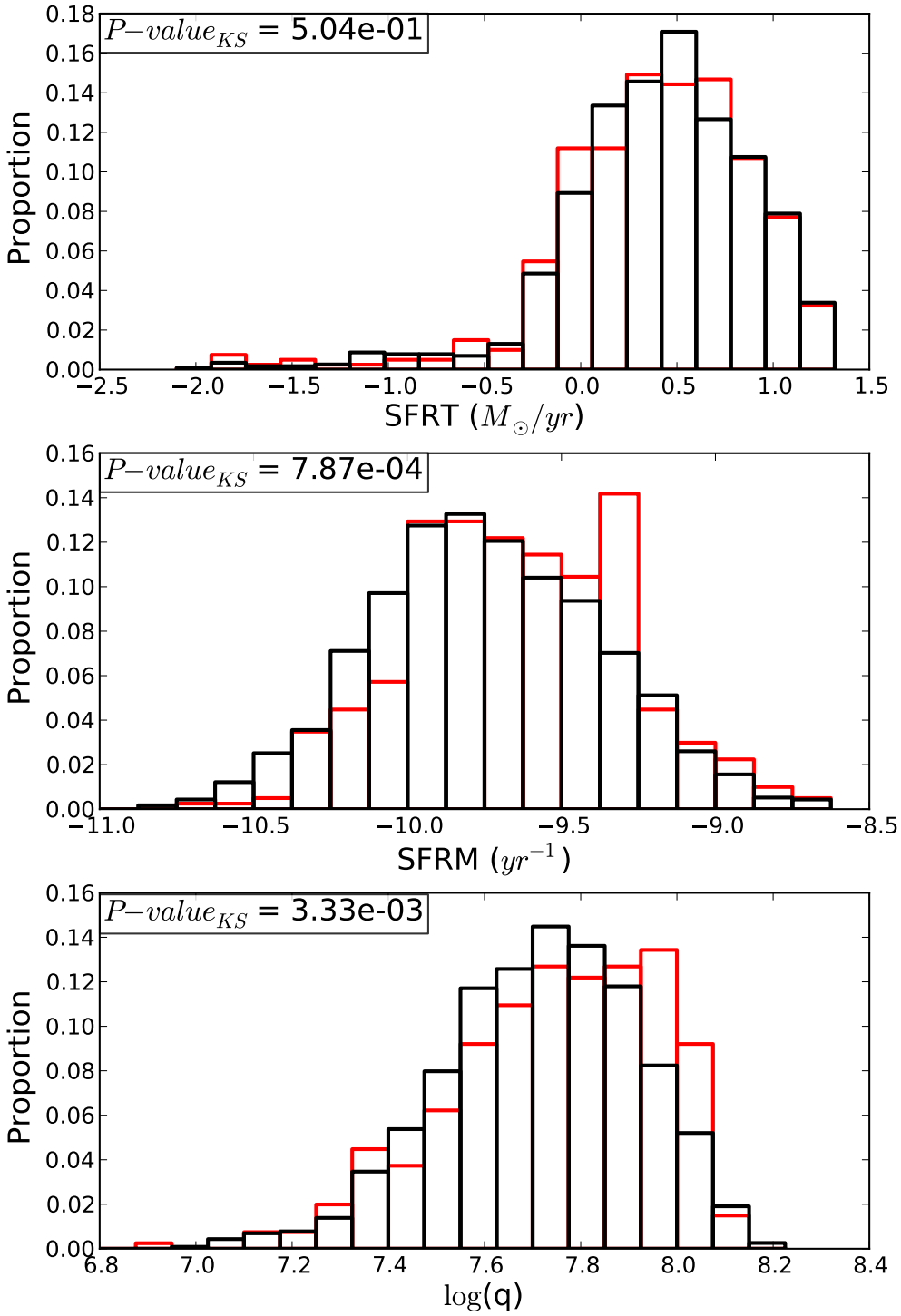

Figure 2.10: From top to bottom, distributions of star formation rate, specific star formation rate and ionization parameter for barred galaxies (in red) and unbarred galaxies (in black). In the text boxes there are the P-values resulting of testing the equivalence of the barred and unbarred distributions with KS tests.

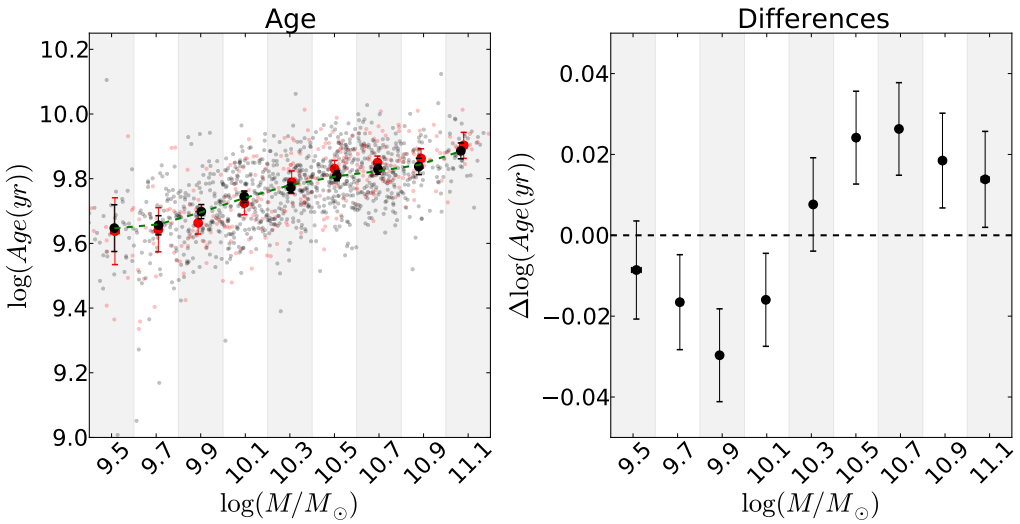

Figure 2.11: *Left panel:* Small dots represent individual galaxies (red for barred, black for unbarred), and big points represent the mean ages and metallicities of the galaxies in each mass interval. The green line represents a polynomial fit to unbarred galaxies. Error bars represent the uncertainties in the mean. *Right panel:* Residuals of barred galaxies respect to the polynomial fitting the unbarred galaxies. None of the differences are statistically significant.

4.7 y 10.4 Gyr, whilst in unbarred galaxies the distribution does not show the younger peak. However, they only find this bimodality for very massive galaxies (with $M_{bulge} \leq 10{,}1$). Due to our sample selection, we do not have enough massive galaxies for a deeper comparison.

2.6.2. Comparison of metallicities with age

A comparison of the metallicities of the gas and the stars in barred and unbarred galaxies may help to differentiate if the bar plays a determinant role in the evolution of galaxies. Fig. 2.12 show this comparison for both metallicities. Whilst a little correlation exists between stellar age and metallicity (with a large scatter), this does not happen for the gas, which supports the conclusion that the chemical properties of gas is not coupled to the stellar population parameters in the central regions of galaxies

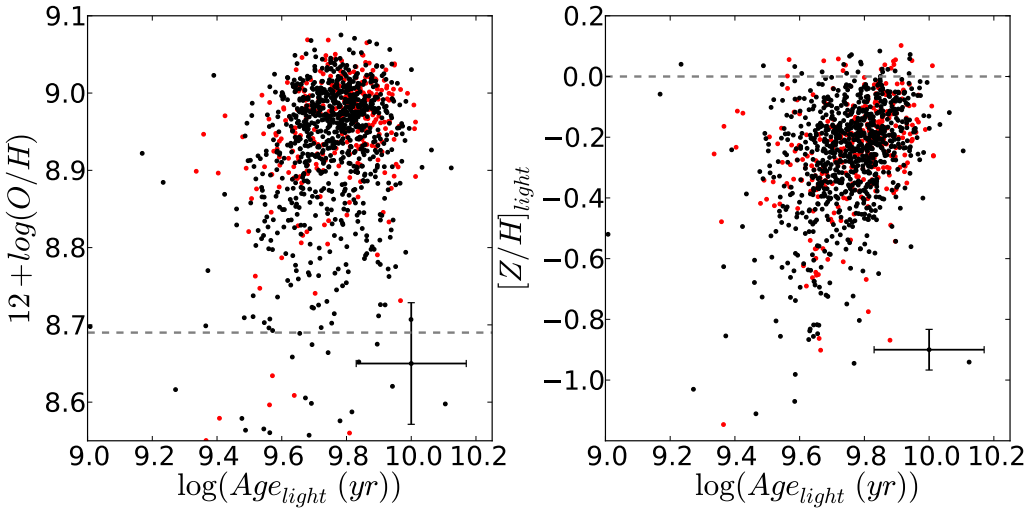

Figure 2.12: Gas-phase (*left panel*) and stellar (*right panel*) agains the stellar age. Red points represent barred galaxies, and black points represent unbarred galaxies. Error bars show the typical uncertainties in the parameters.

2.6.3. Comparison of gas and stellar metallicities

Figure 2.13 shows the gas-phase metallicity *vs.* the stellar metallicity for barred and unbarred galaxies in our sample. It can be seen (and it is confirmed by the Spearman's correlation test) that no correlation exists between the metallicities of gas and stars neither for barred nor for unbarred galaxies.

We checked if the metallicities calculated in a classical $H\beta$-Mgb diagram (*i.e.* Trager et al., 2000) were better correlated with the gas-phase metallicity, but this was not the case.

Lick/IDS Indices (Worthey et al., 1994) is a classical method for calculating stellar metallicities. It consists in comparing the flux in a defined region of the spectrum with the continuum in that region. This continuum is estimated with the flux in two regions adjacent to that in which the absorption wants to be measured. Depending on the chemical species contributing to the absorption, a particular index traces (better or worse) the properties (in particular age and/or metallicity) of the stellar populations contributing to the spectrum. One of these indices is Mgb5177, focused on the magnesium triplet near that wavelength. This index is strongly dependent of the metallicity, and depends very little on the age, so it is one of the indices which best traces this parameter. The process of calculating metallicities through indices is affected by large uncertainties and an interpolation from points on a grid is necessary. To ensure that the process of calculating metallici-

ties is not affecting the results, we also compared the gas-phase metallicity with Mgb5177, but there is also no correlation. However, given the uncertainties in both metallicities, we are not able to detect correlation between this parameters, even when it exists.

2.7. Comparison with previous work

2.7.1. Gas-phase metallicity

As we mentioned in the introduction, there is a lot of controversy in the literature regarding the possible differences (or lack of) between the metallicity of barred and unbarred galaxies. In this section we will try to understand the origin of these discrepancies.

rom the 90's there are works in the literature comparing the metallicity of the gas in barred and unbarred galaxies (Dutil and Roy, 1999; Considère et al., 2000; Henry and Worthey, 1999), finding that metallicities are similar or smaller in barred galaxies. However, and owing to technical limitations, those results were obtained from small samples, biased to late-type galaxies.

The last work published before us, that by Ellison et al. (2011) (E11, hereafter), used a large sample covering wide ranges of mass, inclination and redshift. They found that central metallicities in barred galaxies are higher (0.06 dex) than in unbarred galaxies of the same mass. This study, as our, is using a large sample of galaxies from SDSS selected with similar criteria as our sample. They also used the catalogue of Nair and Abraham (2010) to separate barred and unbarred galaxies and, despite all that, is obtained a much higher difference in metallicity and SFR than the present work. It is worth exploring the origin of these differences which could also help to understand the discrepancies between earlier studies.

The differences between E11 and our can be summarized in this points:

- Our subsamples of barred and unbarred galaxies have the same distributions of age, inclination (axial ratio), and redshift, as in E11. The only difference is that we took care of making our subsamples equivalent in terms of mass, redshift, axial ratio and morphology.

- We use the emission line fluxes from OSSY database, while E11 those from MPA/JHU (whose differences were explained in Section 2.2).

- Finally, we used a metallicity calibration based on R_{23}, while E11 chose a calibration based on [NII]/[OII].

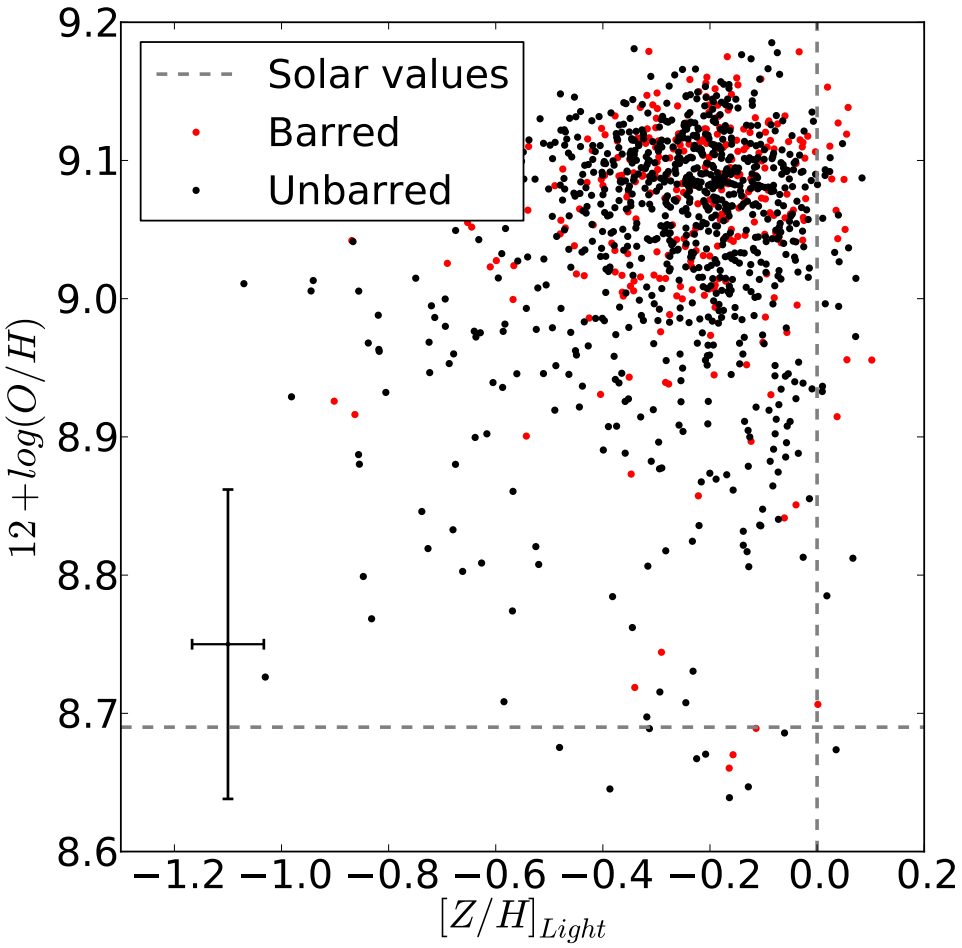

Figure 2.13: Comparison of the metallicities of gas and stars for barred (red) and unbarred(black) galaxies. Dashed lines represent solar values and error bars indicate the typical uncertainty of the parameters.

We will explore how these different choice might affect the final result in the following sections.

2.7.1.1. Selection effects

One of the differences in the sample selection is that in our sample, contrary to the sample in E11, the subsamples of barred and unbarred galaxies have the same morphological distribution. In Section 2.5.2 we showed that the differences in the central metallicity are higher for early-type galaxies. Therefore, a sample biased towards these objects could enhance the differences. To check (and quantify) if this criterion affects the results, we compare the differences between barred and unbarred galaxies from two different samples, of which one of them has similar morphology distributions for barred and unabrred galaxies, while the other does not. First row in Figure 2.14 shows this comparison. Orange points represent the sample in which barred and unbarred galaxies have similar morphologies, and purple points represent the sample with different morphologies. On the right panel we plot the differences between orange and purple points. On average, the differences between considering or not equivalent morphological distributions increase by 5×10^{-3} dex, much smaller than the uncertainties.

2.7.1.2. Emission line fluxes

There are two effects related to this point, and we will analyse them independently. One of them is the difference in the S/N measured for each spectrum. The other one is related with different measurements of the flux, depending on the methodology used in each database (OSSY in our case, MPA/JHU in E11).

The S/N of the fluxes have a relevance in the sample selection because of the cut we made to avoid very noisy measurements. E11 selected only those galaxies with a S/N in [OII]λ3727, Hβ, [OIII]λ4959 and [NII]λ6584 above 5. Trying to reproduce their criteria we selected those galaxies with a S/N in the same lines above 3. The reason for that is that the S/N of the OSSY database is lower than in the MPA/JHU (with a correlation slope of 5/3). Fig. 2.14 shows the metallicity differences between barred and unbarred galaxies selected with a S/N$\geq$3 and S/N$\geq$5. It can be seen that purple points (S/N$\geq$5) are not significantly, but systematically, over orange points (S/N$\geq$5). On the right panel we can see that the differences between purple and orange points are systematically positive.

Apart from the different S/N, we already saw in Section 2.2 that significant differences exist in the ratio [OIII]/[OII]. This ratio is used to derive the

ionization parameter, which takes part in the calculation of the metallicity in most calibrations.

We calculated the differences in the metallicity using the fluxes of the emission lines from both data bases (OSSY and MPA/JHU), which is shown in the third row of Fig. 2.14. The differences in the results using OSSY or MPA/JHU (black points on the right panel) are not significantly different from zero, and no trends can be seen.

2.7.1.3. Metallicity calibrations

R_{23} is a widely used calibration, which can be used with the emission lines in the wavelength range in our data. It can trace the metallicity of the ionized gas in the whole range of metallicities. However it is bivaluated. Therefore, we need another calibration to distinguish between high or low metallicity regimes. We used [NII]/[OII], which is mostly independent of the ionization parameter, but for low metallicities, the primary nitrogen is dominant, so the metallicity obtained in this regime is not precise. Because of this E11 used [NII]/[OII] if $12 + \log(O/H) \leq 8.5$ and R_{23} if the opposite happens.

Figure 2.14 shows (in its fourth row) the differences owing to the use of R_{23} (orange) or [NII]/[OII] (purple). Even when the differences between calibrations are not significant, they are the largest of all the parameters under analysis. Our explanation is that [NII]/[OII] is less sensitive to the ionization parameter than R_{23}, and we saw (Fig. 2.10) that the ionization parameter is larger in barred than in unbarred galaxies. These differences imply that, with the same value of R_{23} the metallicity can vary up to 0.04 dex, depending on the metallicity range.

2.7.1.4. Combination of parameters

None of the parameters explains on its own the discrepancies between E11 and our work. The effect of each parameter is not significant. However, in Fig. 2.14 the purple points are sistematically over the orange points. Therefore, we analyse the combined effect of all criteria.

The bottom panels in Fig. 2.14 show this comparison. Left panel shows in orange the differences in the metallicity between barred and unbarred galaxies selected following our criteria, in purple the differences found by E11 and, in green, the orange points with the differences in the four top right panels added. Right panel shows the differences between purple and green points. As can be seen, the discrepancies now are negligible, and we can reproduce the results of E11.

This comparison should alert us about all the small choice we make when

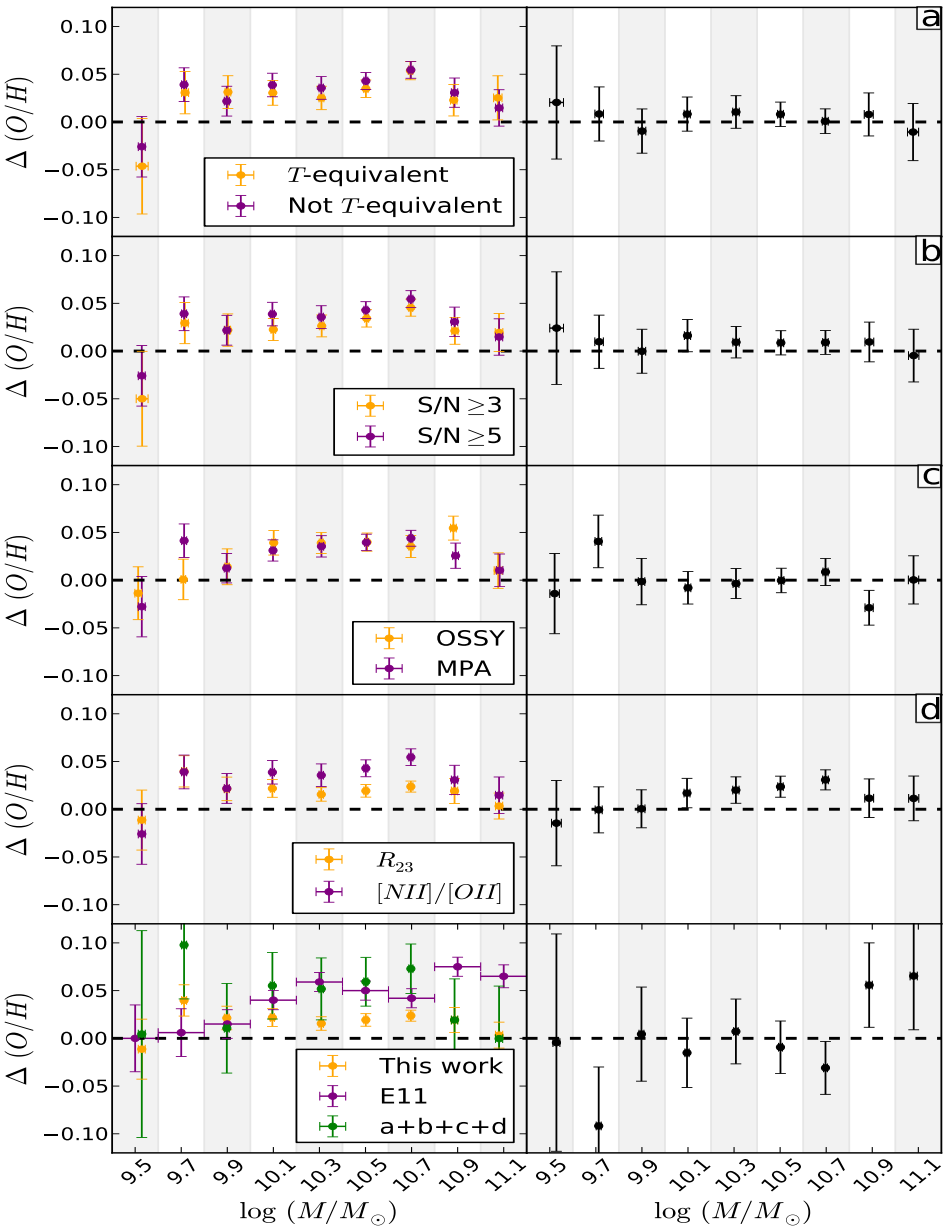

Figure 2.14: Effects of the selection criteria on the results. Left panels show, in orange, the differences in the metallicity between barred and unbarred galaxies found in this work and, in purple, the same differences when one of the criteria is modified. Right panels show the discrepancies between orange and purple points on left panels, except in the bottom panel, where the points represent the differences between the purple and the green points. From top to bottom, the four first panels refer to modifying the selection criterion of morphology distribution, S/N, database and metallicity calibration, respectively. Lower panel shows in orange the differences between barred and unabrred gaalxies found in our work, in purple the differences found by E11 and in green the orange points plus the differences found in the previous four right panels. Bottom right panel shows the differences between purple and green points. Error bars are compatible with the differences being negligible.

we select our samples. Even with such an enormous samples as those in SDSS we introduce selection biases by every little cut we apply to the sample. In this case, the large differences found by E11 were not found in this study and the reason is a combination of a different metallicity indicator, flux database and different ways to make the samples equivalent or not in morphology.

2.7.2. Stellar phase metallicity.

Regarding the stellar phase, there is much less previous work than for the gaseous phase. Moorthy and Holtzman (2006) and Pérez and Sánchez-Blázquez (2011) found hints of stellar populations being more metal rich in barred than in unbarred galaxies. Taking into account our sample size, the uncertainties in the results and the confidence level, we could only be able to consider significant differences those over $\Delta[Z/H] \geq 0{,}022$, which is larger than those found by Moorthy and Holtzman (2006) and Pérez and Sánchez-Blázquez (2011)

Our work expands the morphological range toward late-type galaxies. Our results are into agreement with those of Coelho and Gadotti (2011), where they did not find significant differences in the stellar metallicity of barred and unbarred galaxies considering all morphological types. As mentioned before, they also found a low age component ($\sim$ 4,7 Ga) in the barred galaxy subsample, which did not appear in the unbarred sample. We do not find a bimodal distribution, but the galaxies in our sample as not as massive as those in the sample of Coelho and Gadotti (2011).

2.8. Mass as a reference variable

In this study we compare the properties of barred and unbarred galaxies at a given mass. However, measuring the mass is not a simple task, and it is always an indirect measurement which depends strongly on models, and with large uncertainties (Magris C. et al., 2011; Roediger and Courteau, 2015). As a suggestion of the referee for Cacho et al. (2014) we repeated the analysis using the luminosity instead of the mass as the independent variable, obtaining exactly the same results.

2.9. Summary and conclusions

In this chapter we obtain the metallicities of both ionized gas and stellar populations (along with their ages) for a sample of almost 1600 galaxies (414

barred and 1180 unbarred galaxies). We also compare stellar and gaseous properties and conciliate the discrepancies between our results and those claimed in previous work. In this section we compile and discuss the results obtained in previous sections along with some important points which are worth to discuss.

2.9.1. Gas-phase metallicity in the centres of galaxies

We calculate the metallicities of the gas in galaxies using emission line fluxes obtained from OSSY, measured in the spectrum from SDSS. For the calculation of the metallicities we use a calibration based in the parameter R_{23} described in Kewley and Dopita (2002). We compare these metallicities between two subsamples of barred and unbarred galaxies from different points of view.

We find that, in most cases, these differences are not significant (using a level of 3σ, associated to a P-value=0.0027). However, barred galaxies are systematically more metal-rich than their unbarred counterparts, which is clearer in early-type galaxies (S0-Sb). In this morphological range, differences tend to decrease with mass. The trend is the opposite in late-type galaxies. The lack of differences is into disagreement with what simulations predict; *e.g.* the recent work by (Martel et al., 2013), which analyses the central metallicities in barred galaxies, concludes bar enhances the metallicity in up to $\Delta[O/H] \simeq 0.5$ dex.

We compare our results with previous works, and we find discrepancies among results. Some authors claim that barred galaxies are more metal-rich than unbarred galaxies, whilst others claim the opposite, with some works concluding that there are no differences in the metallicity of barred and unbarred galaxies. We try to find the source of the discrepancies comparing our results with a work in which the analysis is similar to ours, that performed by E11. To do so, we isolated the effect that each sample selection criterion has on the metallicities. Most of the discrepancies arise from the metallicity calibration (up to 0.02 dex between [NII]/[OII] and R_{23} based calibrations). Whilst most of the criterion have non-significant effects, they systematically modify the differences in the same direction and, therefore, when all of them are taken into account, the differences can be up to 0.04 dex, which means to be the value of the discrepancies between E11 and our work.

We compare the star formation rate between both subsamples of galaxies and, whilst the SFR is the same in barred and unbarred galaxies, the specific star formation rate (SFR per unit mass) is larger in barred galaxies. This means that barred galaxies are more efficient forming stars than unbarred

galaxies. This is because bars funnel gas from the outer regions to the central parts of the galaxy, which means more gas available to form stars and more massive stars formed. this is into agreement with the higher ionization parameter found in barred galaxies. These massive stars could be the responsible of the higher metallicity in barred galaxies.

2.9.2. Stellar-phase metallicity in the centres of galaxies.

In the literature there are not many studies comparing the stellar metallicity of barred and unbarred galaxies. This comparison is not the final aim of the analysis and, therefore, the samples are not selected on purpose for this comparison. Both studies are biased towards early-type galaxies and contain very low number of objects. In this work we compare the stellar population properties in the centres of barred and unbarred galaxies with a larger sample of galaxies than in previous work.

We calculate the stellar population properties with `STECKMAP`, a full spectral fitting software which allows to obtain the star formation history and the age-metallicity relation from an integrated spectrum. Full spectral fitting is a quite new technique, and there is still some scepticism about it. For this reason we compare the results obtained with this technique with the results obtained using the more traditional Lick/IDS indices (see Appendix B for more information, where we conclude that both techniques are compatible, but degeneracies are less problematic using spectral synthesis).

We analyse the stellar metallicity in parallel with the gaseous metallicity, and we obtain that stellar metallicities in barred and unbarred galaxies are not significantly different in any of the experiments. This result is into agreement with Coelho and Gadotti (2011). Even more, Coelho and Gadotti (2011) only covered early-type galaxies, while our study is extent to galaxies in the whole morphological range using, in addition, a larger sample of galaxies. We have to remark that the differences found here are smaller than those we can consider significant at a confidence level of 3σ, which is 0.022 dex.

2.9.3. Comparison of gaseous and stellar parameters

One of the goals in this work is the comparison of the parametersa calculated for the gas, and the parameters of the stellar populations, which has not been done before. We make the first comparison of the results obtained through emission lines and the stellar populations in the central regions of

galaxies.

We expected to find correlation between stellar and gaseous metallicities but, at least for the redshift interval in which these galaxies lie ($0.02 \geq z \geq 0.1$) this is not true. This may owe to a different evolution for gas and stars (at least in the central regions of galaxies) or a saturation in the metallicities, this is gas and stars have had time to evolve to reach the higher possible metallicity. The comparison of the gaseous and stellar metallicities with the age of the stellar populations show that no correlation exists between gas-phase metallicity and the age of the stellar populations but it exists (weakly) in the case of the stellar metallicity. This supports the results that the evolution of the gas in the centre of a galaxy is decoupled of the evolution of the stars in that region. The fact that we find this correlation confirms that spectral synthesis is able of breaking degeneracies between age and metallicity; if the degeneracy had not been broken, we would expect an anti-correlation.

Finally we analyse the age of the stellar populations with the mass of the galaxy, comparing the barred and unbarred galaxies subsamples. A clear correlatione xists between the age of the stellar populations and the galaxy mass (as expected) which is not different in barred and unbarred galaxies.

Chapter 3

Stellar populations in galactic bulges

3.1. Introduction

Although less common than in elliptical galaxies, studies of stellar population in bulges are common in the literature (Proctor and Sansom, 2002; Prugniel and Soubiran, 2001; Trager et al., 2000; Ganda et al., 2007). Most of these studies have been done using long slit spectroscopy, with samples biased towards early type systems, due to the difficulty in removing emission lines. The interpretation of these observations are difficult due to the complexity of structures in the centre of spiral galaxies, where rings, bars, discs, classical bulges, etc., can cohabit. The situation is improving with the arrival of integral field spectrographs. Indeed, Peletier et al. (2012, checa esta referencia) showed that the presence of young populations is usually associated with central discs or rings and that different types of bulges can coexist in the same galaxy.

They show in this article the importance of study bulges using these IFS in order to quantify the stellar population properties of the different components and to associate them to the different morphologies. Only in this way we will be able to elucidate the physical processes responsible for their formation. In this chapter we represent a pilot study devoted to understand, in a detailed way, the stellar population properties of bulges.

3.2. Sample and observations

3.2.1. The sample

Because this is a pilot study, we choose the sample to be diverse in its morphological properties. We choose three galaxies in which we expect to find different combinations of stellar populations attending to their morphology, especially in their central regions, as the integral field unit we use has a field of view of only (38×25 arcsec^2). These galaxies were selected from the Carnegie-Irvine Galaxy Survey (Ho et al., 2011) and the catalogue of inner discs and rings of Erwin and Sparke (2002). These galaxies have a bulge-disc decomposition performed by Li et al. (2011). The complexity of these galaxies is evident from their images, but the use of unsharp masked images (following Erwin, 2004; Lisker et al., 2006, see Fig. 3.1) reveals non-radial small-scale structures hidden by the dominant structures in the galaxies. In the following we present a short description of the three galaxies:

NGC5701 is a S0 galaxy with a round bulge and a prominent bar. It is considered one of the best examples of a bar embedded in a strong lens (Buta et al., 2002). In broad band filters it does not show absorption by dust, but it shows some Hα emission in a nuclear spiral (Erwin and Sparke, 2002). This galaxy has a very low surface brightness disc (Gadotti and de Souza, 2003; Gadotti, 2008).

NGC6753 is an SAb galaxy with higher structural complexity than NGC5701 and a very prominent star formation ring (Crocker et al., 1996). Outside this ring a flocculent spiral structure can be found.

NGC7552 (SBab) is dominated by a morphologically complex, dusty bar and a central starburst, showing a small bulge. This galaxy shows intense star formation in the field of view of the instrument, taking place not only in a nuclear ring, but also along the bar and the disc (Hameed and Devereux, 1999). This galaxy belongs to the Grus triplet, so it may have been affected by interactions; in fact, asymmetries in their arms can be seen.

3.2.2. Observations

We observed these galaxies in July and September 2013 at the 2.3m telescope in Siding Spring Observatory (SSO, Australia). We used the Wide Field Spectrograph (WiFeS) which provides a field of view of 38×25 arcsec^2 with a spaxel size of 1×1 arcsec^2. This instrument allows to observe in two different regions of the spectrum with the same or different spectral resolutions. We used two the highest spectral resolution grating for the blue region,

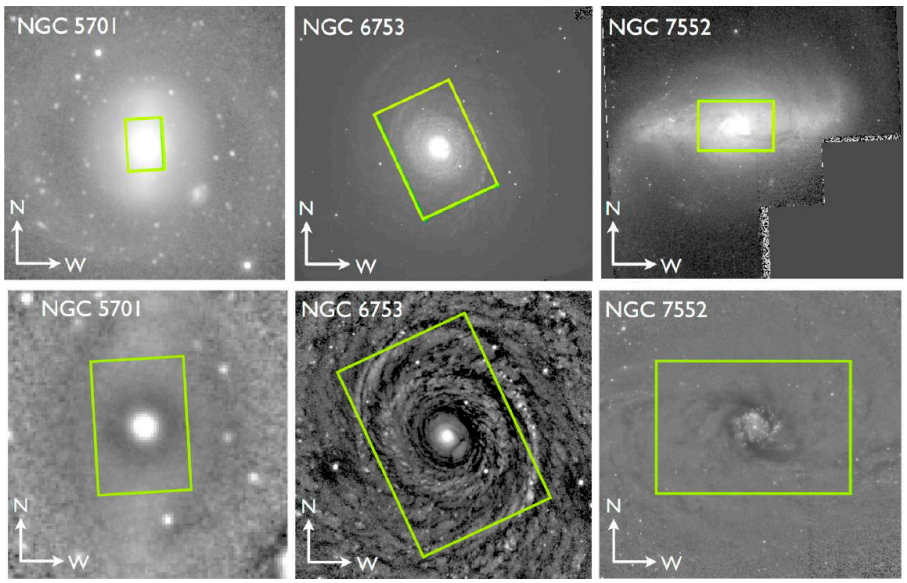

Figure 3.1: HST (top) and unsharp mask (bottom) images of the three galaxies in the sample. The unsharp mask images are obtained by subtracting a radial luminosity model which allows to subtract axysimmetric structures, revealing *hidden* structures.

called B7000. B7000 covers the spectral range from 4180 to 5580 Å with a FWHM=43 km/s. The good spectral resolution of this instrument allows to measure low velocity dispersion (hereafter, σ) while covering a wide wavelength range, which is also important for the spectral fitting. More details about the instrument can be found in Dopita et al. (2007, 2010).

The data reduction was performed by means of the pipeline provided by the observatory, `pyWiFeS` (Childress et al., 2014). It consists in a regular reduction process for IFU data including bias substraction, flat field correction (using both, lamp and sky flats), distortions correction, wavelength calibration, sky lines removal, telluric lines removal (only for the red arm, using observations of white dwarves), flux calibration and data cube generation. The wavelength calibration for the pipeline was not finished when we reduced the data, and the lamp we used (NeAr) was still not included in the pipeline in combination with the grating we used (B7000). We had to, therefore, create our reference files using the wavelengths in NIST webpage [1]. The final accuracy in the wavelength calibration is $\Delta\lambda$ =0.1 Å.

The final data consists in two cubes, one spanning from 4100Å to 5500Å and a spectral sampling of 0.347Å/pixel and a FWHM=1.0 Å and the other covering the range from 6800Å to 8930 Å with a sampling of 0.567 Å/pixel and a FWHM=1.6 Å.

3.3. Analysis

In this section we extract the properties of the galaxies using Lick/IDS indices and full spectral fitting, by means of `pPXF` (Cappellari and Emsellem, 2004), to calculate the kinematics and `STECKMAP` (Ocvirk et al., 2006a,b) to estimate the age and the metallicity of the stellar populations.

We start by binning the data cubes in order to reach a minimum S/N. To do so, we use a Voronoi binning scheme. (Cappellari and Copin, 2003). The chosen S/N for NGC5701 and NGC7552 is 20 per resolution element, while for NGC6753 (due to the large amount of time observing this galaxy) is 40. In the binning, spaxels with $S/N \leq 3$ were rejected.

3.3.1. Calculation of kinematics

The kinematics is calculated using full spectral fitting, through the code `pPXF` (Cappellari and Emsellem, 2004). As every full spectral fitting software, `pPXF` requires a stellar population library. In this case we use `PEGASE-HR`

[1] http://www.nist.gov/pml/data/index.cfm

with R=10000 Le Borgne et al. (2004) because it is the only stellar population library with larger wavelength coverage and resolution than our data. `pPXF` also includes a set of gaussian synthetic emission lines to perform a simultaneous fit of the emission lines by the ionized gas and the stellar continuum, deriving the kinematics of both of them. `pPXF` considers the velocity distribution as a Gauss-Hermite parametrization, which consists in four parameters, v, the mean velocity of the distribution; σ, the velocity dispersion; h_3, which is related to the skewness of a distribution; and h_4, is related to the kurtosis. We calculate all these parameters for the stellar component while a Gaussian distribution is assumed for the gas. `pPXF` is also a tool to remove the gas emission from the spectrum.

3.3.2. Stellar kinematics

Figure 3.2 shows the derived parameters of the kinematics for NGC5701. One of the most obvious things is a clear misalignment between the bar and the kinematic axis. The radial velocity reaches ∼40 km/s, and the σ profile has a peak near the centre (the maximum is not reached exactly in the center as this galaxy present a σ-drop) at 110 km/s and drops to the outer parts to less than 100 km/s. The lack of anticorrelation between h_3 with the velocity is consistent with the high values of h_4 in the centre and is compatible with a region dominated by a bulge (as shown by the ratio between bulge and total luminosity of the galaxy in Weinzirl et al., 2009). A nuclear spiral has also been detected in this galaxy Erwin and Sparke (2002), which could explain the deviation of the velocity distribution from a Gaussian curve, as indicated by the high values of h_3 and h_4.

Figure 3.3 represents the kinematics in NGC6753. What draw the attention is the large rotational velocity (∼150 km/s) and σ (215 km/s), mainly if we consider the inclination of this galaxy (∼ 30°) and that our FoV covers only the very central region. This indicates a very hot component (bulge) which dilutes rapidly in a colder component (disc). However, the inner ring is not visible in the velocity or σ maps. In the h_3 map an anticorrelation with the radial velocity is evident, indicating the clear presence of a rotating disc. In the h_4 map, the star formation ring is visible as a region with the highest values of h_4, suggesting different kinematics of the stellar populations in the ring.

The corresponding maps and radial profiles for the kinematics in NGC7552 is shown in Fig. 3.4. NGC7552 shows a similar rotation than NGC5701. We clearly detect a ring-shaped region with high σ surrounding the inner spiral seen in the unmasked sharp images.

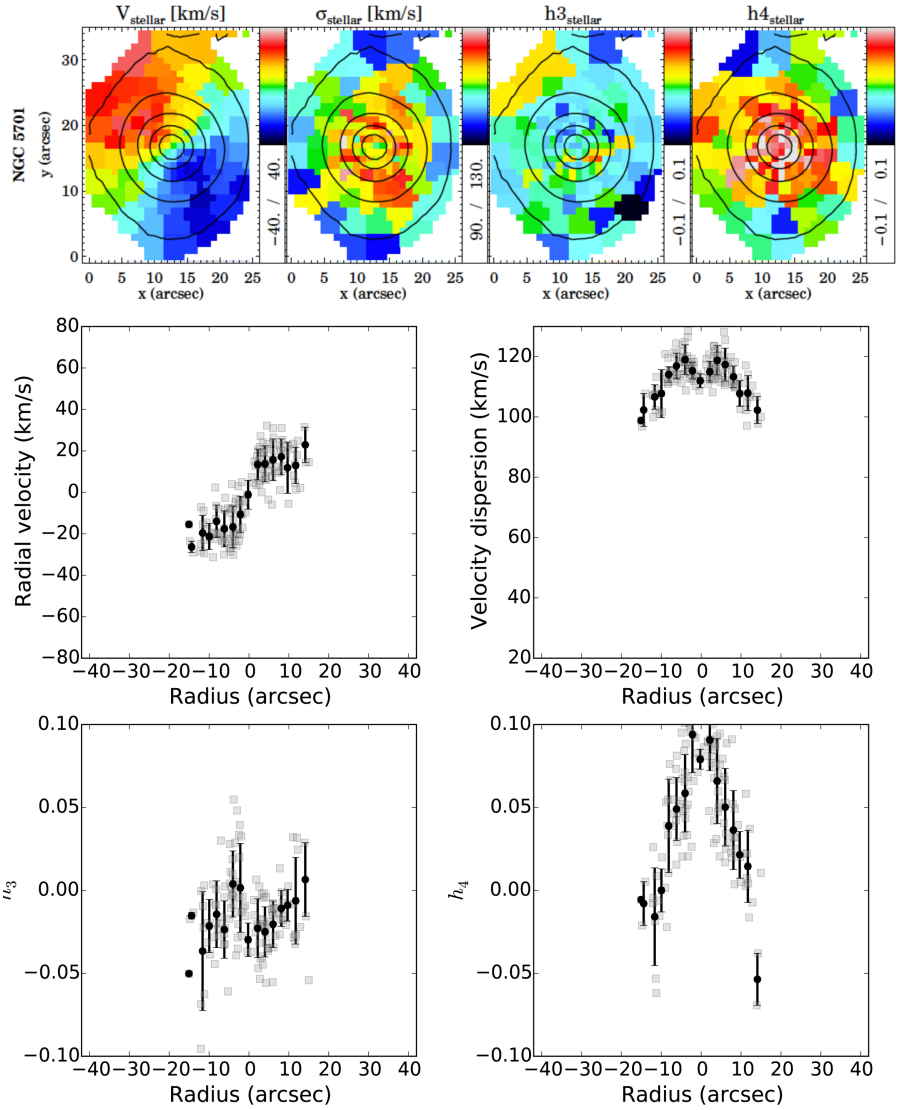

Figure 3.2: The top panels show, from left to right mean velocity, σ, h_3 and h_4 for the stellar component in NGC5701. The scale of each parameter is shown with a colour bar on the right of each panel. Black contours indicate isophotes (spaced by 0.5 magnitudes), measured on the collapsed data cubes The four bottom panels show the radial profiles (radial velocity, top left; σ, top right; h_3, bottom left; and h_4, bottom right) obtained by averaging the derived kinematical parameters in concentric semi-annuli. Positive radii indicate positions where the radial velocity is positive. Error bars represent the dispersion of the values in each semi-annulus.

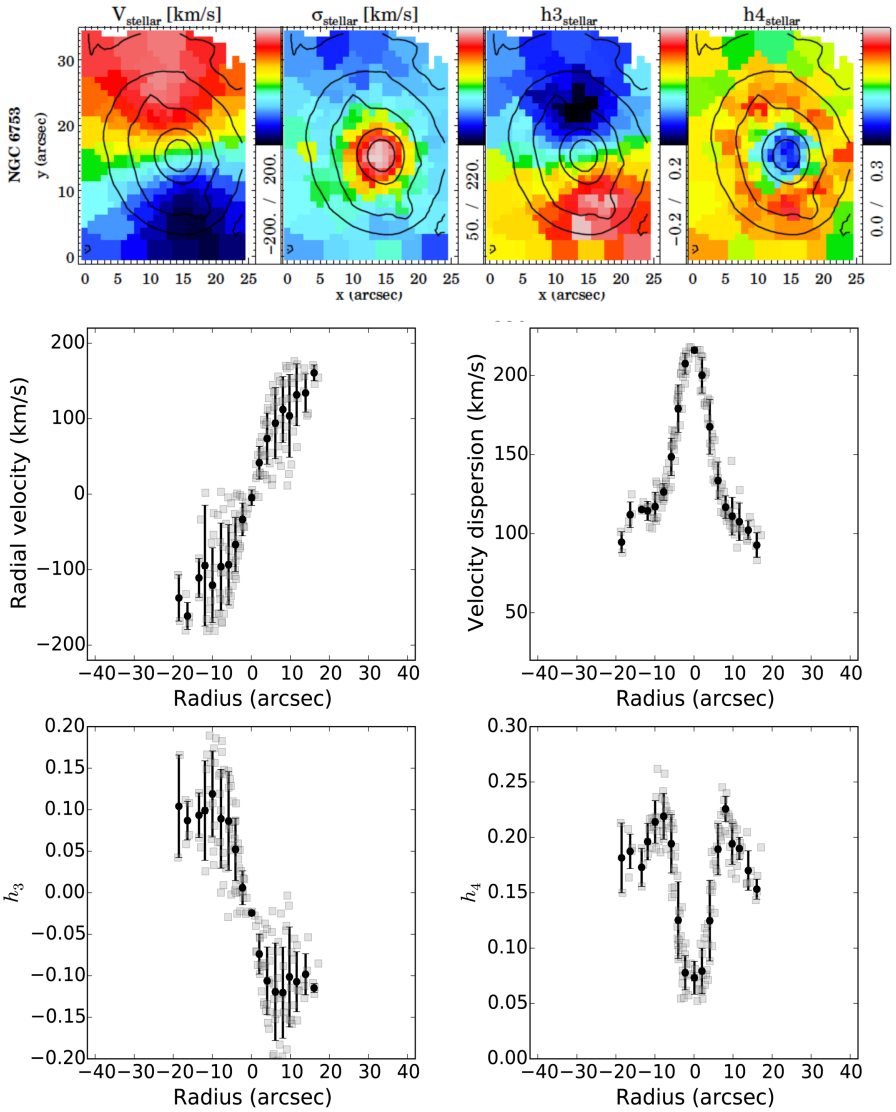

Figure 3.3: This figure show the maps and radial profiles for the velocity, σ, h_3 and h_4 for NGC6753. Symbols and colours represent the same as in Fig. 3.2

These three galaxies show, as expected by their different morphologies, very different kinematics. This is particularly true in the h_3 and h_4 maps, with very different behaviour in the three galaxies. In particular, in NGC6753 a clear anticorrelation of h_3 and the velocity field exists and h_4 shows a different kinematics in the inner ring. The different kinematics reflect the differences in the subcomponents present in the three galaxies.

3.3.3. Gas kinematics

Figs. 3.5, 3.6 and 3.7 show the maps and radial profiles of the velocity and σ for the three galaxies, calculated using Hγ, Hβ, [OIII] and [NI]. In all of them, the velocities are aligned to the stellar field, but the gas is clearly dominated by rotation, with higher rotational velocities and/or lower σ than the corresponding stellar kinematics.

In NGC5701 there is a correlation between the velocities of gas and stars. Also the gas presents lower σ in the centre than in the outer parts of the bulge, showing an anticorrelation between both phases.

In NGC6753, the gas traces almost exactly the radial velocity of the stars, with the velocities being compatible in the two phases. σ is always larger for the stars.

In NGC7552, the gas has larger radial velocities than the stars in the same region. The σ of the gas shows similar values than the stars, also showing the same ring-shaped region with higher σ. However, the ring is not complete, having a shape closer to a hook, probably indicating that there gas feeding the ring, which has not been able to complete a full loop around the galaxy.

3.3.4. Stellar populations through indices

A classical approach to derive stellar populations parameters from integrated spectra is the use of absorption line indices (see, for example Morelli et al., 2012; de Lorenzo-Cáceres et al., 2013; Chen et al., 2014). Among the sets of indices, Lick/IDS are the most widely used to calculate ages, metallicities and abundance ratios. While a large number of indices is available in the spectral range of our data, we only show the results obtained with a few of them, as the other are redundant. Different indices have different sensitivities to variations of age and metallicity (as well as to variations of specific chemical species). A widely used combination of indices is Hβ and MgbFe. We use indices derived from them, which are Hβ_0 (which is more insensitive to the metallicity than Hβ Cervantes and Vazdekis, 2009) and [MgFe]$'$ ($\sqrt{\mathrm{Mg}b(0.72 \cdot \mathrm{Fe5270} + 0.28 \cdot \mathrm{Fe5335})}$, Thomas et al., 2003, insensi-

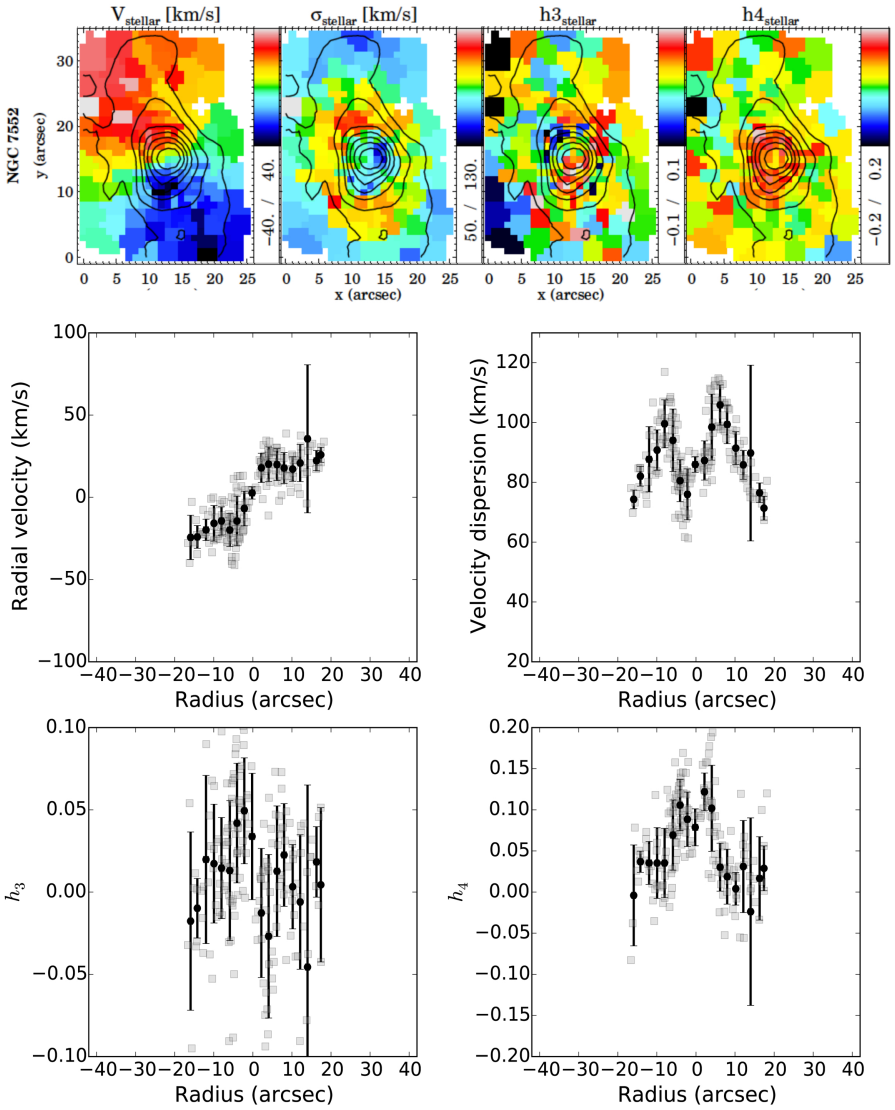

Figure 3.4: This figure show the maps and radial profiles for the velocity, σ, h_3 and h_4 for NGC7552. Symbols and colours represent the same as in Fig. 3.2

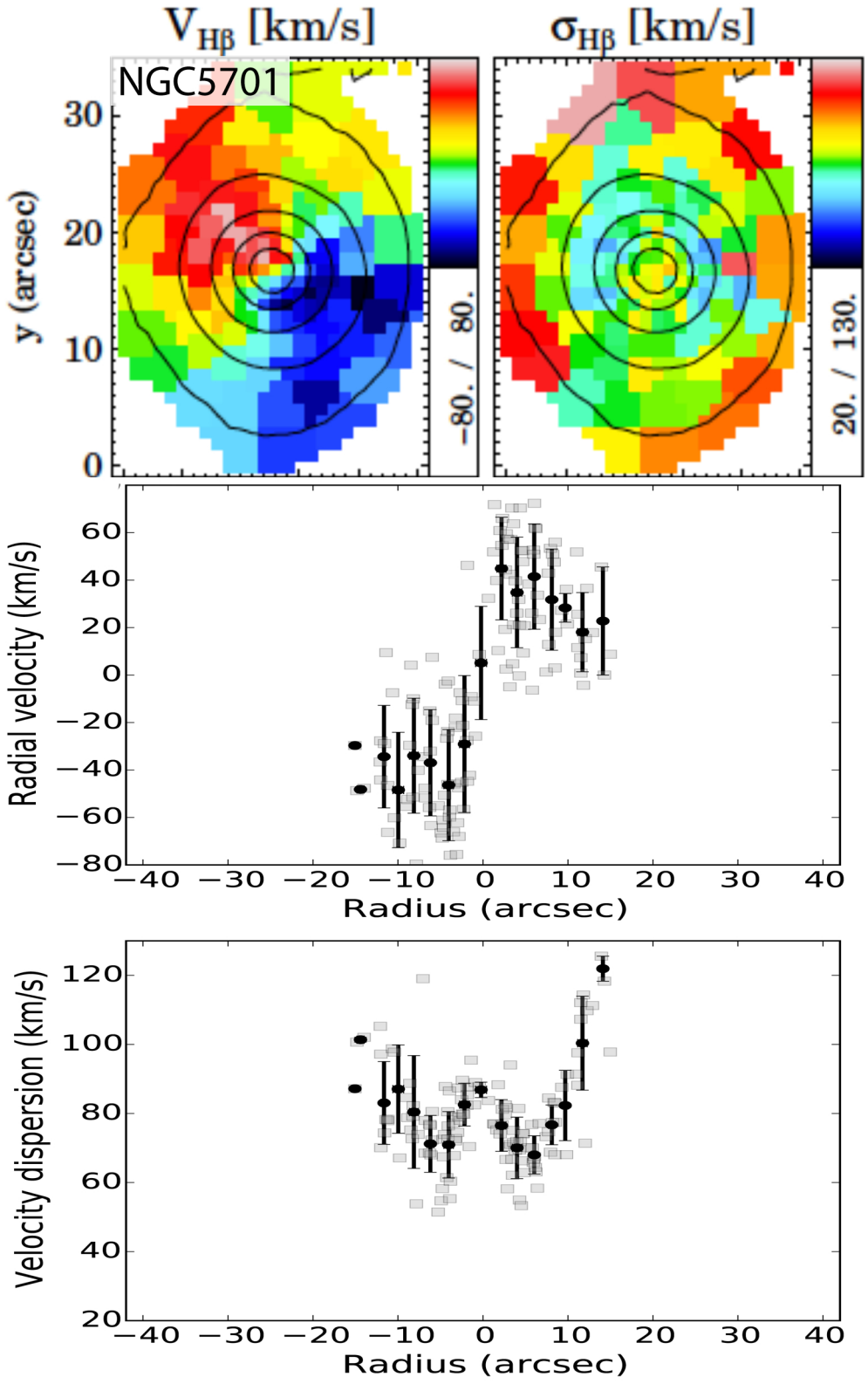

Figure 3.5: Top panels show the maps for the velocity and σ for the gas in NGC5701, calculated using the Hβ emission line (we checked that the results are consistent using other emission lines). The bottom panels show the radial profiles calculated by interpolating the values in the maps in semiannuli separated by 2 arcsec. The errorbars represent the dispersion of the bins covered by each semiannulus.

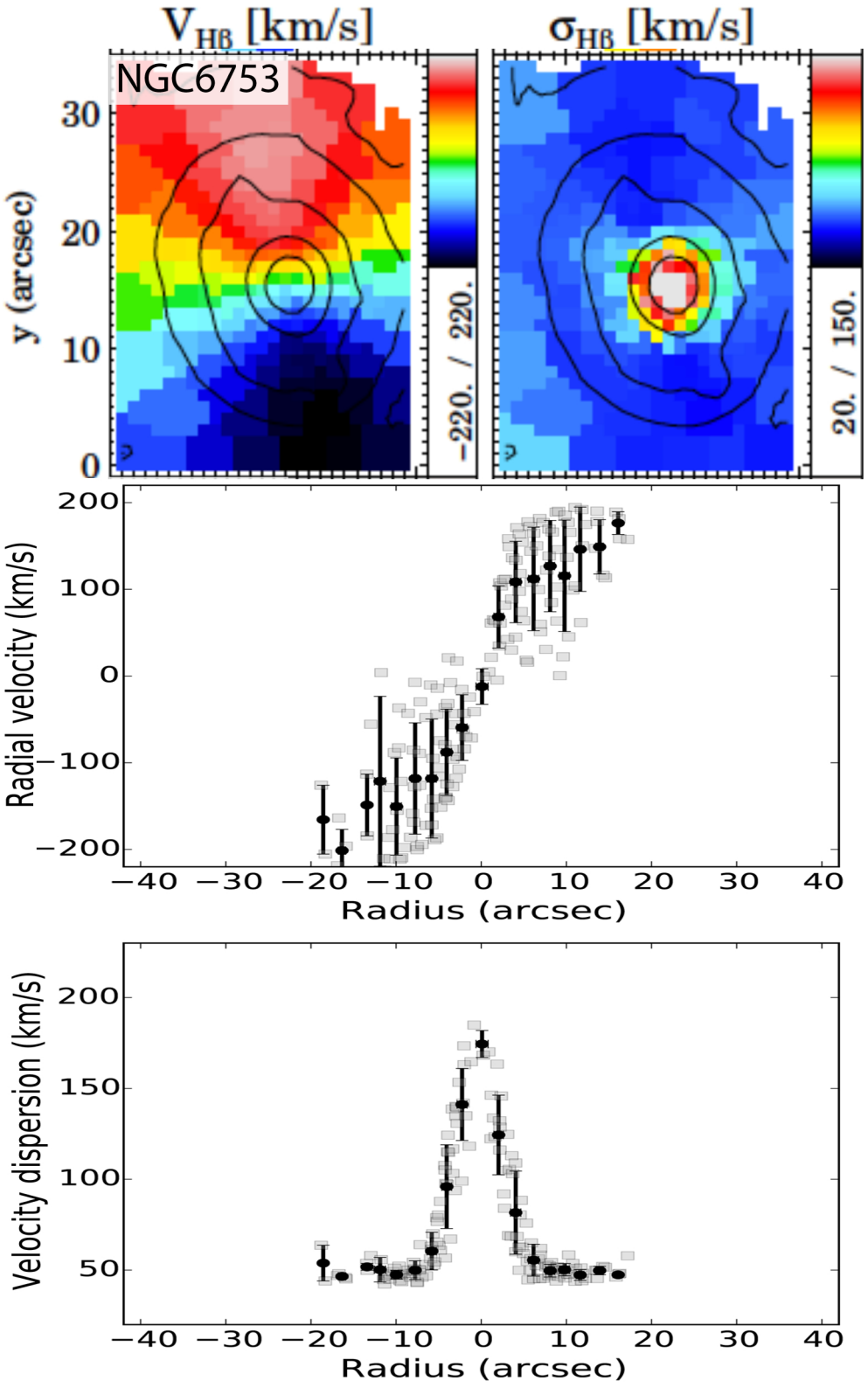

Figure 3.6: Maps and radial profiles of the kinematics in NGC6753. Symbols have the same meaning as in Fig. 3.5

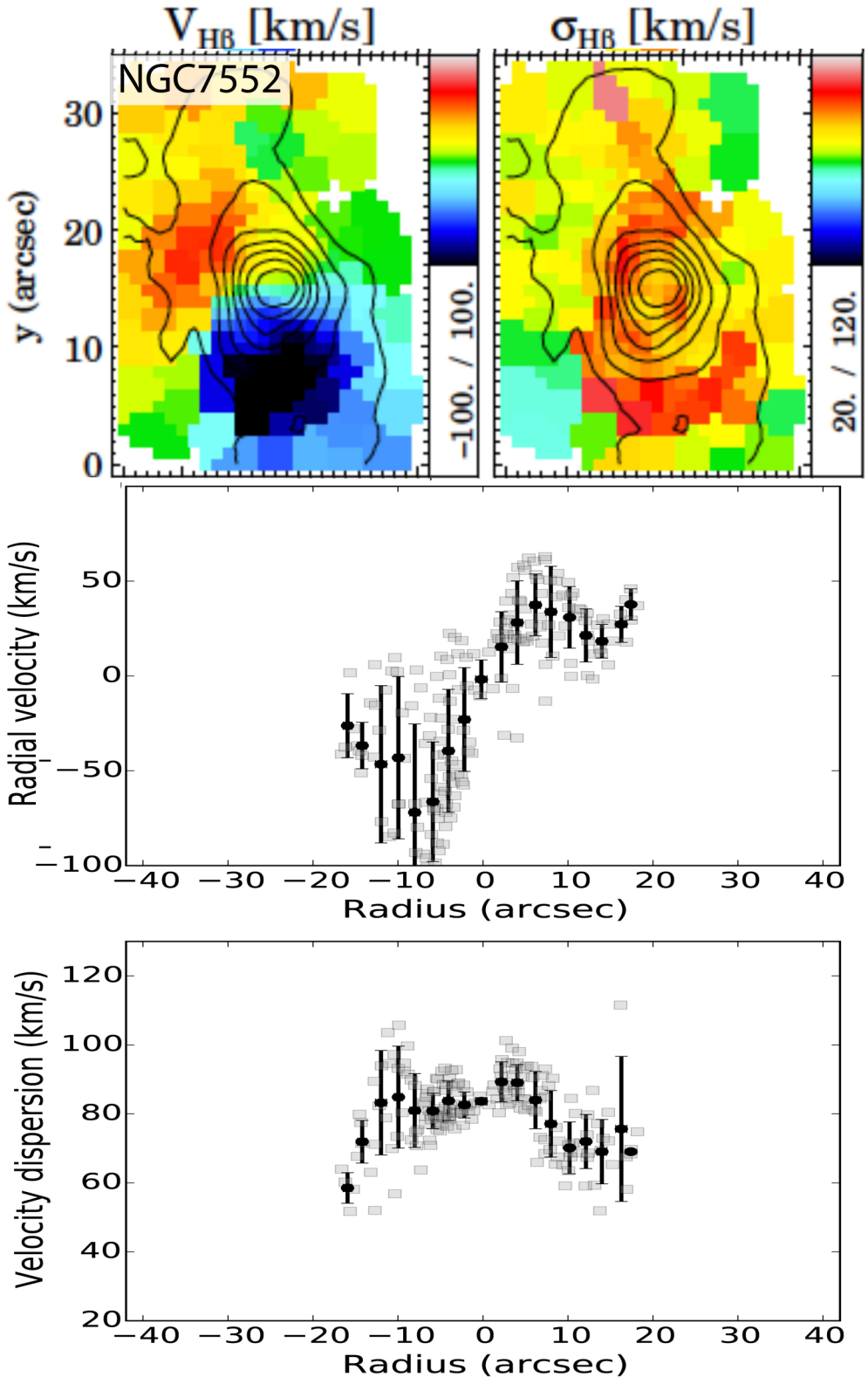

Figure 3.7: Maps and radial profiles of the kinematics in NGC7552. Symbols have the same meaning as in Fig. 3.5

tive to α/Fe variations). Once the indices are calculated, we represent one *vs.* the other and overplot an age-metallicity grid using the predictions of MILES stellar population models (Vazdekis et al., 2010) for single stellar populations of different ages and metallicities with a Kroupa IMF. By interpolating the position of our data with respect to the grid, we can estimate the age and metallicity of the region under analysis.

NGC5701 (Fig. 3.8) is the oldest of the three galaxies, with a mean age of ∼10 Gyr, with ages spanning from 3 to 15 Gyr, very independent of the radius. This scatter is larger than the error bars, but an overlapping (or dominance of) different structures in each bin may be responsible for these variations. Although there is not a clear variation of age with radius (despite the dispersion), a negative metallicity gradient is clearly seen, not only in the index-index diagram, but also in the Mgb and Fe5270 maps.

In NGC6753 (Fig. 3.9) both, an age and metallicity gradient exist, with the centre hosting older and more metal rich stars than the outskirts. The stellar ring shows younger ages and lower metallicities, but the points corresponding to this region fall out of the index-index diagrams.

The centre of NGC7552 (Fig. 3.10) is dominated by young stars (lower than 4 Gyr). At higher radius the age increases, reaching the oldest ages at the distance of the ring and then decreasing again (but not reaching ages as low as in the centre). In the Hβ_0 map two regions can be distinguished with very low values of this index. These regions are those in which the dust lanes make contact with the inner ring. This low age of the stars in these regions may be due to dust affecting the results, but also to a depletion of the star formation in the contact points, as observed by Böker et al. (2008).

The results obtained with indices correspond to a n equivalent SSP, which has the properties of the problem spectrum. If the galaxy is dominated only by one stellar population, the properties derived by the indices are close to that of the galaxy. If the galaxy is more complex, as in NGC6753, and there is not a dominant populations, some of the points derived by indices may lie out of the model predictions.We build different synthetic spectra combining two stellar populations with different contributions (in luminosity and mass). We combine two old populations (∼12.5 Gyr, solar metallicity and supersolar) with four different young populations (resulting from combining ages of 1 or 1.26Gyr and [Z/H]=0.0 or [Z/H]=0.022). We calculate the indices of these spectra, and plot them on a grid build using MILES stellar population models. As can be seen, the spectra with two different populations explains the points outside the grid in NGC6753. In the cases in which the galaxy may present different stellar populations, full spectral fitting gives better results.

Figure 3.12 shows the position of the points of these synthetic spectra

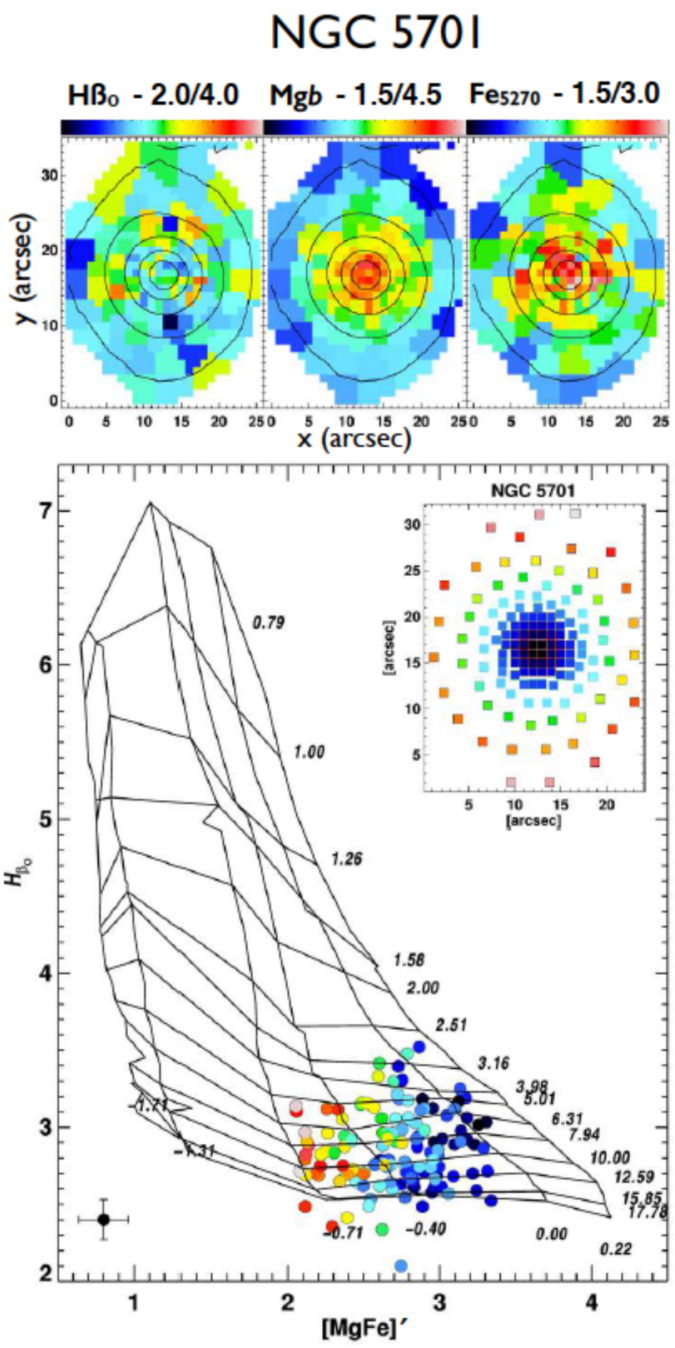

Figure 3.8: Hβ_0, Mgb and Fe5270 index maps (top panels) and Hβ_0-[MgFe]′ diagrams (bottom panels) for NGC5701. The prediction by the Vazdekis et al. 2010 models are showed in a grid for single stellar populations of constant age (vertical lines) and constant metallicity (horizontal lines) as indicated by the labels. In the bottom panels, the symbols are colour-coded,according to the distance to the centre of the galaxy (shown in a box inside each panel). The error bars show the mean uncertainty of the points.

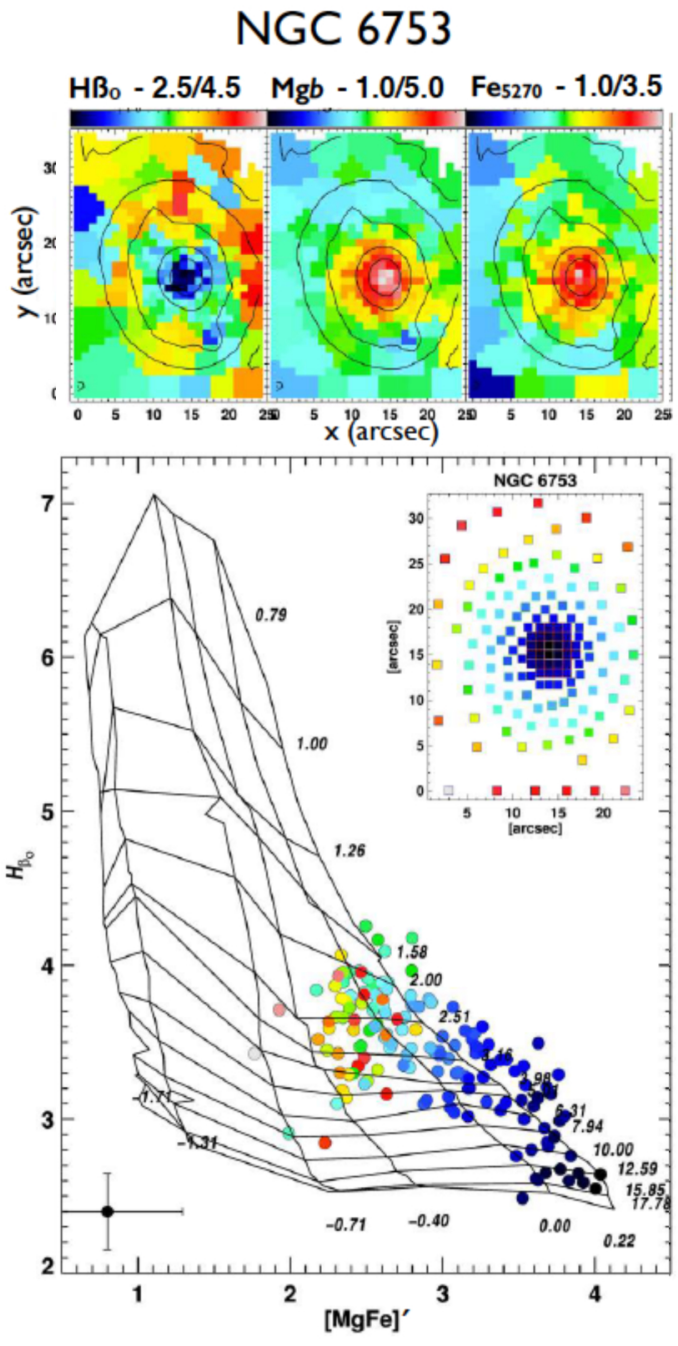

Figure 3.9: Hβ_0, Mgb and Fe5270 index maps (top panels) and Hβ_0-[MgFe]′ diagrams (bottom panels) for NGC6753. Same coding as in Fig. 3.8.

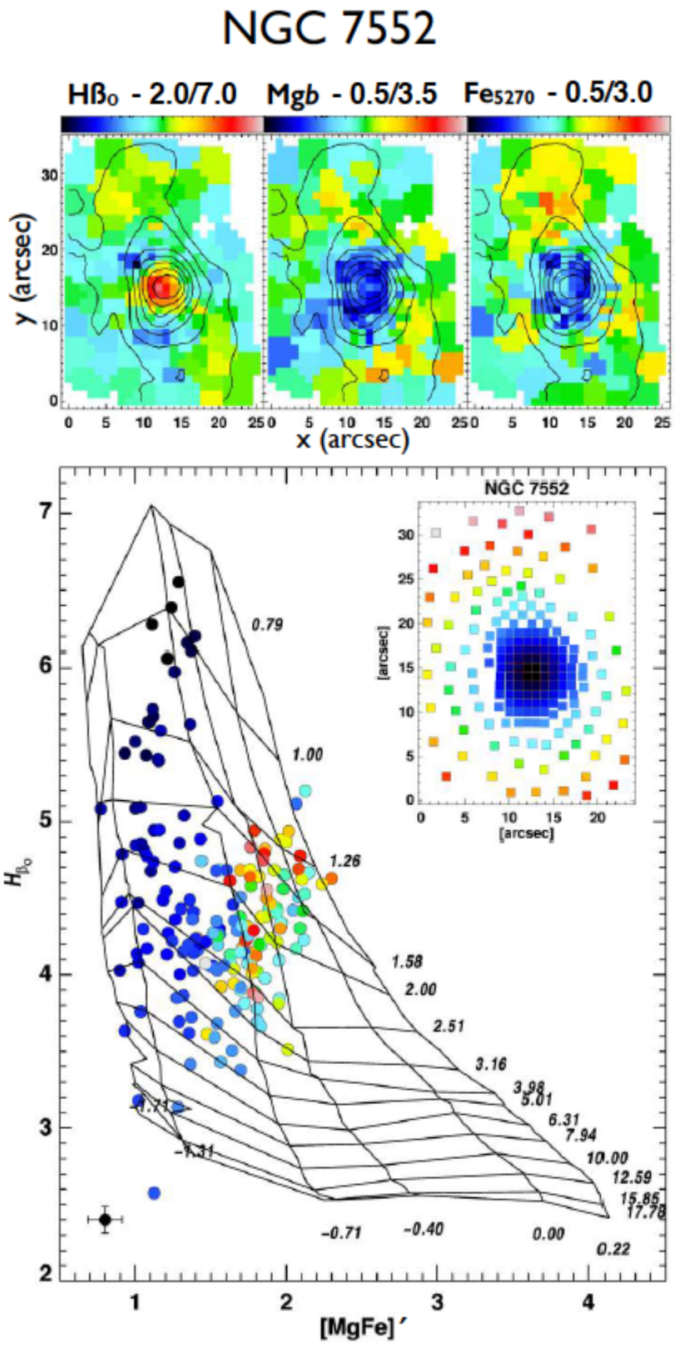

Figure 3.10: Hβ_0, Mgb and Fe5270 index maps (top panels) and Hβ_0-[MgFe]′ diagrams (bottom panels) for NGC6753. Same coding as in Fig. 3.8.

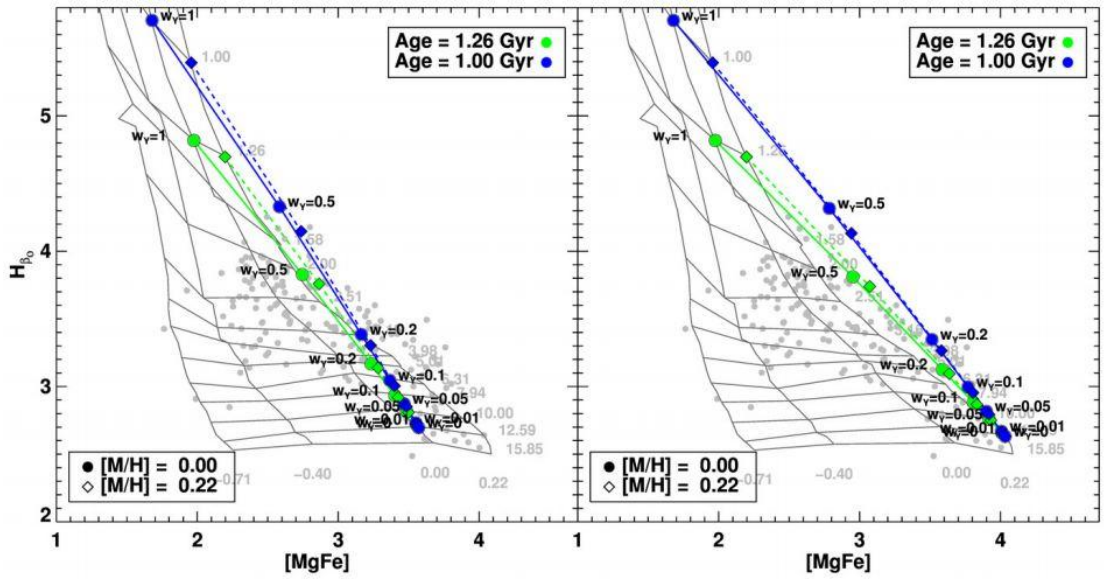

Figure 3.11: $H\beta_0$-[MgFe]′ diagram: colour lines show the measured indices in a synthetic spectrum composed of an old population (12.5 Gyr with [Z/H]=0.0 on the left panel and [Z/H]=0.22 on the right panel) and a young one (1.26 Gyr in green and 1.00 Gyr in blue). The weight of the young component is indicated in the figures. We also plot the values measured on NGC6753. As can be seen, a combination of an old and young population can result on a higher SSP-equivalent metallicity than those of the individual populations.

with respect to the predictions of the models. As can be seen, the points in which the two populations have similar contribution to the spectrum are farther away from the grid than those in which one population dominates over the other. The points of NGC6753 out of the grid can be explained by a combination of an old (∼80 % in luminosity), metal-rich stellar population and a younger component.

3.3.5. Stellar populations through full spectral fitting

3.3.5.1. Star Formation Histories

In this Setion we analyse the SFHs of the bulges as a whole. We first collapse the spectra in the datacube (with a SNR >3) in a single spectrum, for which we derive the SFH using `STECKMAP`, as in previous chapters. The SFHs of the three bulges arw shown in Fig. 3.12.

All these bulges formed the 80 % of their mass before 8 Gyr. What is unexpected is that, in NCG7552, (which is the latest-type galaxy in the sample), the 80 % of the mass is formed by stars older than 12 Gyr. This suggests a quenching of the star formation in this galaxy, which shows two more epochs of star formation at 1 Gyr and in the present.

3.3.5.2. Radial profiles

Here we use `STECKMAP` to calculate the SFHs and age-metallicity relations of the stellar populations. With these values we can calculate mean ages and metallicities (weighted by either luminosity or stellar mass) of the stellar populations contributing to the spectrum. Fig. 3.13 shows a typical output from `STECKMAP` In Section 3.3.4 we already study the distribution of the stellar content. We analyse here the radial distribution of the stellar properties.

We perform a radial binning over annular regions separated 1 arcsec. The age and metallicity at each radii is the median value of the age and metallicity of the regions falling in each annulus obtained in Section 3.3.4. Fig. 3.14 shows these radial profiles.

The luminosity-weighted values trace the stellar populations which contribute to the light of the galaxy, *i. e.*, young stellar populations. Mass-weighted values, on the contrary, trace the stellar population which contribute to the mass of the galaxy, which are the evolved stellar populations.

- NGC5701

In NGC5701 the age profile is very flat, showing old ages (>10 Gyr) and a small gradient (but smaller than the uncertainties). However, the luminosity-weighted metallicity decreases with the radius, showing solar metallicities in the centre and subsolar ([Z/H]$\simeq -0.3$) at 15 arcsec.

The mass-weighted metallicity profile in this galaxy is flatter than the luminosity-weighted one.

The comparison of (mass- and luminosity- weighted) age profiles suggest an uniform stellar distribution in the bulge, with low variations of age in the

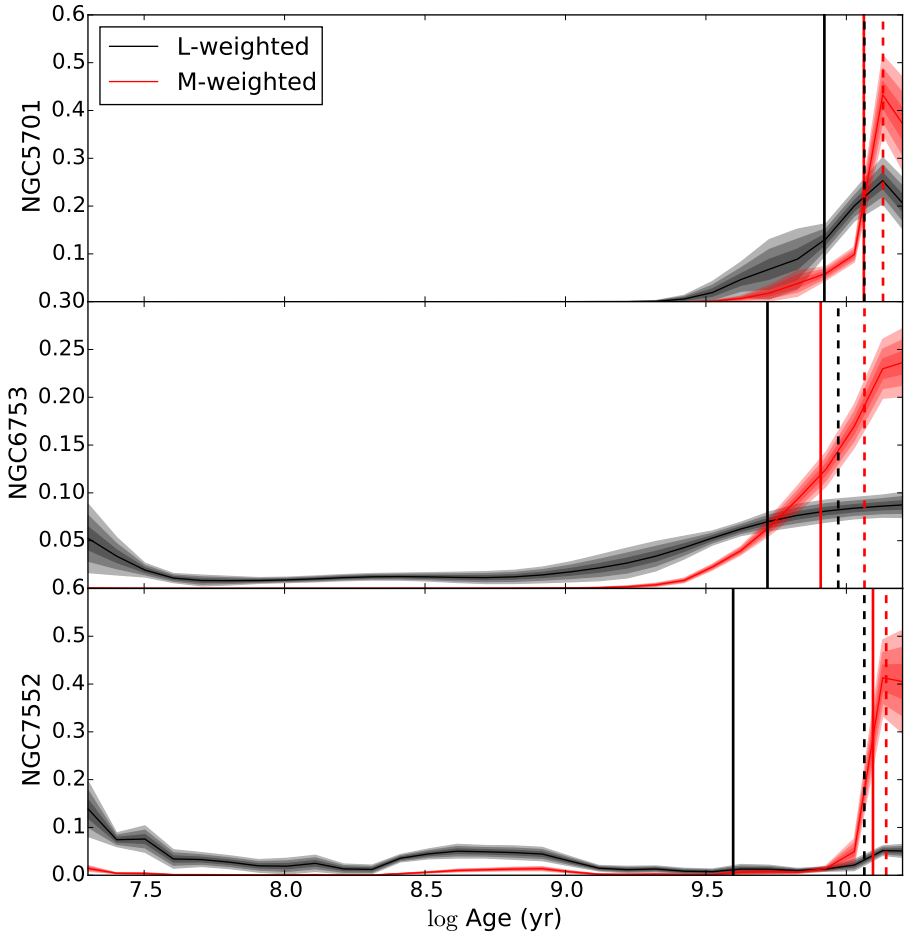

Figure 3.12: Star formation histories of the three bulges in the sample (NGC5701, NGC6753 and NGC7552, from top to bottom) derived from the integrated spectrum of the whole bulge. Black represents the SFH weighted by the mass, while red is chosen for the luminosity-weighted SFH. Shadowed regions indicate 1, 2 and 3σ deviations from the average distribution. Black (red) solid lines represent the age at which each bulge reaches 50 % of its final mass (luminosity).

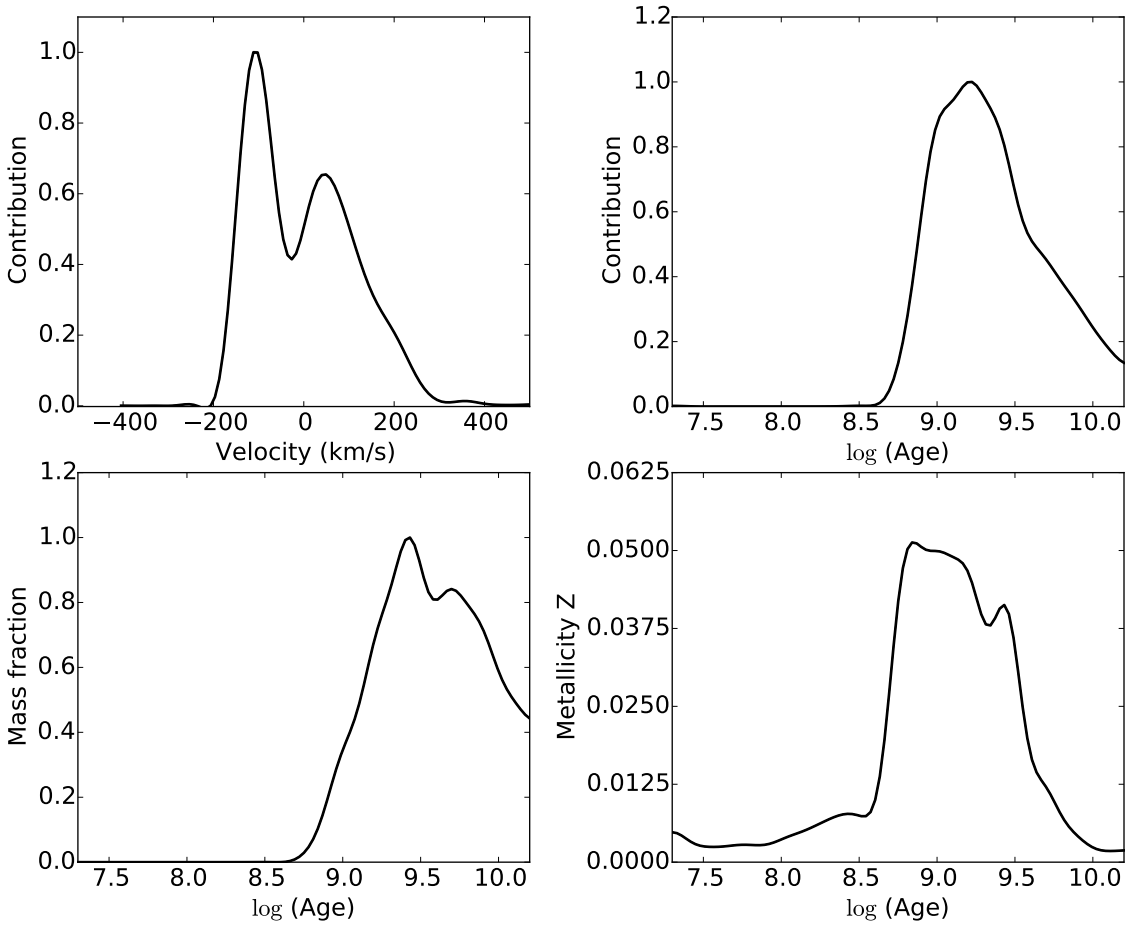

Figure 3.13: Typical output from `STECKMAP`. Top left: line-of-sight velocity distribution (LOSVd), which represents the fraction of stars with a given radial velocity. Top right: stellar age distribution (SAD), which is the contribution of the stellar populations at a given age. Bottom left: fraction of mass of the stellar populations at a given age. Bottom right: age-metallicity relation (AMR), which relates the age of the stellar populations with their metallicity. All these values are weighted by luminosity.

bulge region. Gradients in the luminosity-weighted metallicity are noticeable, going from solar in the centre to subsolar in the outer regions, as expected from the analysis with indices in Section 3.3.4. It is also remarkable that the luminosity-weighted values are high (> 10 Gyr).

- NGC6753

This galaxy is more complex than NGC5701. The age reaches its lower values between 5 and 10 arcsec, which is the region dominated by the star formation ring. This metallicity gradient is flatter in this region than in the rest of the bulge. The metallicity in the centre of the galaxy saturates, reaching the highest value in the MILES templates ([Z/H]=0.22).

The mass-weighted metallicity profile in NGC6753 is similar to the luminosity-weighted one (with the metallicity also saturating in the centre), with higher values for radii larger than 5 arcsec. Between 5 and 9 arcsec there is a bump in the mass-weighted age profile. This region corresponds to the region dominated by the star formation ring.

We know (from Hubble images) that this galaxy presents a star formation ring between 5 and 10 arcsec. In this region the luminosity and mass weighted age profiles have different shapes (the mass-weighted profile is flatter). The ring also affects the metallicity. This indicates that in the ring, the stellar populations are different than in the rest of the bulge.

- NGC7552

NGC7552 has a central starburst, reflected in the very young ages of the stars in this region (with mass weighted ages lower than 5 Gyr and luminosity weighted ages around 1 Gyr). The metallicity in the centre is high ([Z/H]~ -0.2), and decrease with radius up to [Z/H]~ -0.9 at 5 arcsec. At larger radii the metallicity increases again.

The most remarkable feature in the mass-weighted profiles is a set of points with higher ages and metallicities, represented with magenta points in Fig. 3.14. These points correspond to the ring described in Section 3.3.2 with higher σ than the rest of the galaxy. This structure is probably a classical bulge which is been shielded by the central starburst.

This galaxy is even more complex than NGC6753, as proven by the cloud of points with higher ages and metallicities (and also higher σ) which correspond to a different population with different age, metallicity and kinematics.

3.3.6. Stellar populations of different ages

So far we have compared only average values of age and metallicity. `STECKMAP` returns age and velocity distributions and an age-metallicity rela-

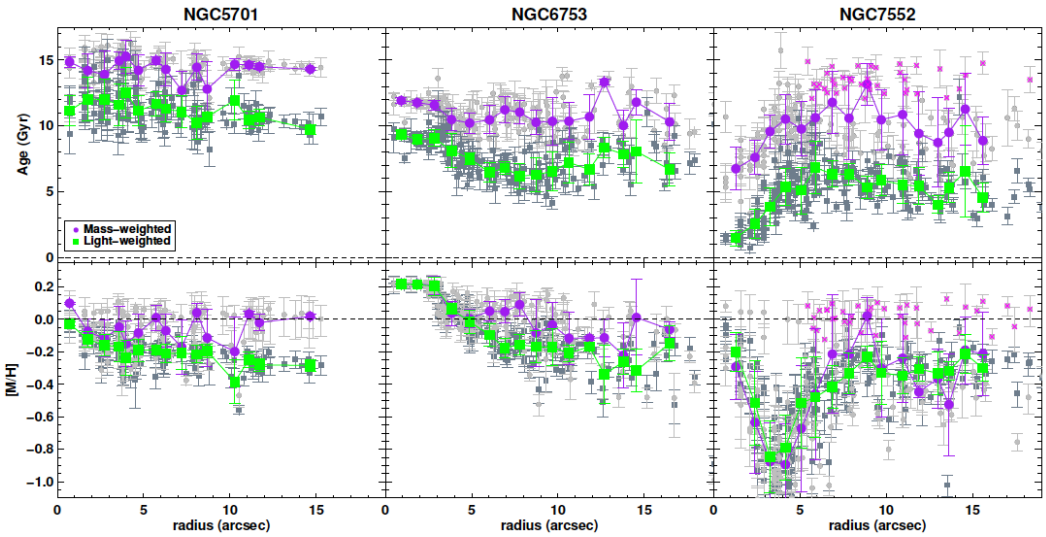

Figure 3.14: Radial distribution of mean age (first row) and metallicity (second row) obtained with `STECKMAP` for the three galaxies. Mass (purple) and luminosity (green) weighted values are shown. The results corresponding to individual unbinned spectra are shown in grey (darker for luminosity-weighted values). Magenta asterisks represent points in the ring (see details in text). Error bars represent the dispersion of the results after 25 Montecarlo simulations.

tion. Taking this advantage of STECKMAP we can study the contribution and characteristics of the stellar components at different ages.

We consider *young* those stellar populations with ages lower than 1.5 Gyr; *intermediate*, those populations with an age between 1.5 and 10 Gyr; *old* those older than 10 Gyr; and *very old* those stars older than 12.1Gyr[2].Our goal is to understand how the populations at these different ages distribute along the galactic bulge and how it was build from the different epoch of formations of the stellar populations in them.

3.3.6.1. Surface brightness

We show 2-dimensional maps of the spatial distribution of stars in different age ranges in Fig. 3.15:

NGC5701 is dominated by old and intermediate stars. The fraction of young stars is very small except in the very central region where they contribute to 12 % of the light, which is compatible with the nuclear spiral observed by Erwin and Sparke (2002).

NGC6753 is also dominated by intermediate and old stellar populations. Young stars are distributed in a ring shape, which coincides with the star formation ring in HST images.

NGC7552 is clearly dominated by young stellar populations, particularly in the core, but also distributed along the bar, which suggests that gas is been funnelled to the central region by the bar (which can also explain the kinematics of the gas-phase in this bulge; see, for example, Martin and Friedli, 1997). The intermediate age population is still significant. The old population is not negligible, being as important (in luminosity fraction) as the other two at large radii.

3.3.6.2. Stellar populations distribution

In the previous section we compared the distribution of the stellar populations attending to their surface brightness. Another way of comparing the distributions of old, intermediate and young stellar populations is computing radial profiles of their relative contribution to the luminosity in each spaxel. In this Section we binned the spectra in ellipses (before running STECKMAP to sample the same region of each galaxy.

Figure 3.16 shows the radial distributions of the stars in four different intervals of age (young stars, with ages lower than 1.5 Gyr; intermediate

[2]This extra cut is motivated because the contribution of old stars is large, and a more accurate analysis at these ages is needed.

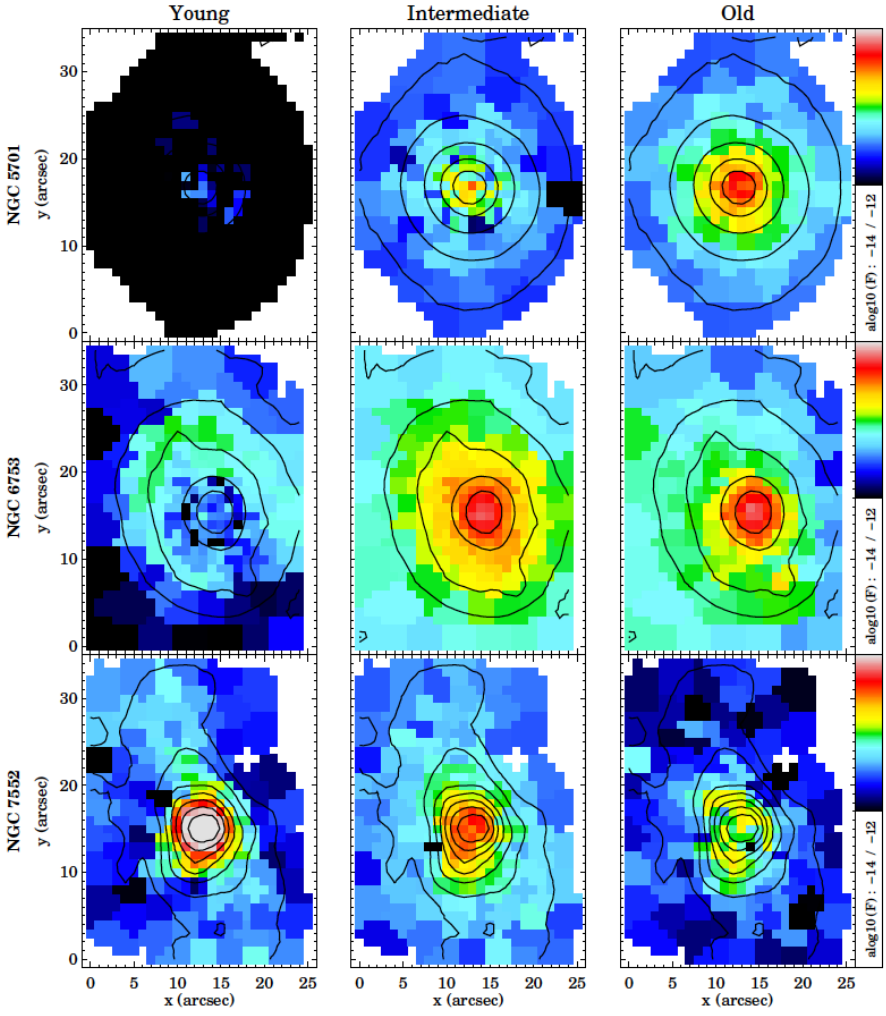

Figure 3.15: Spatial distribution of young (less than 1.5 Gyr, left column), intermediate (from 1.5 to 10 Gyr, central column) and old (older than 10 Gyr, right column) stellar populations for NGC5701, NGC6753, and NCG7552 (from top to bottom) in terms of the luminosity fraction.

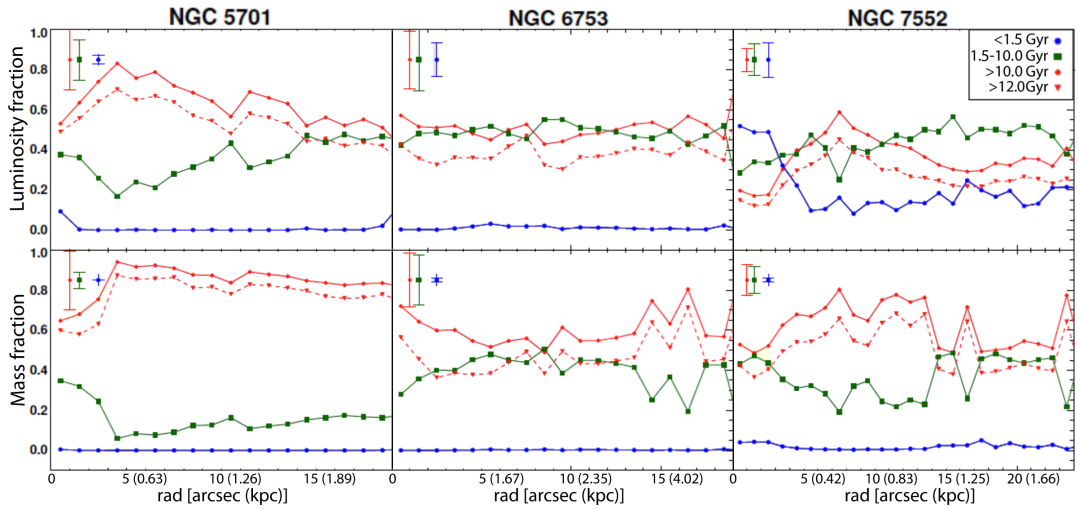

Figure 3.16: Radial profiles of the luminosity-weighted (upper row) and mass-weighted (lower row) age fraction for the young stars (blue circles), intermediate stars (green squares), old stars (red diamonds) and very old stars (red triangles), as explained in Section 3.3.6.2.

stars, with ages between 1.5 and 10.3 Gyr; old stars, older than 10.3 Gyr; and very old stars, those older than 12.0 Gyr).

We see in NGC5701 what we have been pointing out throughout this Chapter, that is a galaxy dominated by old and intermediate stars ($\sim 60\,\%$ and $40\,\%$ in luminosity, respectively) with little contribution (and only in luminosity) of young stars, probably tracing the nuclear spiral in the central 3 arcsec. This value is larger than the values found for other galaxies by MacArthur et al. (2009) at a distance of 1 effective radius (which, for NGC5701, is ~ 11 arcsec). The mass-weighted distribution shows that more than $80\,\%$ of the mass was already formed 10.4 Gyr ago not only in the centre, but along the whole bulge. Even when the uncertainties are large, the fraction of old stars is significantly higher than the fraction of intermediate stars.

In NGC6753 the differences between luminosity and mass weighted radial profiles are very subtle. Old and intermediate stars have almost the same contribution at all radii. In the region where the ring is we cannot detect more than a small bump in the luminosity fraction profile of the youngest component (in agreement with Li et al., 2011). This happens because, as we show in Fig. 3.15 the light in this region comes form the intermediate population. This means that the ring formed when the Universe had an age between 1.5 and 10 Gyr, so it can be considered a fossil ring, like those described in Erwin et al. (2001). Similarly to NGC5701, a large number

($\sim 50\,\%$) of old stars ($\geq$ 10 Gyr) are present.

The luminosity of NGC7552 is dominated by the intermediate population except in two regions. One of this region is the region between 6 and 10 arcsec, which corresponds to the region with high σ. Old stars dominate this region. The second one is the central region (<5 arcsec), which is dominated by young stellar populations, related to the central starburst. The mass radial profile shows the same results, but much less evident. There is an increase of the contribution of the young stellar populations in the region with radius lower than 5 arcsec, and a decrease of the intermediate stellar population (increasing the contribution from old stars) between 6 and 10 arcsec.

We can compare the increase in stellar mass when the galaxies were 1 and 3 Gyr old as the difference in the dashed and solid red lines in top panels of Fig. 3.16. This difference is rather constant with the radius for the three galaxies, as both (solid and dashed) red lines have the same shape. This indicates that the SFR is constant with the radius between these ages.

In NGC5701 and NGC7552 the maximum in the light contribution of youngest stars are in the very inner regions, whilst in NGC6753 the maximum is at $\sim$ 6 arcsec. NGC5701 and NGC7552 have a noticeable bar, which can funnel enough amount of gas to enhance star formation in those regions (as we explained in Chapter 2). Despite both galaxies, NGC5701 and NGC7552, have a peak in the light distribution of young stars in the central regions, the light distribution of the intermediate population is not so similar, with a higher contribution (respect to that of the young population) in NGC5701. The increase in the intermediate populations is higher (and less extended) in NGC5701 than in NGC7552, which may indicate that secular processes started earlier in this galaxy.

3.3.6.3. Comparison with the Milky Way

The finding of an old stellar component (more than 10 Gyr) in the three different types of bulges is consistent with studies in our own Galaxy. Here, colour-magnitude diagrams and spectroscopic studies can be done, and reveal that the majority of stars are older than this age (e.g., Ortolani et al., 1995; Zoccali et al., 2006; Clarkson et al., 2008). This kind of studies also reveal a metal-rich component (Babusiaux et al., 2010; Johnson et al., 2011; Ness et al., 2012) with spans a large range of ages (Bensby et al., 2013). Also, this component has a kinematics very similar to that of a bar, and can be associated with a bar formed by secular evolution in the Milky Way and the younger components found in NGC5701 and NGC7552.

3.3.6.4. Bulge evolution models

Our analysis (even with a low number of galaxies) can help to put some constraints on theoretical models to try to understand how bulges form and evolve. We have a sample of very different galaxies form early to late type spirals exhibiting typical characteristics (and therefore being representative) of their morphologies. In addition, with these different galaxies we find similarities and common results which point to a similar origin and/or evolution processes, independent of the morphological type.

We find, for example, that in the three galaxies a significant fraction (in luminosity, more than 50 % in every case, and reaching 80 % in NGC5701) of the stars are older than 10.4 Gyr. Numerical models conclude that main drivers of the formation of the first stars are gravitational collapse (White and Rees, 1978, in a ΛCDM Universe,), mergers (Hernquist, 1992; Bournaud et al., 2005; Hopkins et al., 2010), and high-z starbursts (Okamoto, 2013; Finkelstein et al., 2013). No matter what model is used, the percentage of stellar mass formed at redshift 2 is always lower than 50 %. To increase this fraction, a second star formation episode between redshifts 1 and 2 is added *ad hoc* to the models (Madau et al., 1996; Norman and Spaans, 1997; Spaans and Carollo, 1997; Daddi et al., 2010). These processes still can be mergers, collapse and starbursts in particular cases but, owing to the lower mass density because of the expansion of the Universe, it is more likely that the star formation in this epoch obeys to internal processes. These predictions are based on results concerning luminosity. Our luminosity-weighted results are in agreement with these previous works. There is an expected disagreement between our mass-weighted results with those found in the literature, as the latter use light-weighted parameters, tracing different stellar populations.

In the three galaxies we see some morphological features associated to an increase in the contribution of young and intermediate stellar populations, which reinforces the idea that these structures and stellar populations are associated to internal processes. Also the environment can affect the properties of the resulting bulge. Our sample is too small to study the effect of the environment on the bulges. However, NGC5701 is part of the Virgo supercluster, as a member of the Virgo III Group. So it has higher probability of having suffered mergers in its early stages than the other two galaxies (NGC7552 may have suffered interactions recently). This could explain the higher contribution of old and intermediate stellar populations to the mass of the galaxy at all radii.

We think that the three galaxies suffered an initial collapse in which they formed most of their stellar mass. While NGC5701 suffered more mergers, NGC6753 and NGC7552 formed in a more isolated environment, so they

could retain more material to form stars in late stages. This scenario can explain that the bulge of NGC5701 is dominated by old stars, while the bulges in NGC6753 and NGC7552 have a high contribution of young stars. Photometrically, the bulge in NGC5701 corresponds to a "classical bulge" while in NGC6753 and NGC7552, the bulges can be considered as pseudobulges, in agreement with Weinzirl et al. (2009).

3.4. Summary and conclusions

This is a pilot study for a more complete analysis to understand the stellar population of bulges and their relation to the different structures using integral field spectroscopy. We present the analysis of the kinematics and the stellar population parameters of three different galaxies hosting bulges with increasing complexity. Our aim is to characterize and quantify the properties and contribution of the distinct stellar populations in the different types of bulges to constrain the galaxy formation and evolution models. To achieve our goals, we use Integral Field Spectroscopy data with high spatial (the field of each spaxel is 1" ×11") and spectral (FWHM $\sim$ 1 Å) in a wavelength range from 3500 to 6000Å). This instrumental setup allows us to study the inner regions in galaxies with high precision, and carry on an analysis from different points of view, like indices (see Section 3.3.4) or full spectral fitting (Section 3.3.5).

We obtain 2D results in terms of different stellar ages, establish their contribution to the mass and light profiles of the galaxy, and measure the epoch of formation of each stellar component, putting limits to the galaxy formation models.

From the kinematics, ages and metallicities of the stellar populations, we deduce different formation scenarios for the three galaxies:

- NGC5701 consists basically in one stellar population with roughly solar (or slightly subsolar) metallicity. In this galaxy, up to 80 % of the mass was formed before redshift 4, being uniformly distributed along all radii. The nuclear spiral, despite it is a very weak feature, is detected by means of the light contribution. The stellar bar does not appear as a different stellar population, probably because the bulge dominates the spectra in the FoV of the instrument or because it is an old bar formed by stellar populations similar to that in the bulge (Sánchez-Blázquez et al., 2011).

- In NGC6753 we find an old metal-rich centre, extremely high σ outside the core and a significant proportion of intermediate-age stars. The

stellar component of the inner ring is detected in the h_4 map, and is consistent with the detection of the emission lines from the ionized gas. Nevertheless, the main stellar component in this galaxy is, again, old , with ages $\geq$10.4 Gyr.

- NGC7552 presents three different components: an inner starburst ring, a high σ ring and a disc component. The inner ring is detected as a large contribution of the young stellar populations in this region, which present a wide range of metallicities, from solar to sub-solar. The inner side of the ring is formed by an old, metal-poor component, followed into a region where two components can be distinguished, one with intermediate stars and solar metallicity and a young one with subsolar metallicity, trend which continues at higher radii. As happened for the other two galaxies, a significant fraction of the stellar mass comes from *very old* stars.

We find that, for every morphological type, the stars are formed at the very beginning of the life of the galaxy. This is particularly true for early type galaxies. We find the importance of the bar in the evolution of these three galaxies, as the two barred ones in the sample present a high contribution of young stars in the central regions, which is not found in NGC6753.

We compare our results with the simulations. Our observations are compatible with a two stage scenario for the formation of the bulge, as predicted by Obreja et al. (2013), which consists in a rapid formation of an old bulge structure followed by a slower formation of a second bulge component. However we find a disagreement in the amount of mass formed. We find that between 50 % (in late type galaxies) to 80 % (in early type galaxies) of the mass is formed by stars older than 10 Gyr, while simulations predict less than 50 %. This suggests a higher efficiency in the star formation in the past, or different evolutionary paths.

We are aware of the low number of galaxies in our sample, so we do not claim that our results are representative of all galaxies. However, all our results point to the same conclusion, which is the high fraction of stars formed in the early epochs of the Universe.

Chapter 4

Disentangling stellar populations

4.1. Introduction

We show in Chapter 3 the importance of disentangling the stellar populations underlying the galactic bulges. There we characterized the bulges of three galaxies of different morphologies, from early to late type galaxies (NGC5701, NGC6753 and NGC7552). This analysis reveals that bulges are complex structures, and that the classification of bulges and pseudobulges not only obeys to photometric reasons, but also to different underlying components.

In Chapter 3 we separated old, intermediate and young stellar populations by making cuts in the stellar age distribution at 1.5 and 10 Gyr. However, this cuts do not attend to any physical reason, but the convenience of redshifts 0.1 and 2[1], which are found very often in the literature. However, to understand the physical processes leading to the formation of galactic bulges is necessary to disentangle the stellar populations properties (age and metallicity) of all the different components that constitute this structure, differentiating them through their kinematics and morphology. This is a very complicated task, as the effect that metallicity, age, and velocity dispersion have on the absorption lines can be similar. Furthermore, recovering the star formation history of several subcomponents from an integrated spectrum is an ill conditioned problem (*e.g.* Moultaka and Pelat, 2000; Moultaka et al., 2004).

Studies focusing on decoupling the stellar populations are very recent. Apart from Seidel et al. (2015) there are some previous works which are

[1]with a ΛCDM cosmology with H_0=68.14 km/s/Mpc, and Ω_M=0.30. However, the conversion of ages to redshift is only approximate, as the stellar population ages span to 17.8 Gyr, which is much larger than the current estimates of the age of the Universe (13.4 Gyr).

worth to summarize here. Coccato et al. (2011, 2013, 2014) disentangled the populations kinematically by synthesising the spectrum using two components; but only for counter-rotating discs or polar rings which have different kinematics. Johnston et al. (2013) recovered the spectra of two components by a bulge-disc photometric decomposition at each wavelength of the whole spectrum for a sample of S0 galaxies; assuming that only this two components are present. Our starting point is more similar to Ocvirk et al. (2008), in which the characterize the kinematics and age of the bulge and the disc in NGC4030 using full spectral fitting with `STECKMAP`. Despite the kinematics and ages are free parameters, they had to fix the metallicity, which can bias the results because of the age-metallicity degeneracy.

In this Chapter we develop a new technique to disentangle stellar populations, which constitutes a step forward with respect to the methodology used before. Now we are able to determine not only the ages of the stellar populations, but also their individual kinematics and metallicities without making an a priori assumption about the number of stellar subcomponents. We only make two hypothesis: 1) the star formation history of each component follows a delayed τ-model and 2) the velocity of the individual components follows a Gaussian distribution.

4.2. Sample and observations

The data used here consists in the same three galaxies that we analysed in Chapter 3. For more information about the sample and observations, see Section 3.2

4.3. A new method to disentangle stellar populations

The method we have developed has the following steps:

- Run `STECKMAP` to recover the stellar age distribution (SAD), line-of-sight velocity distribution (LOSVd) and the age-metallicity relation (AMR).

- Calculate the mean velocity and the velocity dispersion (σ) from the previous step and re-run `STECKMAP` fixing these parameters. With this step, we minimize the effect of age-σ and Z-σ degeneracies (Koleva et

al., 2008b; Sánchez-Blázquez et al., 2011). This is explained in more detail in Section 4.3.1.

- Estimate the number of stellar populations in the galaxy from the age and velocity distributions using Bayesian statistics (see 4.3.2 for details).

- Fit the age distributions with delayed τ-models and the velocity distribution with Gaussian curves, with a number of distributions equal to that estimated in the previous step (see 4.3.3). A delayed τ-model has the following expression:

$$SFR = A \cdot (t - t_0) \cdot e^{\frac{t_0 - t}{\tau}}$$

, for $t < t_0$, with t_0 being the age at which the star formation begins, and τ the time scale of the starburst. We will consider the age of the population, the age at which the maximum of the SFR is, which corresponds to $t_0 - \tau$

- Associate the parameters of the distribution. We will explain this step in more detail in Section 4.3.4.

Before analysing the galaxies with this methodology, we run a series of tests to check the reliability of the technique and to tune the parameters in `STECKMAP`. These parameters consist in a set of smoothing values and operators (see Sect. 2.4 for more details), which are used to regularize the solution given by `STECKMAP`. This regularization consists in penalizing sharp distributions, favouring smooth solutions. These tests are made using synthetic spectra, resulting from a combination of stellar populations with different ages, metallicities, kinematics and contributions to the spectrum. Also, different shapes for the SFH of the populations are considered. With these tests we study how this methodology behaves in different situations, specially how it deals with degeneracies and its weak points in *difficult* situations, where the individual stellar populations have similar properties. The information about the characteristics of the stellar populations included in each test is summarized in Table 4.1.

Test	Contribution (%)	Velocities (km/s)	σ (km/s)	Age (log yr)	[Z/H]	SFHs
1	[0.5, 0.5]	[0, 0]	[100, 100]	[10, 1]	[0.0, -0.4]	Delta
2	[0.5, 0.5]	[0, 100]	[100, 100]	[10, 1]	[0.0, -0.4]	Delta
3	[0.5, 0.5]	[0, 100]	[100, 50]	[10, 1]	[0.0, -0.4]	Delta
4	[0.85, 0.15]	[0, 0]	[100, 100]	[10, 1]	[0.0, -0.4]	Delta
5	[0.85, 0.15]	[0, 100]	[100, 100]	[10, 1]	[0.0, -0.4]	Delta
6	[0.85, 0.15]	[0, 100]	[100, 50]	[10, 1]	[0.0, -0.4]	Delta
7	[0.15, 0.85]	[0, 0]	[100, 100]	[10, 1]	[0.0, -0.4]	Delta
8	[0.15, 0.85]	[0, 100]	[100, 100]	[10, 1]	[0.0, -0.4]	Delta
9	[0.15, 0.85]	[0, 100]	[100, 50]	[10, 1]	[0.0, -0.4]	Delta
10	[0.5, 0.5]	[0, 0]	[100, 100]	[10, 1]	[-0.4, 0.0]	Delta
11	[0.5, 0.5]	[0, 100]	[100, 100]	[10, 1]	[-0.4, 0.0]	Delta
12	[0.5, 0.5]	[0, 100]	[100, 50]	[10, 1]	[-0.4, 0.0]	Delta
13	[0.85, 0.15]	[0, 0]	[100, 100]	[10, 1]	[-0.4, 0.0]	Delta
14	[0.85, 0.15]	[0, 100]	[100, 100]	[10, 1]	[-0.4, 0.0]	Delta
15	[0.85, 0.15]	[0, 100]	[100, 50]	[10, 1]	[-0.4, 0.0]	Delta
16	[0.15, 0.85]	[0, 0]	[100, 100]	[10, 1]	[-0.4, 0.0]	Delta
17	[0.15, 0.85]	[0, 100]	[100, 100]	[10, 1]	[-0.4, 0.0]	Delta
18	[0.15, 0.85]	[0, 100]	[100, 50]	[10, 1]	[-0.4, 0.0]	Delta
19	[0.5, 0.5]	[0, 0]	[100, 100]	[5, 5]	[0.0, -0.4]	Delta
20	[0.5, 0.5]	[0, 100]	[100, 100]	[5, 5]	[0.0, -0.4]	Delta
21	[0.5, 0.5]	[0, 100]	[100, 50]	[5, 5]	[0.0, -0.4]	Delta
22	[0.85, 0.15]	[0, 0]	[100, 100]	[5, 5]	[0.0, -0.4]	Delta
23	[0.85, 0.15]	[0, 100]	[100, 100]	[5, 5]	[0.0, -0.4]	Delta
24	[0.85, 0.15]	[0, 100]	[100, 50]	[5, 5]	[0.0, -0.4]	Delta
25	[0.15, 0.85]	[0, 0]	[100, 100]	[5, 5]	[0.0, -0.4]	Delta
26	[0.15, 0.85]	[0, 100]	[100, 100]	[5, 5]	[0.0, -0.4]	Delta
27	[0.15, 0.85]	[0, 100]	[100, 50]	[5, 5]	[0.0, -0.4]	Delta
28	[0.5, 0.5]	[0, 0]	[100, 100]	[10, 1]	[-0.4, -0.4]	Delta
29	[0.5, 0.5]	[0, 100]	[100, 100]	[10, 1]	[-0.4, -0.4]	Delta
30	[0.5, 0.5]	[0, 100]	[100, 50]	[10, 1]	[-0.4, -0.4]	Delta
31	[0.85, 0.15]	[0, 0]	[100, 100]	[10, 1]	[-0.4, -0.4]	Delta
32	[0.85, 0.15]	[0, 100]	[100, 100]	[10, 1]	[-0.4, -0.4]	Delta
33	[0.85, 0.15]	[0, 100]	[100, 50]	[10, 1]	[-0.4, -0.4]	Delta
34	[0.15, 0.85]	[0, 0]	[100, 100]	[10, 1]	[-0.4, -0.4]	Delta
35	[0.15, 0.85]	[0, 100]	[100, 100]	[10, 1]	[-0.4, -0.4]	Delta
36	[0.15, 0.85]	[0, 100]	[100, 50]	[10, 1]	[-0.4, -0.4]	Delta
37	[0.25]	[0]	[100]	[1, 10, 1, 10]	[0.0, 0.0, -0.7, -0.7]	Delta
38	[0.16, 0.84]	[300, 10]	[100, 300]	[8.8, 10.1]	[0.40, 0.13]	Delayed τ
39	[0.16, 0.84]	[250, 5]	[50, 200]	[8.8, 10.1]	[0.49, 0.46]	Delayed τ
40	[0.33, 0.66]	[200, 5]	[50, 350]	[9.6, 9.6]	[0.46, 0.34]	Delayed τ
41	[0.09, 0.91]	[100, 200]	[200, 400]	[8.1, 9.5]	[0.28, 0.21]	Delayed τ
42	[0.77, 0.08, 0.15]	[250, 100, 5]	[50, 50, 200]	[8.7, 8.9, 10.1]	[0.49, 0.20, 0.11]	Delayed τ
43	[0.44, 0.56]	[100, 300]	[300, 10]	[9.6, 59]	[0.00, 0.18]	Delayed τ
44	[0.82, 0.18]	[200, 50]	[5, 250]	[9, 10.1]	[0.00, -0.70]	Delayed τ
45	[0.64, 0.36]	[350, 50]	[5, 200]	[9.7, 10.1]	[-0.30, 0.0]	Delayed τ
46	[0.38, 0.62]	[100, 400]	[200, 200]	[10.1, 8.13]	[0.28, 0.21]	Delayed τ
47	[0.60, 0.27, 0.13]	[50, 200, 50]	[250, 5, 100]	[8.9, 9.5, 10.1]	[0.40, 0.00, -0.30]	Delayed τ

Table 4.1: Parameters of the tests. From left to right: test number, contribution to the flux of the spectrum of the different subcomponents, mean velocity, velocity dispersion, mean age, mean metallicity and star formation history of the stellar populations inclueed in each spectrum.

To illustrate the methodology in the following sections we use the test number 47 (see Table 4.1 for more info) because it is the most complex of all of them. The conclusions concerning the rest of test cases can be found in Section 4.3.6.

4.3.1. Free vs. fixed kinematics

We run `STECKMAP` (masking the emission lines in a region as narrow as possible) for each individual spectrum. with Pegase-HR models (Le Borgne et al., 2004; Prugniel et al., 2007) as basis.

The analysis of stellar populations through full spectral fitting is affected by several physical degeneracies, in particular the age-metallicity and the metallicity-sigma degeneracies. The first one is greatly reduced when a full spectral fitting is performed (as opposed to a Lick-indices analysis Conroy, 2013; MacArthur et al., 2009; Sánchez-Blázquez et al., 2011) while the second can be greatly reduced by fixing one of the two parameters (sigma or metallicity Chilingarian, 2006; Koleva et al., 2008a). We first calculate the LOSVd[2] and then recalculate the SAD fixing the velocity and the velocity dispersion as mean and the standard deviation of the LOSVd. Using Montecarlo (MC) simulations, uncertainties can be estimated for each distribution.

Figure 4.1 shows a comparison between the results obtained with free and fixed kinematics. As can be seen SAD and AMR are different with free and fixed kinematics. The choices which best replicated the input in the tests resulted from taking the SAD and the AMR when the kinematics is fixed.

4.3.2. Estimating the number of stellar populations

Estimating the age, metallicity, radial velocity and velocity dispersion for an undetermined number of stellar populations from a single spectrum is an ill-conditioned problem with too many parameters. One way to reduce the number of parameters is to assume the shape of some of the distributions. In particular, we consider that the star formation history can be described by a delayed τ-model and that the line-of-sight velocity distribution is shaped as a Gaussian.

A key step of the procedure is the derivation of the number of stellar populations in a particular region. As we are using parametric models, we can minimize a statistical indicator of the fit to the global distribution using a number of individual distributions. χ^2 is a widely used estimator, but it has the issue that it tends to decrease with the number of parameters (the

[2]We calculated it using `GANDALF`.

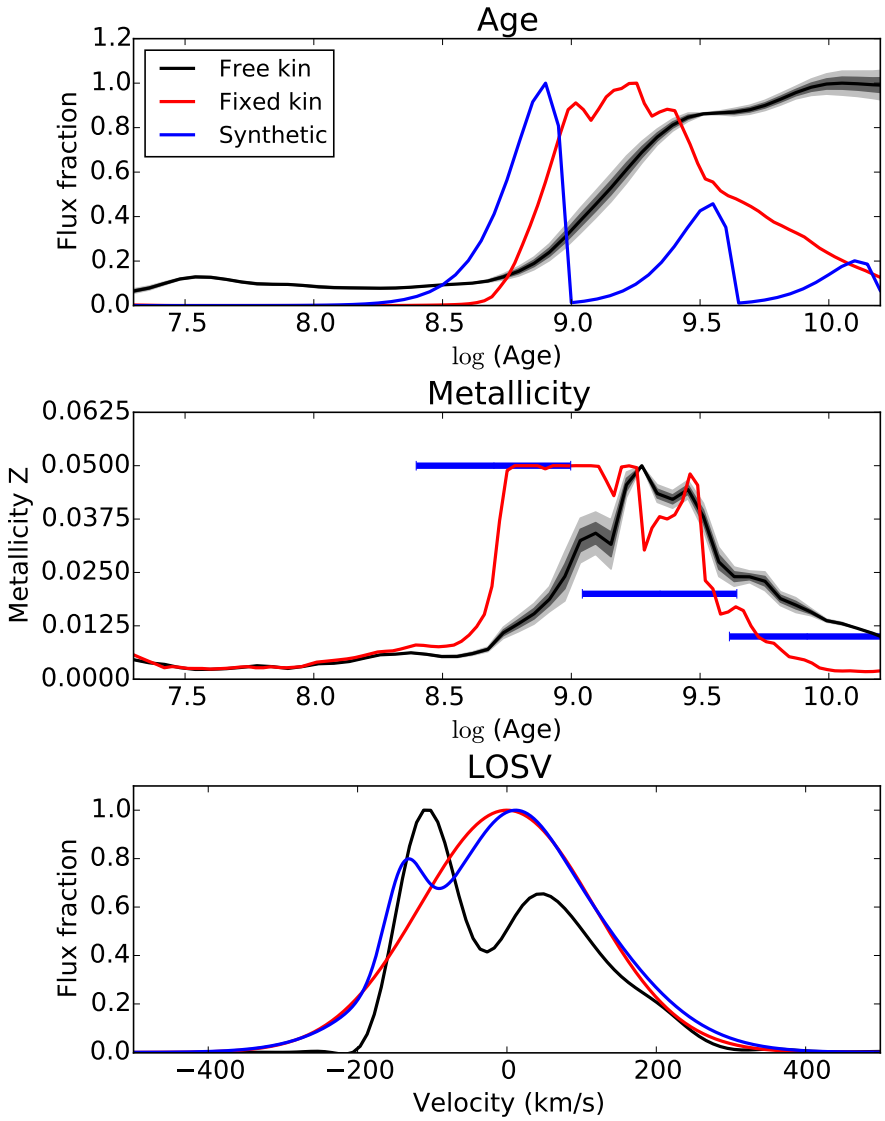

Figure 4.1: Comparison of the stellar age distribution (top panel) and age-metallicity relation (middle panel) with free (black), fixed (red) kinematics and for the synthetic spectrum (blue). Bottom panel shows a comparison between the calculated velocity distribution (black) and a Gaussian curve with the same mean and standard deviation. The different intensities (from dark to light) in the colour indicate 1, 2 and 3σ deviations from the calculated value at each point.

number of different stellar subcomponents, in our case; see, *e.g.* Mighell, 1999, 2000).

To decide how many different components are contributing to the integrated spectrum we have decided to use the Bayesian Information Criterion (BIC, Schwarz, 1978). This criterion basically consists in adding a penalization to the estimator of the quality of the fit when the number of populations is increased. A revision of the results is made to ensure that the number of populations and their characteristics are reasonable.

We start by fitting the SAD and LOSVd with a number of components that can vary from 1 to 6. For each number of components we run 500 MC simulations. In each MC simulation we choose different initial fitting values (age and velocity) of each component in a random way, following a probability distribution equal to the SAD or LOSVd. We choose the solution with the lowest BIC of the 500 MC simulations.

Figure 4.2 shows the estimation of the number of stellar populations based on BIC and χ^2 for the test case used as example. As can be seen, χ^2 decreases monotonically with the number of populations, whilst the BIC reaches a minimum when the number of populations is 3. In the bottom panels, we plot the fits which the estimators suggest.

A closer look to the fits shows that one of the three populations has a contribution compatible with zero, and age and kinematics similar to one of the other populations, so we consider those two populations as just one SSP. In the next section (4.3.3) this is explained with more detail.

4.3.3. Fitting the distributions

In the previous section we fit the distributions modifying only the initial conditions. Now, to derive uncertainties, we keep fixed the initial conditions and modify the points to be fitted. We run 500 MC simulations in which we take, at each age or velocity, a random value from a Gaussian distribution centred on the mean value and a width equal to the dispersion of the values given by `STECKMAP`. The "initial conditions" for the fit are the same in each MC simulation and are those obtained in the previous step. In total we derive eight parameters for each stellar population, which are: $w_{age,i}$, the contribution (measured as a luminosity fraction) to the stellar age distribution; $A_{0,i}$, the age of the first stars of each stellar population; τ_i, the time between $A_{0,i}$ and the maximum of each distribution; $w_{vel,i}$, the contribution (in luminosity, again) to the velocity distribution; v_i, the mean velocity of the stellar population; σ_i, its velocity dispersion; Z_i, the mean metallicity calculated as the weighted average of the AMR with the age distribution of each population;

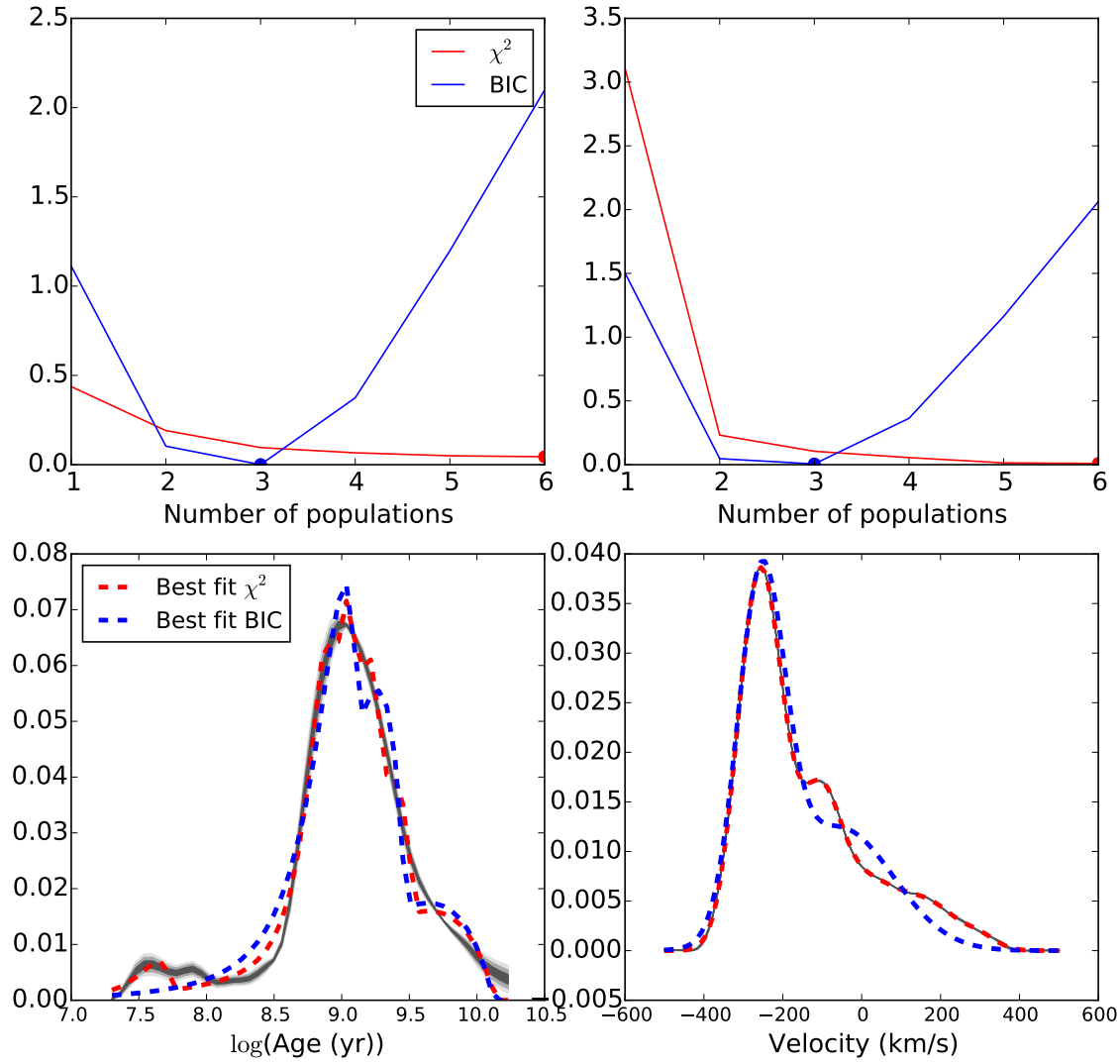

Figure 4.2: Estimation of the number of populations. Using the stellar ages distribution (SAD, on the left) and the line of sight velocity distribution (LOSVd, on the right), both in grey lines, derived from `STECKMAP`. Top panels show the variation of BIC and χ^2 values, normalized for better comparison. Bottom panels show the distributions and the fits which minimize BIC and χ^2.

and $\sigma_{Z,i}$, which is the weighted standard deviation of the metallicity.

Usually the results are given in the form "*mean* $\pm$ *uncertainty*". This assumes that the uncertainties follow a Gaussian distribution, which may not be true. Instead of this, we give the uncertainties as a density function built with the results of the MC simulations described in the previous paragraph. These density functions give the probability that a parameter takes a given value. Figure 4.3 shows the density functions of the parameters calculated for the three populations in this test.

Figure 4.4 shows the fits for the SAD and the LOSVd using the three populations, considering the values which best fit these distributions using three different stellar components.

4.3.4. Associating parameters

Up to now we have disentangled the kinematics and the age distribution of the stellar population separately, but we have not related one with the other yet.

`STECKMAP` returns an AMR relation, which gives the metallicity of the stars at a given age. It also returns the SAD, which gives the flux fraction as a function of the age of each population. The luminosity-weighted value of the metallicity of each stellar population is calculated simply as the average of the AMR weighted with the SAD of each individual stellar population.

To relate ages and kinematics, we first thought about using the contribution of the SSPs to the SAD and the LOSVd. However, they are not necessary the same. This makes necessary an assumption, which is to consider that older populations have larger velocity dispersion. This assumption is based on observational evidence in the Milky Way of an age-sigma relation (Nordström et al., 2004; Holmberg et al., 2007) and on observations of bulges with integral field units, suggesting that young populations, when present, are associated to colder kinematics, which still preserve their initial angular momentum.

For a better visualization of the results, we designed age-metallicity-kinematics (AMK) diagrams, based on the age-kinematics diagrams in Ocvirk et al. (2008), but including the metallicity. In the AMK diagrams, the age, metallicity and kinematics of each individual stellar population can be seen at first sight. The diagram for the testcase used is shown in Fig. 4.5, which will be explained in detail in the next section.

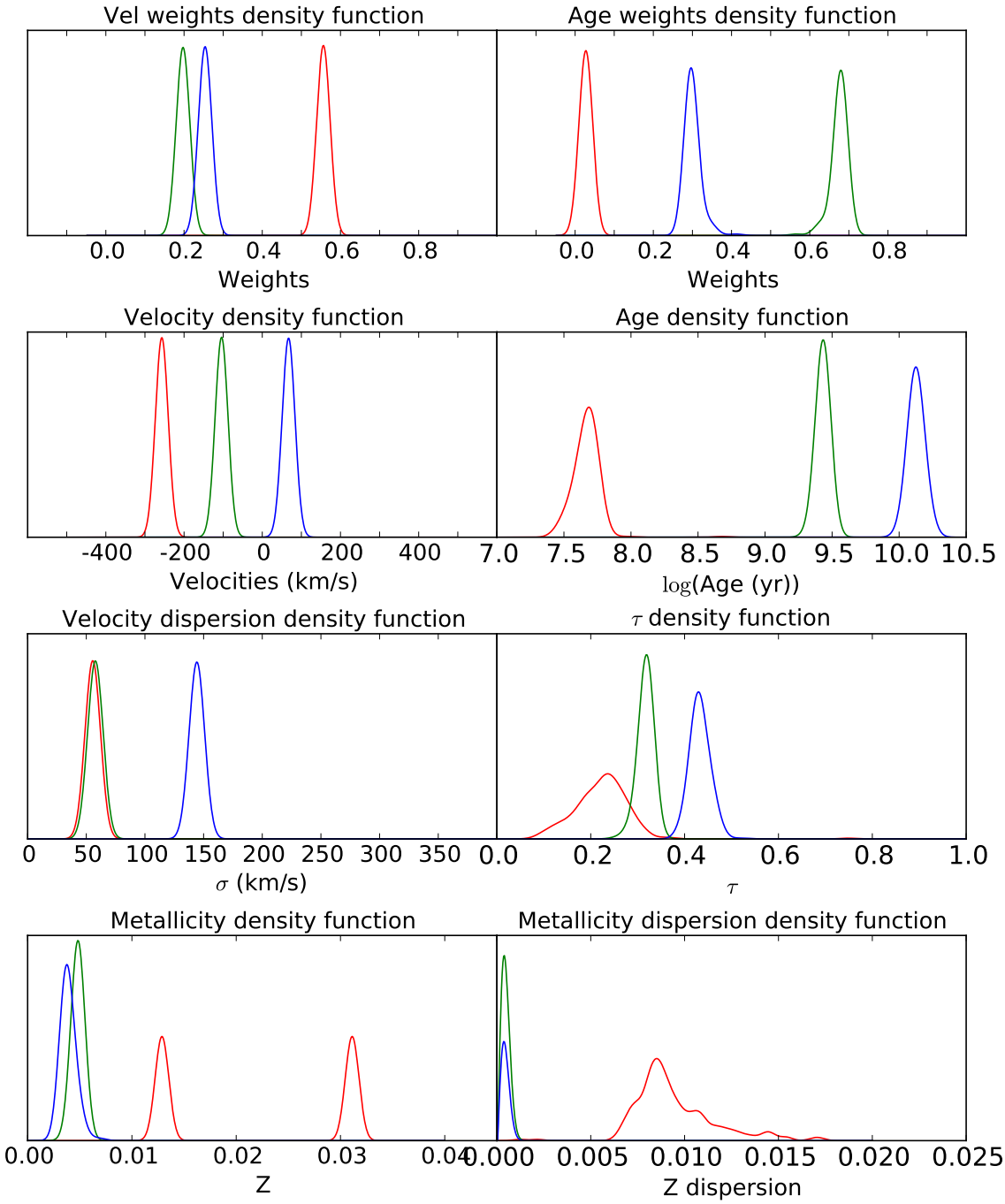

Figure 4.3: Density functions of the eight values calculated for the testcase serving as example (see details in text).

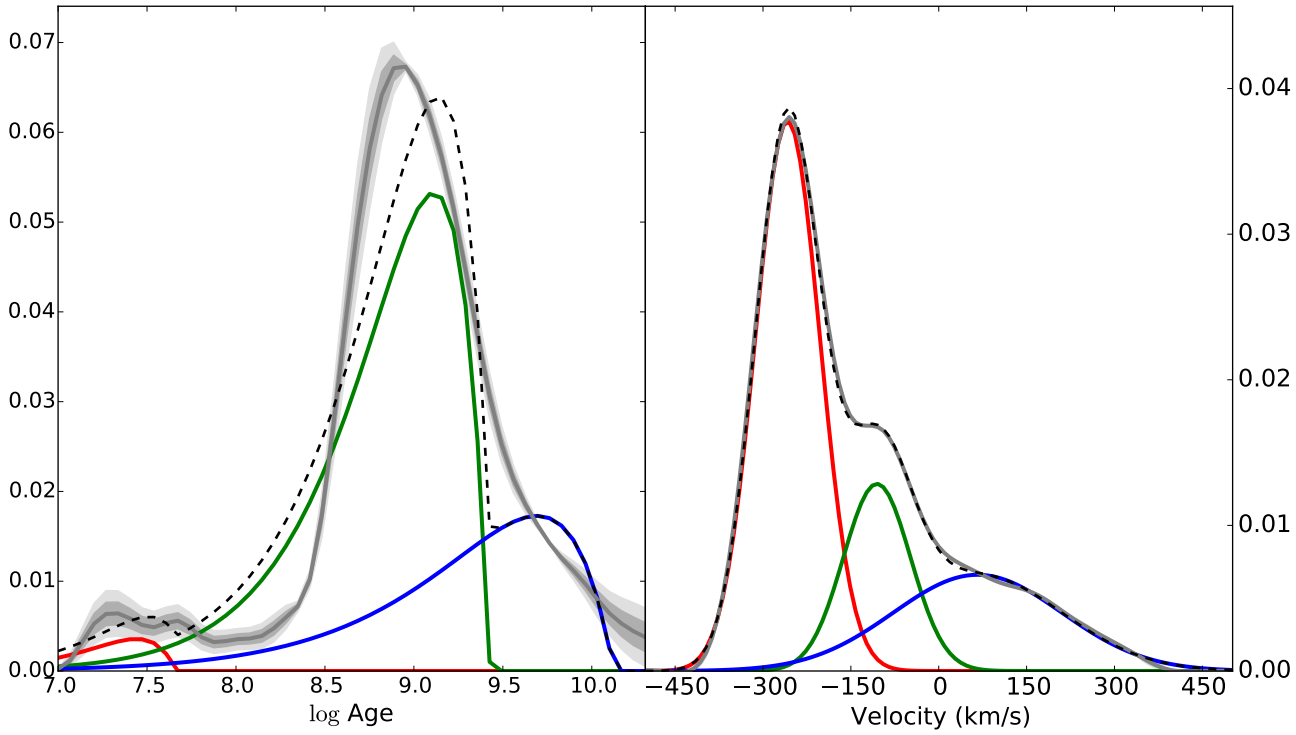

Figure 4.4: Fitting with the three populations derived for the test case.

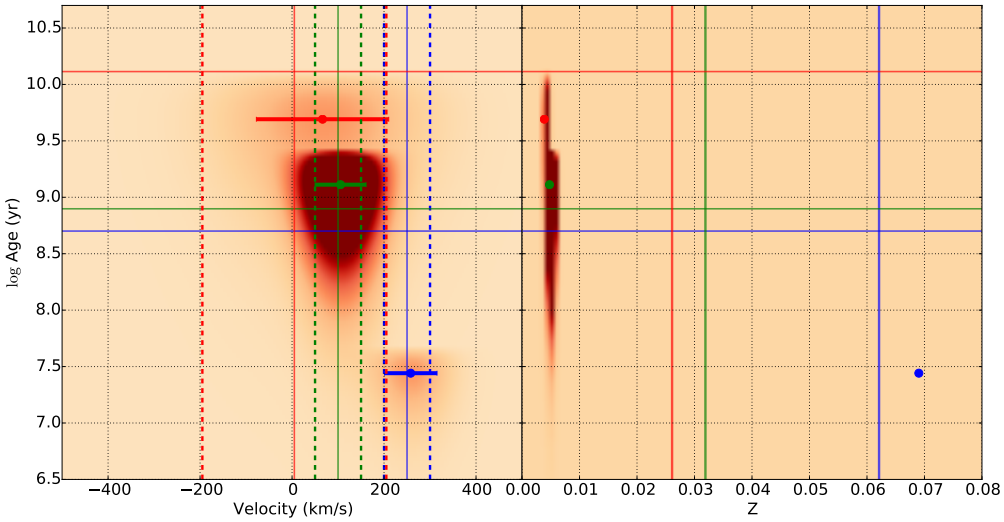

Figure 4.5: Age-metallicity-kinematics diagram for the test case number 47. On the left, a representation of the age vs. the velocity is displayed. On the right, the age vs. the metallicity. The intensity of the shadow is proportional to the flux fraction of stars at that given age, metallicity and kinematics. Red, green and blue dots represent the maximum of the age and velocity distributions and the error bars indicate the recovered velocity dispersion of each population. Solid lines represent the values of the age, metallicity and kinematics chosen for the synthetic spectrum. Dashed red and black vertical lines represent the velocity dispersion of the populations from which the spectrum was built.

4.3.5. Input vs. output

For this test case we recover two stellar populations, which are very easily seen in Fig. 4.5. In the diagrams shown in this figure, if this methodology worked perfectly, the dots should fall exactly on the intersections of the solid lines, and the error bars should extend up to the dashed vertical lines. This happens for the kinematics and ages, where all the parameters are compatible with the input (given the uncertainties in the parameters). For the metallicities, there is less agreement, but the uncertainties in these parameters are larger than in the kinematics.

In the next table we summarize the results obtained for this particular test case and the input values used to produce the synthetic spectrum.

Parameter	Input 1	Recovered 1	Input 2	Recovered 2	Input 3	Recovered 3
$Weight$	0.77	0.03	0.076	0.67	0.15	0.30
$\log(Age$ (Gyr))	8.71	7.66	8.89	9.42	10.1	10.1
v (km/s)	-250	-257	-100	-105	-5	-66
σ (km/s)	50	57	50	55	200	143
Z	0.069	0.062	0.032	0.005	0.026	0.004

Table 4.2: Comparison of the recovered values and the input values.

4.3.6. A big set of tests

We chose one of the tests (test number 47) to illustrate how the methodology works. Apart from that, we ran a large series of tests, combining a different number of stellar populations, with different kinematics, ages, metallicities and star formation histories. In total, more than 40 different combinations were tested, with the same spectral resolution, wavelength range and similar SNR than the spectra of the galaxies in the sample. The combinations were chosen to cover a lot of points in the parameters space, putting especial attention on the degeneracies.

The main conclusion is that the combination of `STECKMAP` and the decomposition works well in most of the cases, always recovering at least the age and kinematics with small errors. The metallicity values are more difficult to recover, but we can always stablish an approximate age-metallicity relation (*i.e.*, the method works at establishing if the younger population is also more metal rich or the other way around). However, there are some issues we had to learn to deal with:

- In some cases the SAD shows a contribution of an extremely young stellar population. We know that this population is spurious because

we observed it using synthetic spectra, in which we know the age distribution. Moreover, if we modify the age limits in which the SFH is calculated, this young population always appears at the lower limit. With the expertise in our group using `STECKMAP` we know that the solution is to increase the precision in the calculation of the SNR. After calculating the SNR with several algorithms, the option which estimates the SNR with higher accuracy is the algorithm DER_SNR (Stoehr et al., 2008, recommended by the International Virtual Observatory Allianz[3]). This method consists in comparing the median signal with the median noise to estimate the SNR of the whole spectrum. When a reliable estimator of the SNR is included in `STECKMAP`, the spurious young population disappear from the solution.

- For some tests only one Gaussian curve is necessary to fit the LOSVd, but more than one delayed τ-models are necessary to fit the SAD. In these cases we assume that both populations have the same kinematics, and we split that Gaussian curve in two (Gaussian) velocity distributions with the same mean velocity and velocity dispersion and a contribution to the total LOSVd equal to the contribution to the SAD

- If the spectrum is dominated by old stars, it is more difficult to recover the young populations when separating the age distributions. For instance, in "test case 4" we recovered only a 5 % of young stellar populations, whilst the input was 15 %. However, if the spectrum is dominated by young stars, the scenario is the best possible one.

- We test also what happens if there are two stellar populations with the same or similar ages. In this case, `STECKMAP` cannot recover properly the SAD, because it works with mean properties at a given age. What happens here is that the SAD is spread. However, we still can recover the stellar populations, but at a cost of a large spread in the metallicity distribution.

- When a spectrum is composed by four different stellar populations (in our particular case, resulting of the combination of two ages (1 and 10 Gyr) and two metallicities (0.02 and 0.004), each of them with the same contribution to the total luminosity and kinematics, which makes it highly degenerated) the methodology recovers two stellar populations with ages very similar to that of the input. The kinematics can be fit with only one Gaussian curve centred on zero and a width close

[3]http://www.ivoa.net/documents/latest/SpectrumDM.html

to the input velocity dispersion. Therefore, even when the case is as degenerated as possible, we can still estimate the stellar populations contributing to the spectrum.

- Metallicity is the most affected parameter by degeneracies, especially when several stellar populations are combined. The uncertainties in the metallicity are large, and sometimes absolute values of the metallicity are not reliable. Moreover, STECKMAP does not return metallicity distributions (as it does for the age and the velocity), but the mean metallicity of the stars at a given age. However, even in cases in which absolute values are not good, we can still conclude if a stellar population is more or less metal-rich than other.

It is worth mentioning that we have built synthetic star formation histories to test the method and, in some cases, we have thought of those scenarios that are more difficult to recover. For example, sometimes we have assumed that the properties of the different subcomponents are very similar (and, therefore, difficult to disentangle with STECKMAP. We have also tested the method with star formation histories consisting in instantaneous bursts with different metallicities. this type of scenario is very difficult to recover with STECKMAP, as this code favours those solutions where the fluxes and metallicities change smoothly with time. Star formation histories in observed galaxies should be easier to recover with our method.

4.3.7. The methodology on real data

Now it is time to move to the real galaxies, in which the process is almost exactly the same as for the test cases, but needs some adjustments.

First of all we have to reach enough SNR to obtain reliable results. Our aim when planning the observations was $SNR \geq 100$ in the inner regions, as suggested by Ocvirk et al. (2008). However, owing to bad weather, this is not possible. For this reason we have to bin the data. We binned the galaxies in three regions, one of them covering the central parts of the bulge, and the other two symmetric respect to the kinematical axis found in Section 3.3.2. Fig. 4.6 shows the three regions overprinted on an image built by collapsing the data cube.

STECKMAP does not impose a priori conditions, except positive and smooth solutions. The smoothness can be controlled by means of a series of parameters which can be tuned in STECKMAP. We used the test cases to adjust the smoothing parameters, but some fine tuning is still necessary, as the smoothing parameters not only depend on the instrumental setup, but also on the

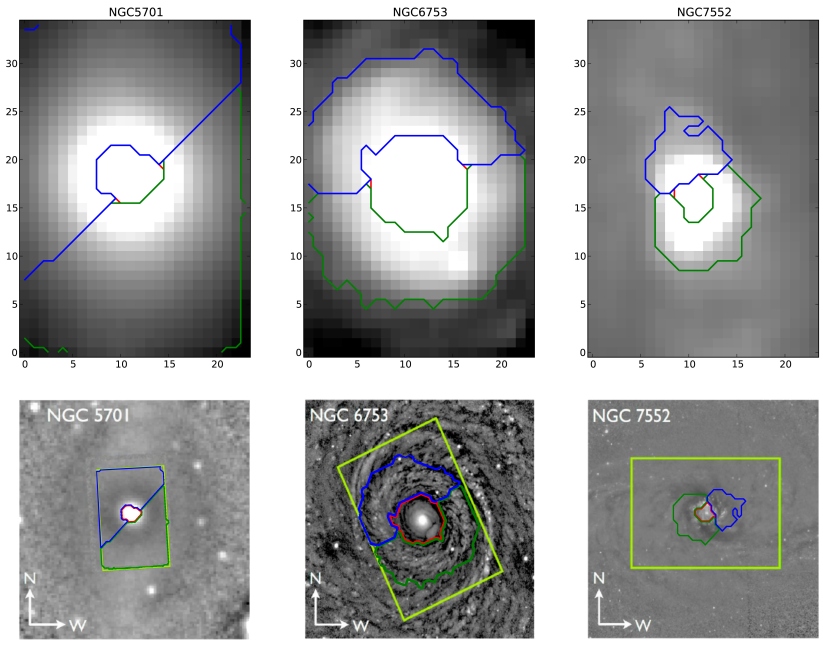

Figure 4.6: Binning of the spectra in the three galaxies of the sample. The images are built by collapsing the data cube along the spectral direction. The overprinted contours indicate the regions from which the spectra are binned.

particular spectrum.

When estimating the number of components, we run a large number of simulations with random initial conditions, trying to find the best possible fit in terms of BIC. However, "large" does not necessarily mean "large enough", especially when the distributions are not smooth. In some cases a visual inspection of the fit reveals that it is not good enough (even when it has a good BIC). For example, in NGC5701 (see Fig. 4.7), there is a population of young stars (log Age $\simeq$ 7.2) which is not included in the best fit considering BIC. We think that this population is real, as the contribution is compatible with being larger than zero, and it appears in the two outer regions. In these cases we have to disobey the statistics, and stablish by hand the initial conditions or the number of components, always from a conservative point of view, trying not to include spurious populations, and checking that the BIC is similar to the best one obtained with the random initial conditions.

Figures 4.7, 4.8 and 4.9 show the estimation of the number of stellar populations for the three galaxies in our sample. We proceed to analyse the three galaxies separately.

After this step for the three galaxies, we end up with three populations for NGC5701 and NGC6753, and four populations for NGC7552. Their properties are discussed in the next Section.

4.4. Results

We have decomposed the stellar populations in the three bulges. Figs. 4.10, 4.11 and 4.12 show the AMK diagrams for all of them.

4.4.1. NGC5701

Figure 4.10 shows the AMK diagrams for NGC5701, in which we find three different components.

We find two very old components ($>$ 10 Gyr) with a low rotational velociy and a large velocity dispersion. The metallicity of these old stellar populations is subsolar in the central bin, but supersolar in the outer regions. However, the uncertainties in the metallicity are too large to extract any conclusions about gradients in metallicity. The two old populations are similar in age, but the differences in the metallicity are significant. Although the two populations appear to have similar velocities, they show apparent differences in the velocity dispersion.

We also find a young population (log Age $\simeq$ 7.2) with the same stellar

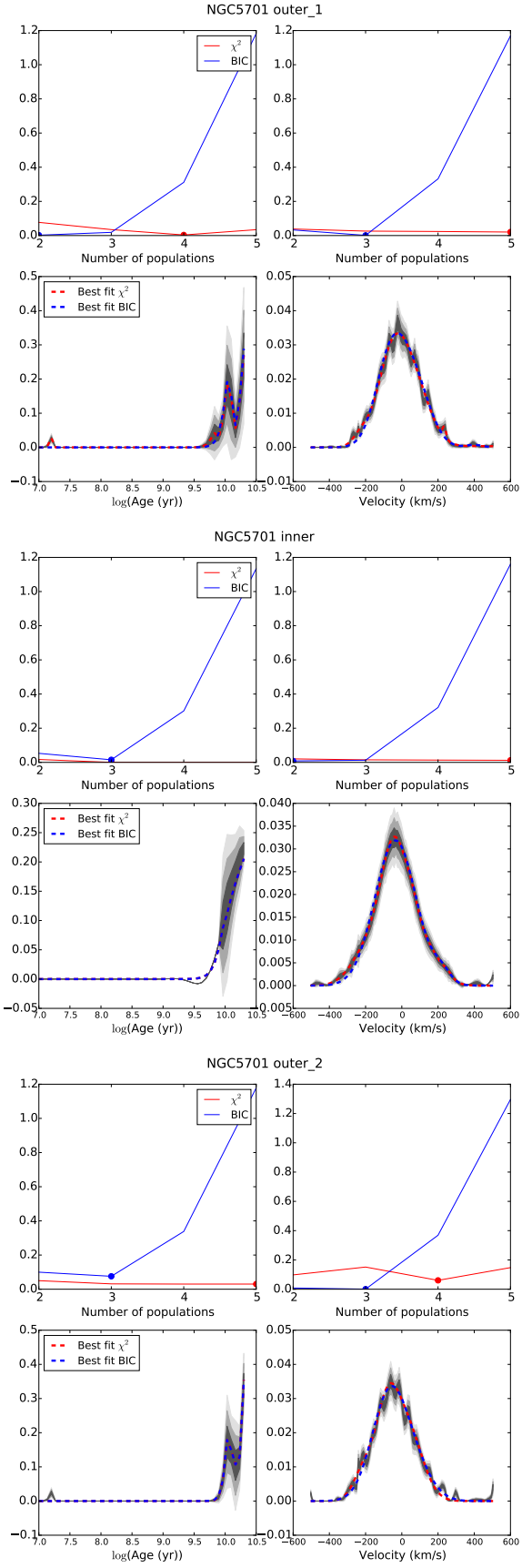

Figure 4.7: Estimation of the number of populations for the three regions in NGC5701. This figure is similar to Fig 4.2, using the same colour coding.

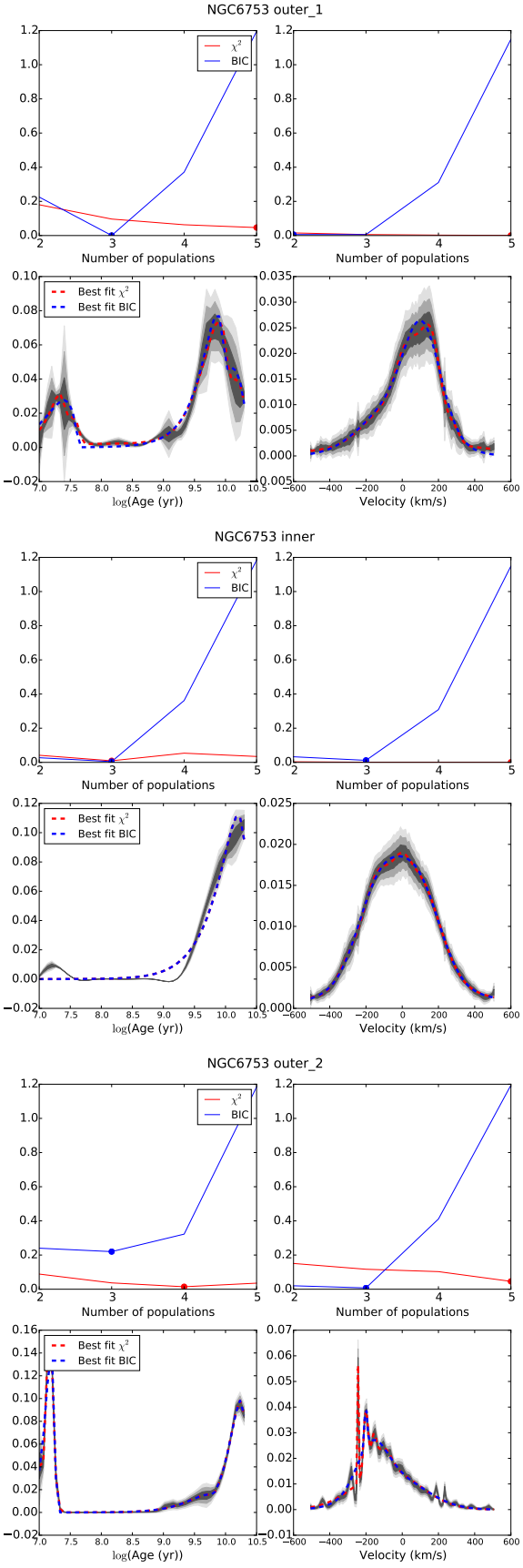

Figure 4.8: Estimation of the number of populations for the three regions in NGC6753.

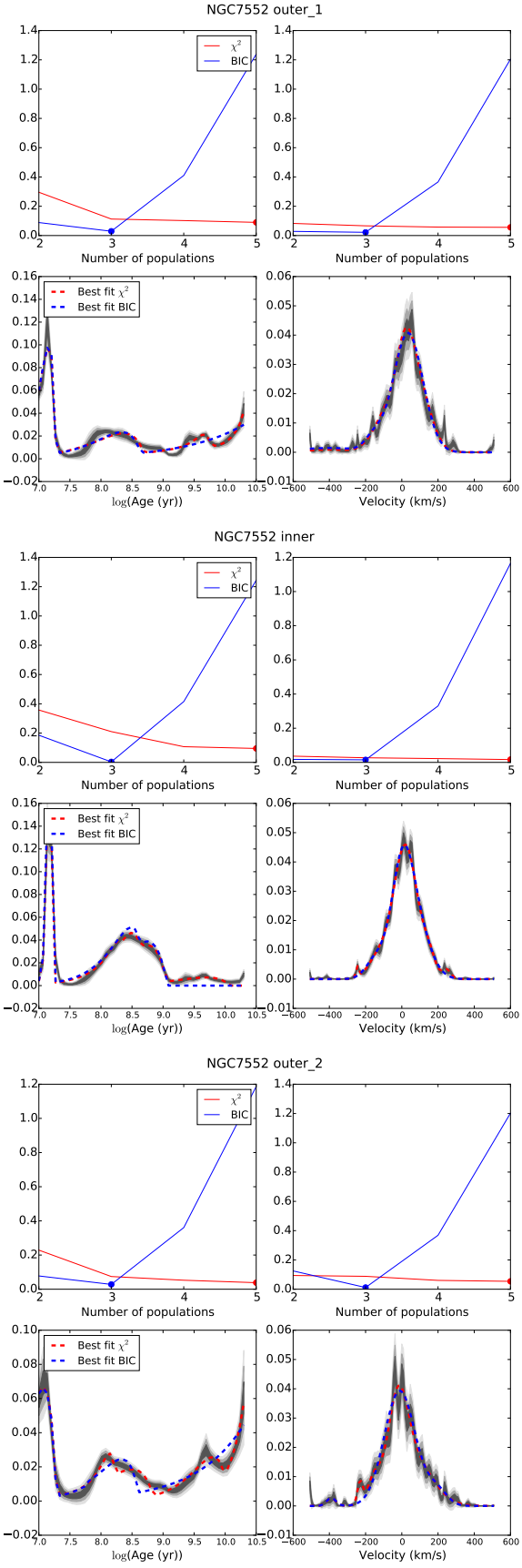

Figure 4.9: Estimation of the number of populations for the three regions in NGC7552.

properties in the two outer regions. Its radial velocity is around 200 km/s, and its velocity dispersion is very low, around 15 km/s. Its metallicity is subsolar (Z=0.01). The properties of this population are compatible with a disc or an inner spiral. The contribution of this population is very low ($\sim 3\,\%$ in light). As the disc in this galaxy is too faint to be detected (Gadotti and de Souza, 2003; Gadotti, 2008) and the inner spiral detected by Erwin and Sparke (2002) is big enough to contribute to these bins ($r \simeq 10''$), we conclude that this young contribution is the stellar component of the inner spiral.

We can compare our results obtained with the mean values of the parameters obtained without decomposing different stellar populations. We calculate the average properties of our results, and compare with the values calculated with the techniques described in Chapter 3. The mean ages and kinematics are in very good agreement. The metallicity is not in that good agreement. The different stellar population models used (with different ranges of age and metallicity) can explain these discrepancies. Here we use Pegase-HR, whilst in Chapter 3 we use MILES. Using MILES implies that the spectra have to be degraded to match the resolution of the stellar population models (2.51Å Falcón-Barroso et al., 2011). However, despite all these caveats and given the uncertainty in the derivation of the metallicities, the resultsare compatible with those obtained in the previous Chapter.

4.4.2. NGC6753

We decompose this galaxy in three different populations, shown in the AMK diagram in Fig 4.11

As in NGC5701, we find a double component (red and green symbols) in the bulge characterized by broad velocity distributions peaking near 0 km/s.These two populations have different properties, with one having larger velocity dispersion and metallicity than the other.

The star formation ring in this galaxy (see Crocker et al., 1996, and Chapter 3) is detected as a very young population (blue symbols), with a clear rotational kinematics (high rotational velocity and low velocity dispersion) and solar metallicity. The mean velocities, velocity dispersions mean ages and metallicities are compatible with those derived in Chapter 3.

4.4.3. NGC7552

Figure 4.12 shows the diagrams for the three regions of NGC7552. We find four different stellar components in the bulge of this galaxy.

The population of stars older than 10 Gyr, in this case, can be charac-

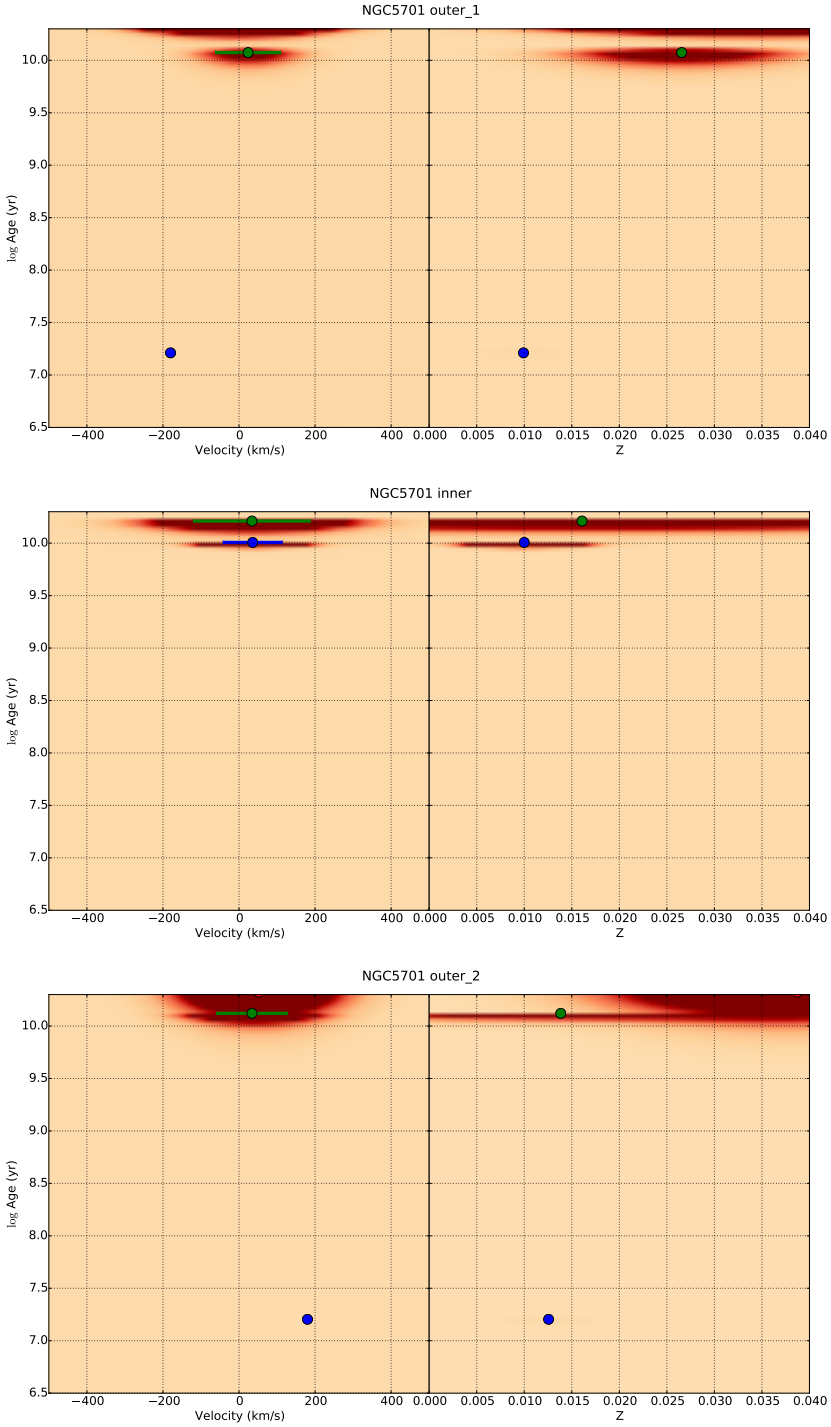

Figure 4.10: Age-metallicity-kinematics diagrams for NGC5701. These diagrams relate the age (vertical axis) with the velocity (horizontal axis in the left panels) and the metallicity (right panels). The diagrams for the three regions in the galaxy are represented from top to bottom. The dots represent the maximum of the contribution for each population in age, metallicity and velocity. The velocity dispersion of each population is represented by the errorbars. The horizontal projection of these panels is the SAD, the vertical projection of the left panel is the LOSVd of the synthetic spectrum. The AMR can be reconstructed from the right panel. The SAD, AMR and LOSVd of this synthetic spectrum are plotted in Fig. 4.1.

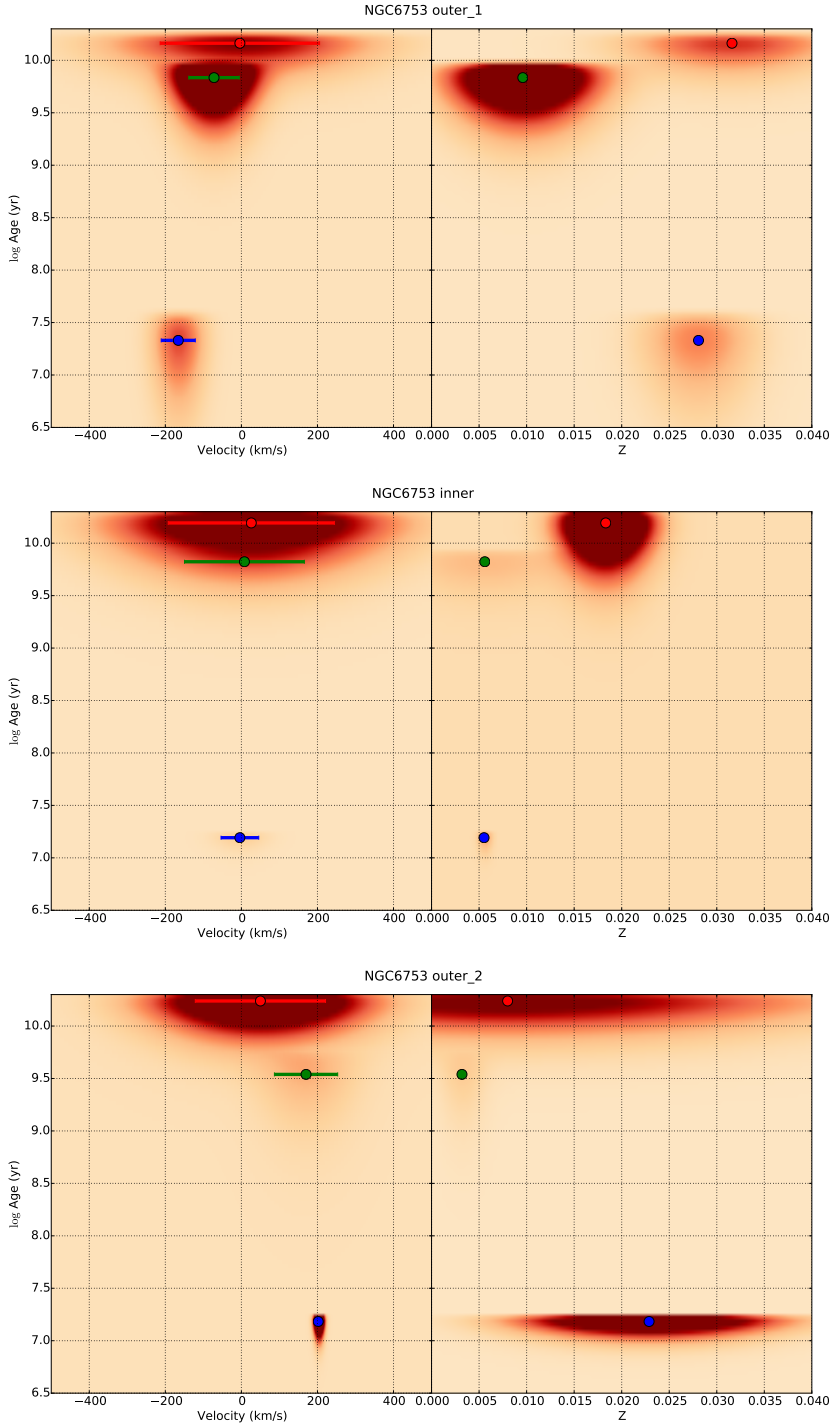

Figure 4.11: Age-metallicity-kinematics diagrams for NGC6753. Symbols represent the same as in Fig. 4.10

terized by just one component (black symbol) which, in this case, has lower metallicity in the outer regions (the opposite as happened in NGC5701 and NGC6753), showing super solar metallicity in the centre, and not showing in the outer regions.

The intermediate age component is characterized by one stellar populations. It does not show a clear rotation ($\leq$ 40 km/s), probably due to the inclination of the galaxy, which is almost face on. This population has roughly solar metallicity in the three regions.

Again, the star formation is revealed through the recently formed stars (black and blue symbols in the outer regions). In NGC7552 the young stars have very low metallicities, that can be explained by constant primordial (or, at least, very little evolved) gas flows.

The evolution of this galaxy is very different from the other two, having a larger contribution of young stars. The kinematics and the metallicity of the bulge are not very different to that of the disc, which makes it compatible with a pseudobulge.

4.5. Discussion and conclusions

We develop a new technique to disentangle the different stellar components that form the bulges of galaxies. We test this methodology with synthetic spectra, and establish its limitations and weak points, concluding that, in real galaxies, the conditions are good enough to properly disentangle the stellar populations.

We are able, for the first time, of recovering the whole set of parameters (velocity, velocity dispersion, age and metallicity) of each component in the bulge. We applied this technique to the three galaxies observed with WiFeS (see Section 3.2 for more information) that we already analysed in Chapter 3. Comparing the results obtained with the decomposition with those obtained by averaging the distributions given by `STECKMAP`, we see that both are compatible.

We find that NGC5701 has a bulge formed by a 99 % of stars with ages higher than 5 Gyr. Indicating that the bulge formed in early processes. However we find three different populations in our decomposition of kinematics and ages:

- a population with a luminosity weighted age of 20[4] Gyr, a null rotational velocity, a velocity dispersion of 125 km/s and contributing a

[4]This age is larger than the current estimate for the age of the Universe (13.7 Gyr), but the stellar evolution models need this age to fulfil the observations.

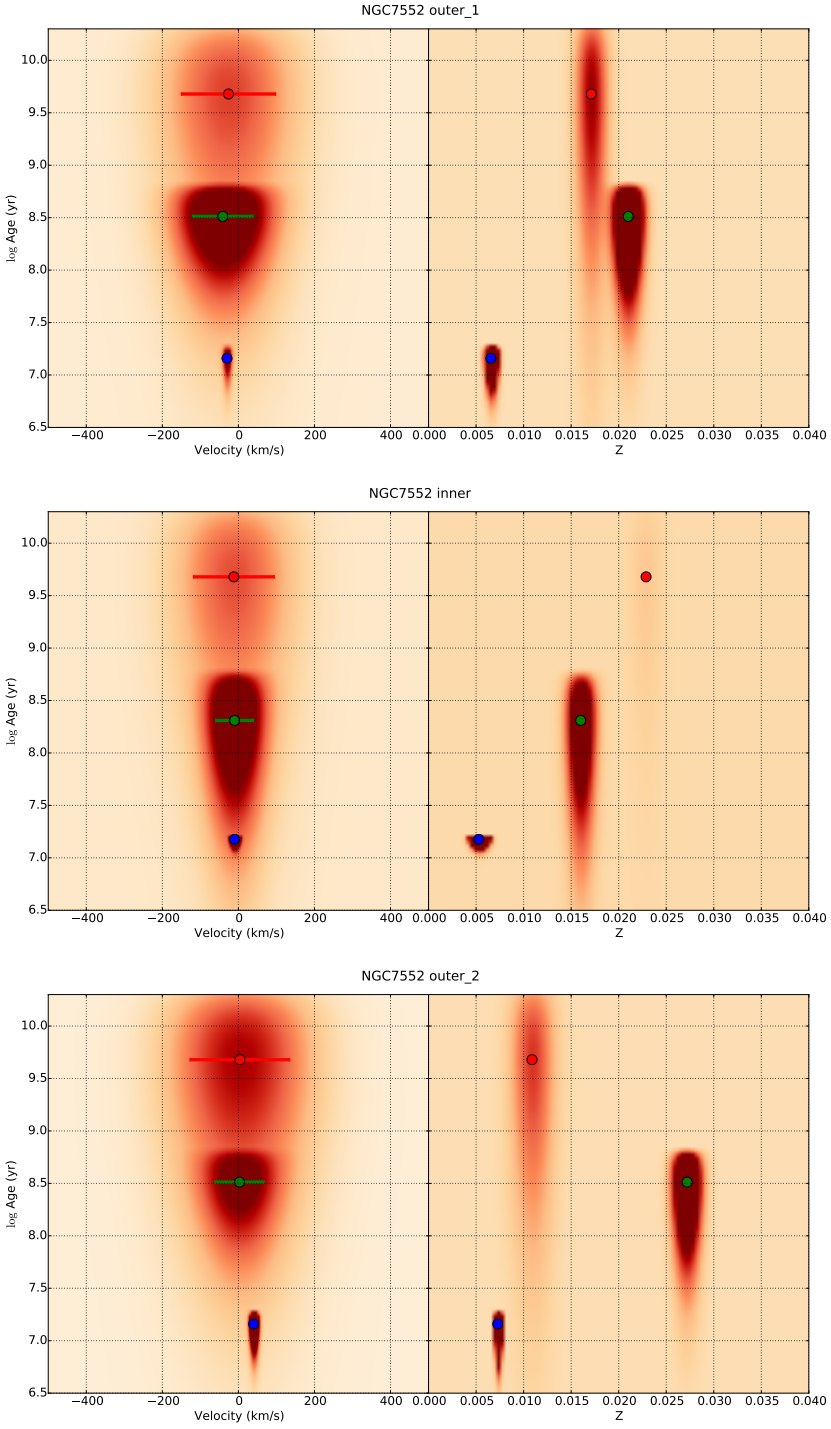

Figure 4.12: Age-metallicity-kinematics diagrams for NGC7552. Symbols represent the same as in Figs. 4.10 and 4.11

51 % in luminosity and .... % in mass. This population has a metallicity Z=0.016, compatible with its velocity dispersion (Thomas et al., 2005).

- a second population with a luminosity weighted age of 10 Gyr, rotating at 50 km/s and a velocity dispersion of 85 km/s. This population contributes a 46 % in luminosity and .... % in mass. The metallicity of this population is Z=0.01, which is also compatible with its velocity dispersion.

- a third population rotating with a velocity of 150 km/s and a very low velocity dispersion (15 km/s) and a metal content of 1 %. This galaxy contributes a 3 % (which is a negligible contribution in mass) and only in the two outer regions.

This young population is probably due to the nuclear spiral (Erwin and Sparke, 2002). This galaxy lacks of gas, except for this inner spiral, which discards gas inflows from the intergalactic medium in this galaxy. The other two populations are old and a kinematics not very different. However the results are consistent in the three regions (which are analysed in an independent way), which makes us more confident about them. These two populations could indicate that the bulge form in two different stages, as some simulations predict (*i.e.* Obreja et al., 2013). However, these simulations predict that the epoch of formation of bulges is between redshifts 1 and 3 (corresponding to ages of the Universe of 2 and 5), which is later than the epoch of formation of the stars in the bulge of this galaxy.

We find that the bulge in NGC6753 is formed also by a large fraction (60 % in luminosity) of stars with ages higher than 8 Gyr. We find the following populations in this galaxy:

- a population with 20 Gyr, supported by velocity dispersion (v_{rot}=4 km/s, σ=210 km/s), and supersolar metallicity (Z=0.032).

- a younger population, with a mean age of 3 Gyr, rotating at 75 km/s and with a velocity dispersion of 40 km/s. This population is less metal-rich than the previous one, with a metallicity of Z=0.0075.

- the third population is the youngest (20 Myr) in this galaxy. This population also is the one which is rotating faster (v_{rot}=200 km/s, σ=45 km/s) and roughly solar metallicity.

The two older populations show similar properties to that in NGC5701, also being compatible with the double-stage formation scenario for this bulge.

Again the ages of the stellar populations in the bulge is larger than those predicted by the galaxy formation models. The young population traces the star formation ring which is present in this galaxy. As can be seen in Fig.4.6 his ring is only covered by the bins of the two outer regions. However, the young population is also present in the inner region, which could indicates that stars are being transported to the inner region from the ring.

We find that NGC7552 is dominated by young stars. However, there is a large contribution of old stars (around 40 % in luminosity). We decompose this bulge in three different stellar populations:

- the oldest stellar population (16 Gyr) has a velocity dispersion of 124 km/s, with a very low rotational velocity (15 km/s). Its metallicity is roughly solar (Z=0.02).
- a stellar population with a mean age of 1 Gyr, with a rotation of 40 km/s and a velocity dispersion of 75 km/s. It also has a metal content compatible with solar metallicity.
- The fourth population is the youngest (2 Myr), and it is rotationally supported (v_{rot}=30 km/s, and σ=8km/s). The metallicity of this population is the lowest in this galaxy, with Z=0.006.

NGC7552 does not show a double component compatible with a classical bulge, suggesting a different evolutionary scenario than in NGC5701 and NGC6753. In mean, it is the youngest galaxy of the three, with less contribution of old stars than in the other two. The properties of the stellar populations in this galaxy (supported by rotation and with low velocity dispersion) makes it compatible with a discy pseudobulge.

Chapter 5

MILES stellar library extension

5.1. Introduction

A significant fraction of the observing time in large telescopes is dedicated to studies aiming at understanding the stellar content of galaxies at high and low redshift. In the last decade stellar populations studies provided among the most severe restrictions to our current view of how galaxies form and evolve (*e.g.* Kauffmann et al., 2003b). Such studies require to compare spectroscopic and photometric data with predictions of stellar population synthesis models, which are fed by either theoretical or empirical stellar spectral libraries. Most accurate studies requiring the analysis of line-strength indices have been made with the aid of models based on the Lick/IDS stellar library (Worthey et al., 1994). However the quality of the spectra of this library is not very good as the observations were performed at the end of the 70ś using a non-linear detector. The low resolution of this system (FWHM >8.4 Å) and its variation with wavelength, make the stellar population analysis difficult and uncertain (Worthey and Ottaviani, 1997).

Furthermore since the Lick spectra have not been flux-calibrated it is not possible to compute models predicting full SEDs. This limits the analysis to a number of indices, which prevents us to exploit the full potential of current observing facilities. In the last years we have published a new library, called MILES, observed at the INT with the IDS (Sánchez-Blázquez et al., 2006b). The library consists of 985 stars spanning an unprecedented range in atmospheric parameters (Cenarro et al., 2007). The spectra cover the full optical range at constant spectral resolution 2.5 Å FWHM.

MILES is regarded nowadays as the standard library in the field as its spectral resolution, spectral-type coverage, flux-calibration accuracy and number of stars represent a substantial improvement over previous libraries.

The MILES project was completed with a new generation of models that synthesize spectra of stellar populations based on this library. These models allowed us to safely extend our optical predictions from intermediate- to very-old-age regimes and the metallicity coverage from super-solar to [M/H]= −2.3.

Despite the good metallicity coverage of MILES, these stars are imprinted with the chemical composition of the solar neighbourhood, which results from the Star Formation History experienced in this region of the Galaxy. Following this pattern Oxygen (and Magnesium) is enhanced with respect to Iron for [Fe/H] <−1 decaying to reach zero at solar metallicity (*e.g.* Edvardsson et al., 1993a,b). Thus models based on MILES (as well as any other empirical library) are not fully appropriate for massive galaxies, which show [Mg/Fe] >0 and high metallicity, most likely, as a result of a rapid formation of the bulk of their stellar populations. A number of efforts have been made to build models with varying abundance ratios with the aid of theoretical atmospheres (*e.g.* Thomas et al., 2003; Coelho et al., 2007). Such models are however in their infancy and, more importantly, need to be calibrated.

As in MILES the metallicity is traced by the [Fe/H] abundance, *i.e.* ignoring the varying chemical abundance patterns present in individual stars, we have recently made an effort to determine the Mg/Fe abundance ratio of almost 80 % of the stars of MILES (Milone et al., 2011). For this purpose we have combined the abundance ratio determinations from high resolution spectra from the literature (*e.g.* Borkova and Marsakov, 2005) with our own determinations through a robust spectroscopic analysis using the MILES spectra, all carefully calibrated to a single uniform scale. In Fig. 2 we plot the abundance ratio of the MILES stars as a function of [Fe/H]. Note however that for a given [Fe/H] there is a significant scatter in the [Mg/Fe] values. We are in position to confirm that this scatter allows us to select appropriate subsamples of stars, mainly around solar metallicity, to construct reliable stellar population models with varying [Mg/Fe] ratios. A preliminary set of such models has been computed following this approach.

5.2. Sample Selection and Observations

The stars in each run are observed with the Intermediate Dispersion Spectrograph (IDS, with the EEV10 CCD) with three different instrumental setups :

- *Red* setup: using the R632V grating, which allows a 0.9Å per pixel and a spectral coverage of 5450-7500Å. The slit in this configuration covers

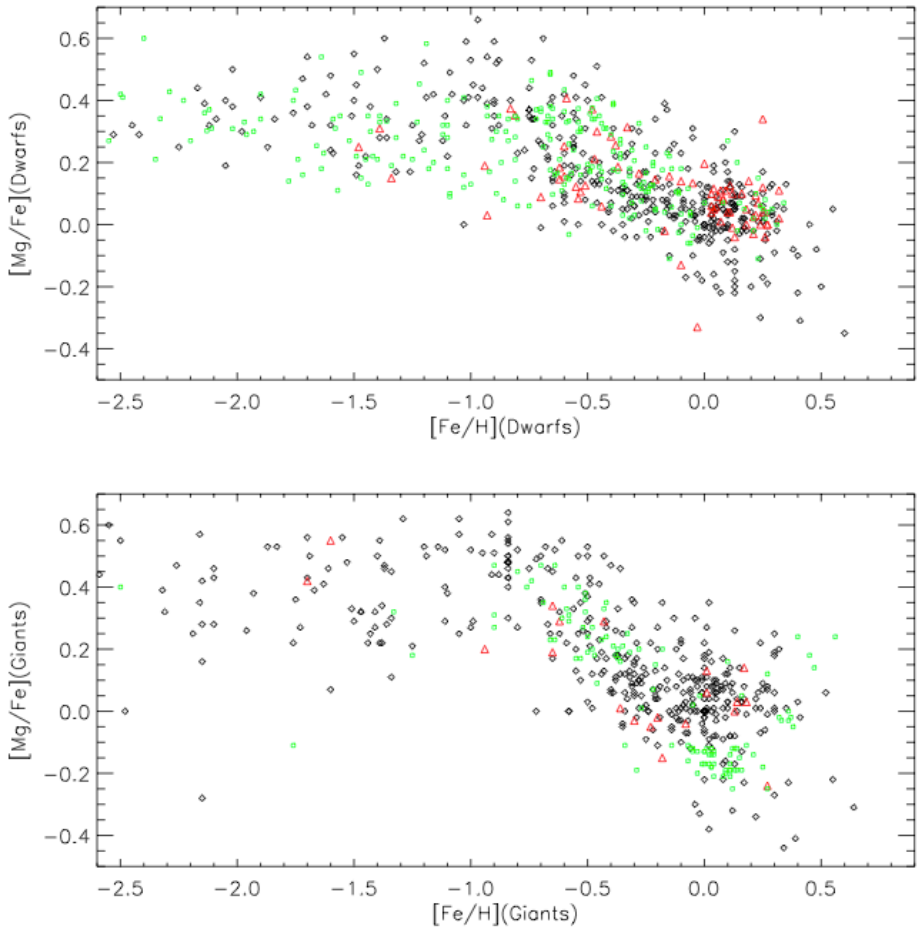

Figure 5.1: [Mg/Fe] against [Fe/H] for dwarfs (top panel) and giant stars(bottom panel) in the MILES library Black points represent the stars of the first MILES version while coloured points represent the new stars observed in this work. Green and red colours indicate stars observed in the first and second run, respectively.

0.7 arcsec on the sky.

- *Blue* setup: using the same R632V grating and slit width, but covering from 3500-5550Å. To minimize the second order contribution, a filter was set in the optical path.

- *Wide* setup: using the R300V grating (which allows us to cover the combined wavelength range of red and blue setup). This setup is designed to measure the flux of the star for calibration purposes so, in order to not to lose any light from the star, the slit projects 6 arcsec onto the sky. Also, a filter was introduces in the optical path to avoid second spectral order contamination. This filter was different in both runs, which will be discussed in Section 5.3.11.

5.3. Data Reduction

The data reduction process is similar to that in Sanchez-Blazquez (2004) and Sánchez-Blázquez et al. (2006b) for the MILES library. We use the package $\mathrm{R_ED^{uc}_mE}$ (Cardiel, 1999) in most of the steps, but we use Python[1] to do the renormalization of the spectra and the comparison of the new stars with similar stars in the library, which will be explained in Sec. 5.3.9. The main advantage of $\mathrm{R_ED^{uc}_mE}$ is that it allows a proper estimation of the uncertainties by pixel with a parallel processing of data and error frames. All spectra here, as happens with the original library, have an associated uncertainties spectrum.

5.3.1. Cosmic rays deletion

$\mathrm{R_ED^{uc}_mE}$ includes two different modules to clean the frames of cosmic rays, `autocos` and `cleanest`. The first one compares similar images to detect variations among them. Variations over a given σ (10σ in our case) are considered as cosmic rays. This method is useful when a large number of similar images is available, for example bias, flats and calibration frames in general. The second one compares the signal in one pixel with the surrounding pixels. If the value exceeds a number of times the standard deviation of the counts in the near pixels, it is considered as a cosmic ray. This second method is preferred for the object frames.

[1] http://www.python.org

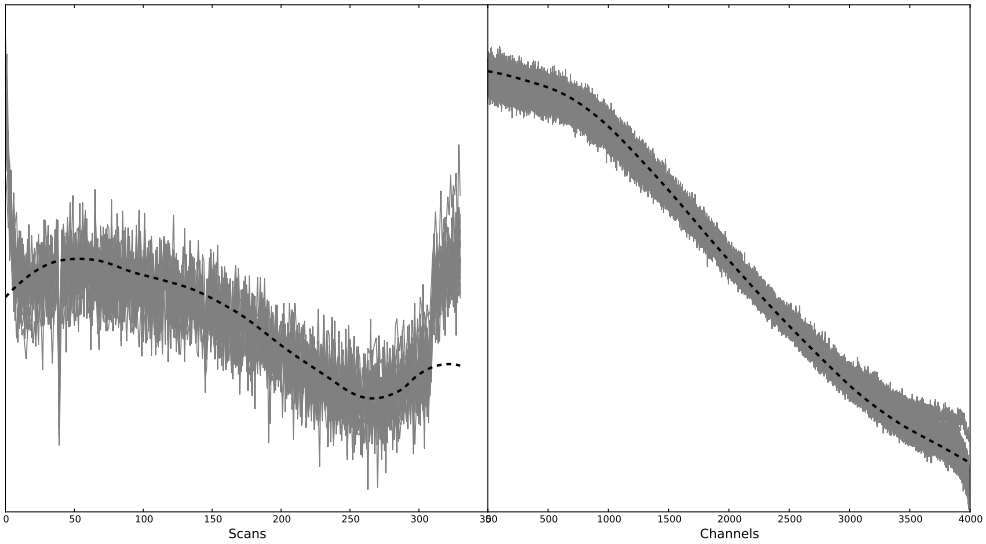

Figure 5.2: Comparison of a random sample of 20 bias frames (grey) with the master bias (dashed black line). We are comparing the average along the spectral (left panel) and spatial (right panel) directions. For the rest of nights, the shape of the bias frames varies, but the bias are stable each night.

5.3.2. Bias subtraction

We took at least 50 bias frames at the beginning and the end of each night. Comparing them we deduced that the bias signal is very stable during the night. Fig. 5.2 shows this stability for one of the night with a the *Blue* configuration.

For each night we calculated an average bias with all bias frames in each night. In the second run the readout of the CCD was configured with an overscan region which allows to calculate the bias constant. We fit a smooth surface to the average bias, obtaining the master bias. With the residuals to the master bias, we can calculate the readout noise. The constant and the master bias are subtracted from all frames in the corresponding night.

For the first run, no overscan region was configured, so the master bias frame includes both the bias constant and the shape of the bias.

5.3.3. Flat field correction

The flat field correction is done with two different types of frames: lamp flats, to remove high-frequency (pixel to pixel) differences in the detector sensitivity; and sky flats, to remove low frequency differences owing to the

different optical paths of the light from the lamps and the stars. In both cases, we remove the cosmic rays and the bias signal.

We first calculate an average frame using the lamp flats. This average frame is normalized by dividing it by its mean shape along the spatial direction. In the case of the sky flats, $\mathrm{R_E D_m^{uc} E}$ includes a routine (`nortwi`) devoted to the treatment of these observations[2].

Finally we end up with a master flat field and a master sky flat field.

5.3.4. Wavelength calibration

We took calibration frames (CuAr + CuNe lamps) at the beginning, the end and during every night with two different exposure times, in order to detect the faintest lines. The lines in the calibration frames are compared with the atlas of lines provided by the observatory to relate the position of the pixel with the wavelength using `findmax` and `findarc`. These data are fitted with `fitlin` to a 4-order polynomial. This is done for one reference arc frame of each instrumental setup (the lamps are stable during and along the nights, not in the intensity of the lines, but in their wavelength).

During the night we took arc frames after observing some of the stars; therefore, we have stars with an associated arc and stars without it. For the stars with an associated arc frame, we use the arc closest to the star and the reference arc frame.

For those stars without an associated arc frame, we calculate the offset respect to stars of similar spectral type and temperature which do have an associated arc frame. With this offsets we can calculate a polynomial for each star which relates the position of the pixel with its central wavelength. Using these polynomials we can calibrate the wavelength in each frame.

Stars are not still, but moving with respect to the observer. We looked for the velocity of each star in SIMBAD database and corrected for a little shift in the wavelength due to this radial velocity. In SIMBAD the radial velocity is expressed respect to the Sun, not respect to the Earth. Moreover, SIMBAD database is not homogeneus, with radial velocities taken from different sources and, therefore, with different accuracies. The correction from these combined effects is small, but noticeable, so we cross-correlate the spectra of the stars with a high resolution spectrum of the Sun (0.002 Å /pixel), taken from the database *BASS 2000*[3]. A comparison revealed that the wavelength calibration is, at least, as good as it is for the stars already in the library.

[2] `nortwi` first corrects from C-distortion, but, as discussed in Sec. 5.3.5, this is not necessary.

[3] http://bass2000.obspm.fr

5.3.5. Geometric corrections

There are two geometric distortions affecting the frames, called C and S distortions.

The C-distortion consists in a shift in the central wavelength of the pixels along the spatial direction of the detector. The effect on the spectrum is that, when collapsing the spectra along the spatial direction, the wavelengths of each scan do not match, and the measured properties of the star will be incorrect. Arc calibration frames are the best frames to detect and characterize this distortion. After a careful analysis of the emission lines in the arc frames, we concluded that no C-distortion was affecting our data, as the peak of each emission line along the spatial direction had the same pixel position (see Fig. 5.3). We do not have to correct from this effect.

The S-distortion consists in the spectrum being bent in the spectral direction. If S-distortion is present, more spectra have to be selected, and some of the pixels included will not have any information, so the signal-to-noise ratio will decrease. The best way to correct from S-distortion is to calculate the position of the peak along the spectral direction at each wavelength, and fit a polynomial to rectify the spectrum. This is done as an iterative process in order not to use very high order polynomials.

5.3.6. Atmospheric extinction correction and sky subtraction

We use the routine `correxT` for correct for the reddening effect of the atmospheric extinction. This routine uses an extinction curve provided by the observatory (La Palma, in this case).

We also subtract the sky brightness by fitting a polynomial to the pixels outside the spectrum of the star at each wavelength. This polynomials allow a proper subtraction of the sky while preserves the flux of the star and does not decrease the SNR. The task `skysubm` in R$_{\rm E}$D$^{\rm uc}_{\rm m}$E automatizes this process.

5.3.7. Flux calibration

All the former processes have been performed in parallel on the *Red*, *Blue* and *Wide* frames, adapting each point to the particular features of the frame. For every night we observed flux standard stars, because the MILES library is flux calibrated.

Due to the instrumental setup, the observed spectra may be affected by second order contamination (starting from 6700 Å). We use two standard

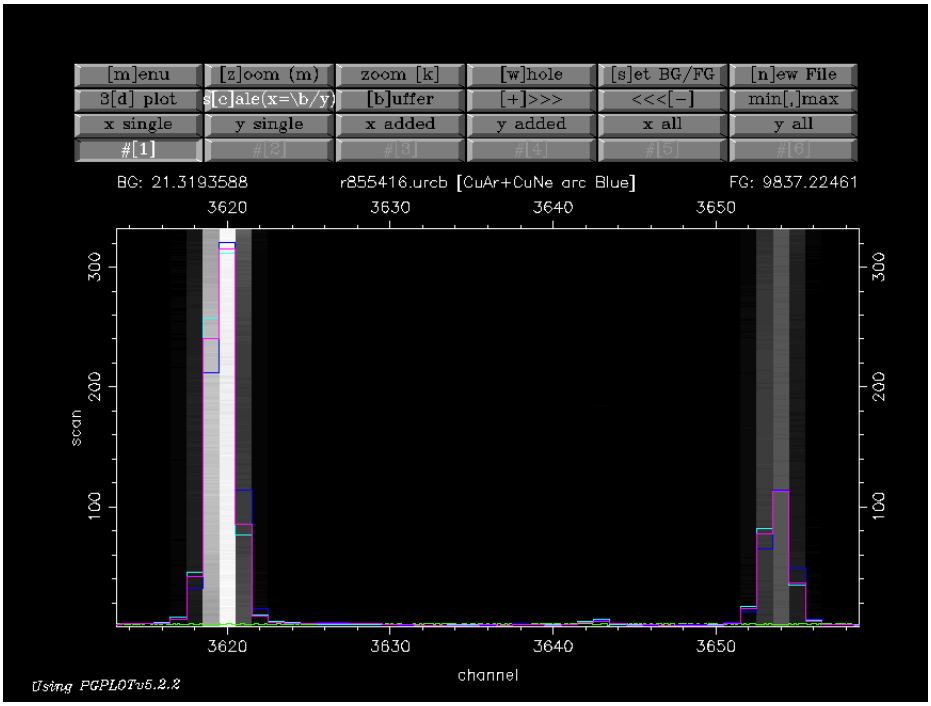

Figure 5.3: Emission lines from an arc frame. These lines are in the far end of the spectrum, where C-distortion is more noticeable. Blue, cyan and pink lines represent the profile of the lines at different scans. As can be seen, the maximum of the line is at the same channel for every scan, so we do not need to correct from C-distortion.

stars to correct for this effect.

Let S_a, S_b be the observed flux of two different standard stars, and T_a, T_b their tabulated flux. With the second spectral order contribution, these parameters are related as follows:

$$S_a = C_1 T_a + C_2 T_{2a}$$
$$S_b = C_1 T_b + C_2 T_{2b}$$

where C_1 and C_2 are the response curves for the first and second spectral orders, and T_{2a}, T_{2b} are T_a and T_b resampled to double the resolution and shifted 3350 Å to mimic the second order contribution. This system of equations can be solved to obtain the following expressions for the response curves:

$$C_1 = \frac{S_a - C_2 T_{2a}}{T_a} \text{ and } C_2 = \frac{T_a S_b - T_b S_a}{T_{2b} T_a - T_{2a} T_b}$$

The flux of a star from 3350 to 6700 Å is:

$$S'_c = \frac{S_c}{C_1}$$

which can be resampled and shifted to calculate its contribution to the second spectral order, S'_{2c}.

Finally, the calibrated flux of a star, S'_c is:

$$S'_c = \frac{S_c - C_2 S'_{2c}}{C_1}$$

This is the calibrated flux for the low resolution setup. To transfer this to the high resolution frames, we first lower the resolution of the *Blue* and *Red* frames to match he resolution of the *White* frames. The next step is to divide the *White* spectrum of each star by its corresponding *Blue* and *Red* spectra, so we obtain a calibration curve for each star observed in both configurations. The calibrated *Blue* and *Red* spectra result from multiplying the uncalibrated spectra by these calibration curves.

5.3.8. Combination of red and blue frames

Blue and *Red* frames overlap from 5450 to 5550 Å. We normalize both spectra attending to the flux in this region and combine them as an average, weighted by the inverse of the uncertainties in each pixel. Fig. 5.4 shows an example of the *Red* and *Blue* spectra after weighting and before adding them to obtain the full spectrum.

After this step we end up with a reduced spectrum of the stars, from 3350 to 7500 Å, with a dispersion of 0.9Å/pixel, and a FWHM of 2.51Å, as in the MILES library.

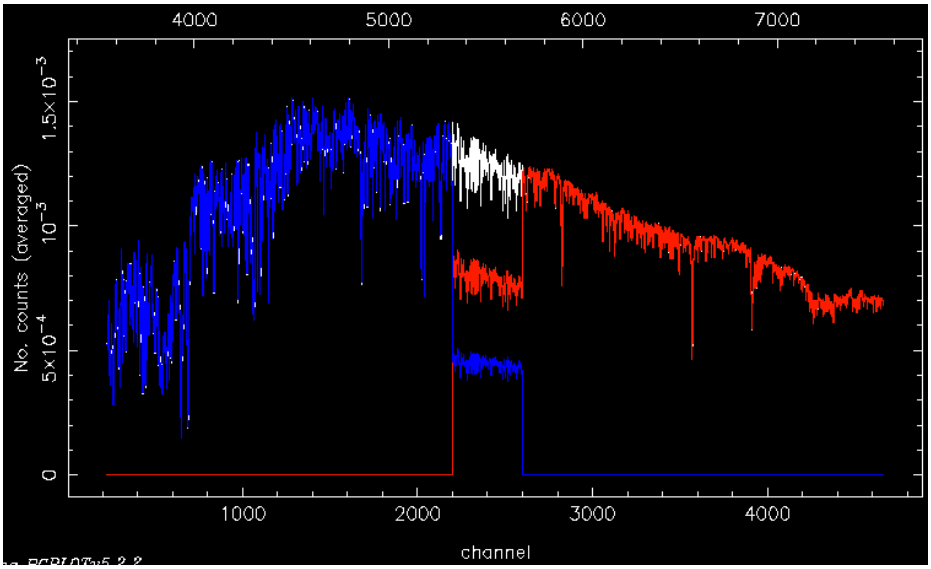

Figure 5.4: Addition of the *Red* and *Blue* frames for one star in the sample (Red and Blue lines) weighted by the inverse of their uncertainties at each wavelength. This addition results in the *Wide* spectrum (white line).

5.3.9. Quality check

The MILES library has been tested since the beginning. In Sanchez-Blazquez (2004); Sánchez-Blázquez et al. (2006b) a detailed explanation of the quality control can be found. Testing the new stars is necessary, but we make it in a different way, comparing the new stars with similar stars already in MILES, which have already been tested. As there are new stars in regions uncovered by the stars in MILES, this comparison is not possible for all the new stars. However, the number of stars with similar counterparts is high enough to discard systematic effects in the stars that cannot be compared. As future work, a better comparison (using colours and indices) will be performed.

Figure 5.5 shows a comparison between two stars, HD005494 (spectral type F8V, T_{eff}=6083K, log g=4.00, [Fe/H]=-0.15; in the sample of new observed stars) and HD035296 (F8V, T_{eff}=6091K, log g=4.25, [Fe/H]=0.04; in the MILES library) as an example. The shape of the spectrum is similar (taking into account that the stars are slightly different), and the central pixel of the lines are on the same position for both stars. This is true for all the stars in both observing runs.

5.3.10. Telluric lines removal

One of the problems of observing the red region of the spectrum is the presence of telluric lines. These lines are due to the absorption of the O_2 and H_2O molecules in the Earth atmosphere, and are usually removed by means of hot stars. We did not observe hot stars during the runs and, therefore, we use an alternative technique.

We use an algorithm that recovers the spectrum of a star with a given set of atmospheric parameters (T_{eff}, log g and [Fe/H]) using the rest of the stars in the library (see Appendix B in Vazdekis et al., 2003, for details). We can replace the region affected by telluric lines with the result of interpolating the stars in the library with the stellar parameters calculated for each star.

5.3.11. Blue region

As explained in Section 5.2, the filters used to remove the second order contribution are different in the two observing runs, GG385 in the first one and WG360 in the second one. As a result, the cut introduced to avoid the second order in the first run did not allow the light below 4000Å to pass (see Fig.5.6). This region is important to estimate the abundances of Ca, CN and other chemical species, and some indices also lie in this region. This issue

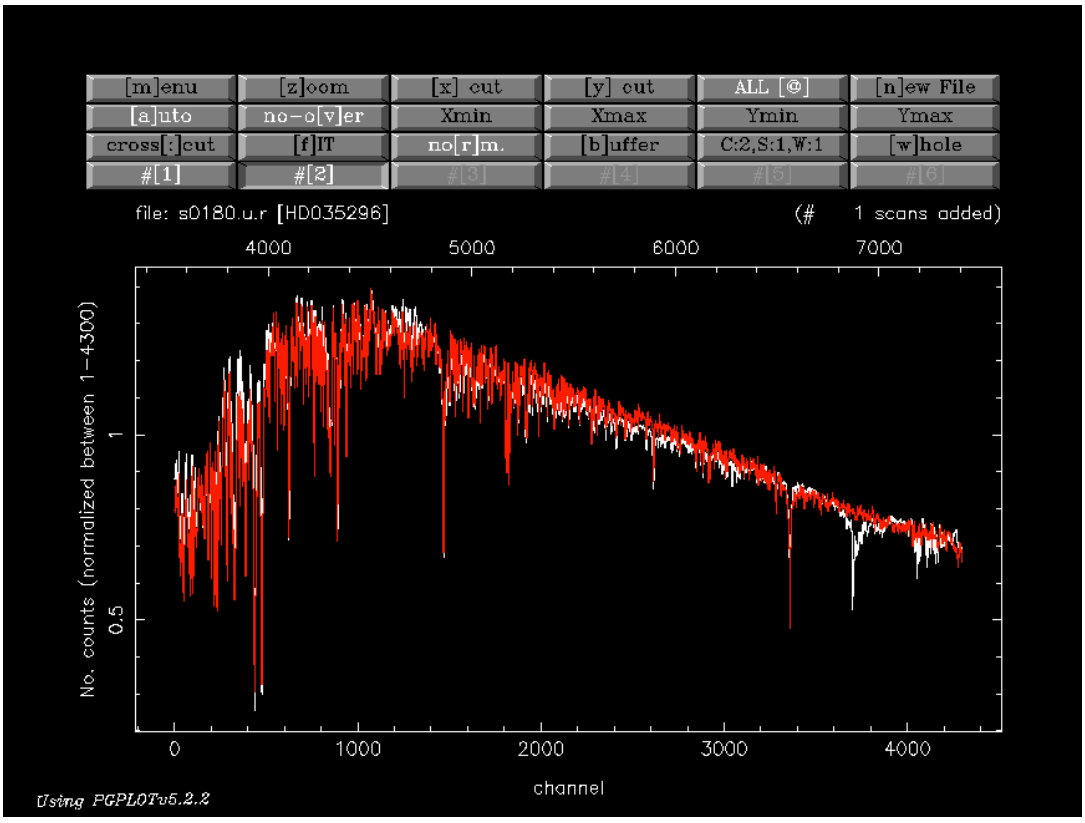

Figure 5.5: Comparison of two similar stars in the existing MILES library (red spectrum) and in the sample of new stars (white spectrum). As can be seen, the shape of the spectrum is similar, and the lines are in the same position, so the new stars are as good as the stars in the public library.

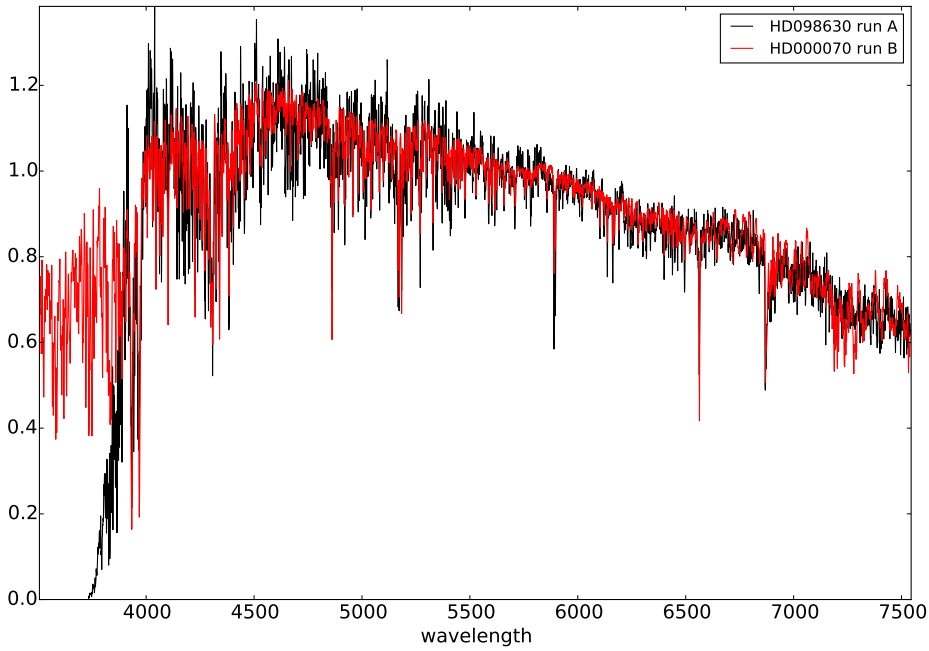

Figure 5.6: Comparison of the blue region for a star in the first (red spectrum) and second (black) observing runs. As can be seen, below 3800Å the flux of the spectrum in the run A is zero.

only affects to the frames with the *Wide* configuration, and only the flux calibration is compromised, as the spectral features are observed in the *Blue* configuration.

To solve this problem we will make use of the interpolator again. In this case, the interpolator will only be used to reconstruct the correct shape of the spectrum below 4000Å, using the rest of the spectrum as a constraint.

5.4. Conclusions

We have observed and reduced 250 new stars to be included in the MILES library. This means an increase of around 25 % over the whole MILES sample (985 stars).

A comparison of the new stars with MILES reveals that the quality of the new stars is, at least, as good as those in the original library, but the coverage of the [Mg/Fe]-[Fe/H] diagram improves significantly.

We face some problems during the reduction process, owing to different epochs of observations, different observers and the availability of the filters at each moment. However, these problems are successfully solved and the new stars can be included in the MILES library, after calculating their stellar parameters.

Chapter 6

Conclusions and future work

6.1. Conclusions

In this work we make a contribution to improve our knowledge about the bulges of disc galaies. We tackle the problem from different perspectives and using different datasets. The main results can be summarized as follows:

1. We constrain the role of the bars to the build up of bulges. We demonstrate that bars increase the flow of matter (gas and stars) to the central regions of galaxies, increasing the efficiency of the star formation processes, as indicated by the higher specific star formation rates and ionization parameters in barred galaxies.

2. This higher efficiency in barred galaxies is not enough to increase significantly the metallicity of the gas and the stars respect to that in unbarred galaxies.

3. We find differences in the ages of the stellar populations in the centres of galaxies. We do not find differences in the mean age at a given mass, but the mean age of stellar population in strongly[1] barred galaxies shows a bimodal (with peaks at ∼4.7 and ∼10 Gyr) distribution. The distributions of the unbarred subsample and the whole barred subsample do not show this bimodality (showing a peak at ∼10 Gyr)

4. As part of that analysis, we make a comparison between previous work and ours, and realize that there is much controversy on the results. A deeper comparison with the latest work before ours revealed a possible

[1] As defined by Nair and Abraham (2010), *i. e.*, in terms of the contribution of the bar to the total luminosity of the galaxy.

origin of the discrepancies in the analysis of the gaseous phase in the central regions of galaxies.

5. We analyse the subcomponents underlying galactic bulges, concluding that at least 50 % of the stellar mass in galaxies is formed 10 Gyr ago, although the sample is small. This result is in agreement with the results obtained by MacArthur et al. (2009) and Sánchez-Blázquez et al. (2011).

6. We develope a new technique to disentangle the stellar components of bulges. This technique allows us to relate the age, metallicity and kinematics of these populations individually, for the first time.

7. We used this technique in the bulges of three galaxies. We confirm the double stage formation of bulges predicted by simulations (Obreja et al., 2013), but only in two of the three galaxies in the sample. As these two galaxies are the earlier-type galaxies, the "double-bulge" formation may depend on the morphology.

8. We contribute to the extension of the MILES stellar library, increasing its size ∼25 %. These stars will be included in the library when their stellar parameters are obtained and will be used in a new version of the MILES stellar populations models.

6.2. Future Work

- Determination of the survivability of bars.

We said in Chapter 2 that knowing the timescale of bars is crucial to determine if their effect in galaxy evolution is as strong as predicted by simulations. Based on Gadotti and de Souza (2005), we want to estimate this timescale in a sample of face on galaxies from the CALIFA project (García-Benito et al., 2015; Sánchez et al., 2012; Walcher et al., 2014). We build two pseudoslits, along the bar and along its perpendicular direction. By comparing the vertical velocity dispersion in these two pseudoslits we can estimate the age of the bar.

- Population decomposition in the CALIFA sample.

We made some tests about the reliability of this technique in the galaxies observed in CALIFA. To perform this tests, we take the same synthetic spectra as in Chapter 4, but adapted to the resolution (R∼1700) and wavelength

range (3700-4200Å) of the high resolution data in CALIFA. Also, tests using the WiFeS data are carried to test for systematic effects arising from the construction of the synthetic models.

Figure 6.1 shows a representative example of these tests between the WiFeS data and the WiFeS data modified to fit the CALIFA specifications. We compare the LOSVd, SAD and AMR given by `STECKMAP` with the two configurations using KS tests. As can be seen in the figure, the LOSVd and SAD are compatible between both spectral setups, but not the AMR. This is true for seven of the nine spectra that we compare, so we can say that both kinematic and age decomposition are possible with CALIFA data.

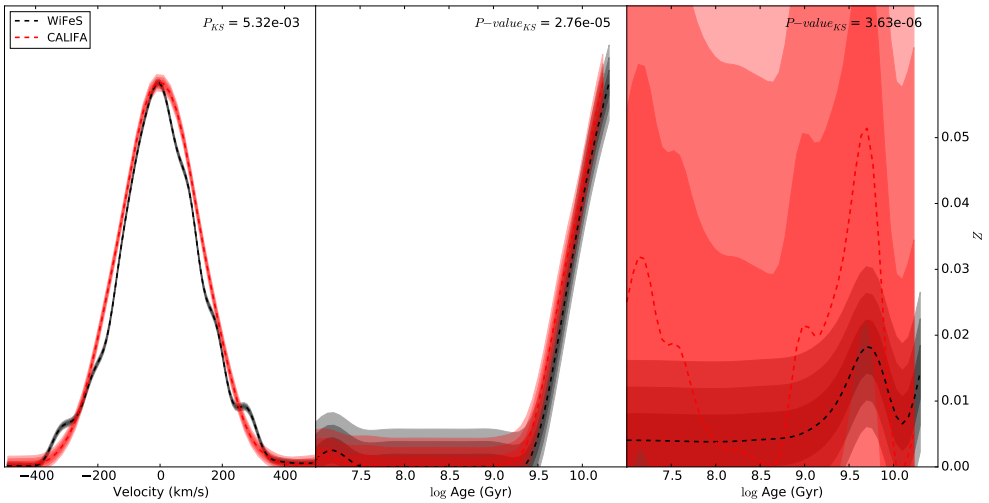

Figure 6.1: Comparison of the LOSVd (left panel), SAD (central panel) and AMR (righ panel) for the spectrum in the central region of NGC5701, as a representative example of the tests comparing the results obtained for the galaxies observed with WiFeS in its original version (black) and the results obtained with the spectra modified to match CALIFA spectral resolution and wavelength coverage (red). The mean distribution is represented by dashed lines, and 1 two and three sigma deviations are indicated by shadowed regions.

- Population decomposition with MUSE data.

MUSE (Multi Unit Spectroscopic Explorer Bacon et al., 2010) is a last generation integral field spectrograph in the VLT-UT3 unit in Paranal Observatory in Chile. In its wide field mode (1×1 arcmin) it combines a good

spatial (FWHM$\simeq$0.35 arcsec) and spectral (R$\simeq$2000 at 4650Å, R$\simeq$4000 at 9300Å) resolutions with a large wavelength range (4650 to 9300Å).

These features make MUSE the best instrument to apply our decomposition technique (described in Chapter 4). We will make some tests with real and synthetic spectra at the resolution and wavelength range of MUSE to study how efficient is our decomposition with this kind of spectra. The combination of the knowledge of the different stellar populations with their position in the galaxy will mean a big step forward in our understanding of how bulges form.

Appendix A

STECKMAP

A.1. Introduction

Full spectral fitting is a quite recent technique used to derive the properties of the stellar populations from an integrated spectrum. This technique consists in reconstructing the problem spectrum using a set of templates with known properties. There is a bunch of codes solving this problem from different approaches, like `STARLIGHT` (Cid Fernandes et al., 2005), `PPxF` or `STECKMAP` (Ocvirk et al., 2006a,b). The mathematics underlying these process is different in every code, but the basics are the same: to assign weights to stellar populations with a given age and metallicity. Most of the codes are also able to obtain the global kinematics of the stellar populations, by shifting and widening the template spectra.

Along this Thesis, `STECKMAP` has been widely used with most of the results coming from the use of `STECKMAP` in different ways. This full spectral fitting code is not very well known, and its use is not very straightforward. In these Appendix we show how we used `STECKMAP` and show the reader some hints and solutions to the issues we had with `STECKMAP`

A.2. Degeneracies

The calculation of the stellar population parameters is affected by several degeneracies. The most important (an known) degeneracy is the one existing between age and metallicity. This degeneracy has the effect that old metal-poor populations produce similar spectra than young metal-rich stellar populations. Full spectral fitting has proven to be very effective dealing with this degeneracy.

A less known degeneracy is that between metallicity and velocity dispersion. This happens because both metallicity and velocity dispersion increase the width of the absorption lines. This degeneracy is more evident when both parameters are calculated at the same time, but is easily removed when they are derived one at a time. We first calculate the velocity distribution and then we fix the kinematics to calculate the metallicity.

A.3. STECKMAP

One important difference among codes is how the solution is considered as a valid solution with physical sense. Usually the best solution is the linear combination of templates which minimize a given parameter (for instance, χ^2). However, due to degeneracies in the parameters, this criterion may not always be valid as there are many solutions which give similar good fits. Due to this, it is convenient to regularize the solution (Pichon et al., 2002). In the case of STECKMAP this regularization is done by means of Bayesian statistics and giving more probability to those solutions which change smoothly with age, penalising highly oscilating solutions. Another difference among codes are the assumptions that each one makes about the parameters. Most spectral fitting codes assume Gaussian velocity distributions. STECKMAP only imposes positivity, continuity and smoothness of the solution.

The following code is an example of how we use STECKMAP:

```
dlambda=1.7; // sampling of the basis.
kin=1; // kin=0 -> no kinematics, kin=1 -> LOSVD search
epar=3; // with continuum matching (to deal with flux calibration errors)
nde=30; // number of control points for continuum matching
vlim=[-1000.,1000.]; // wavelength domain for the LOSVD
meval=500; // maximum number of evalutations during the optimisation

muv=0.1; // smoothing parameter for the LOSVD
mux=10; // smoothing parameter for the stellar age distribution
muz=100; // smoothing parameter for the age-Z relation

L1="D2"; // smoothing kernel for stellar age distribution (here D2, i.e. square Laplacian)
L3="D1"; // smoothing kernel for age-metallicity relation (here D1, i.e. square gradient)
L2="D1"; // smoothing kernel for the losvd (here D1, i.e. square gradient)
//L4="D2"; // smoothing kernel for the non parametric flux recalibration (here D1, i.e. square gradient)

// File to fit
fV="example.fits";

// Generating basis of models
b=bRbasis3(ages,wavel=wavel, basisfile=basisfile,nbins=nbins,dlambda=dlambda); // generate basis
ws;plb,b.flux,b.wave;   // plots the basis

// Parameters
z0=0.00475;
nMC=50
```

```
SNR0=8.58068647458;
RMASK=[[3000, 3300], [3702.,3735.],[3886.,3890.],[3967.,3973.],[4098.,4105.],[4336.,4346.],[4830.,4845],[4855.,4870.],[49

// Converting to STECKMAP format
a=convert_all(fV,log=0, SNR0=SNR0, z0=z0);

// Fitting
x=sfit(a,b,kin=kin,epar=epar,noskip=1,vlim=vlim,meval=meval,nde=nde,RMASK=RMASK,\\
          mux=mux,muv=muv,muz=muz,L2=L2,L4=L4,L3=L3,L1=L1,sav=1, nMC=nMC,\\
          dMC="data",fg="flat",MC_noise="yes");
```

In these lines of codes, some parameters can be modified to adapt the code to our data. The most important are the following:

- *basisfile*: indicates which stellar population models are being used to fit the input spectrum. STECKMAP allows natively to choose among MILES, Pegase-HR or Bruzual and Charlot (2003).

- *wavel*: marks the wavelength range to perform the spectral fitting.

- *ages*: limits the age range of the stellar populations. This range should be smaller or equal to the range covered by the stellar population models.

- *kin*: enables or disables the calculation of the kinematics. The possible values of this tag are: 0, in which the kinematics can be fixed (by including the mean radial velocity in the redshift and widening the basis spectra using the tag *FWHMpix*); 1, in which the velocity distribution is calculated within the limits set by *vlim*; or 2, in which a decomposition of stellar populations is performed (see the pilot study on NGC4030 by Ocvirk et al., 2008).

- *epar*: enables the extinction correction. It can be disabled (*epar*=0), or different models for the extinction correction can be used. The default value, *epar*=3, considers a non-parametric extinction curve which also corrects for incorrect flux calibrations.

- *muv, mux, muz, mue*: are smoothing parameters for the velocity distribution, age distribution, metallicity distribution and extinction curve, respectively. STECKMAP regularizes the solution imposing positivity and smoothness. STECKMAP tries to minimize the objective function $Q_\mu(x) = \chi^2(x) + \mu P(x)$, which penalizes χ^2, for each distribution. The penalization can be modified with muv, mux, mux and mue (corresponding to the μ in the former equation).

- *L1, L2, L3, L4*: are the smoothing kernels, which correspond to the $P(x)$ in the equation in the previous item. $P(x)$ means $x^T \cdot L^T \cdot L \cdot x$, where L can be a first (gradient), second (Laplacian) or third order operator. The operator is chosen by setting *L1, L2, L3* and *L4* to D1 (gradient), D2 (Laplacian, which is the default) or D3 (third order operator).

- *SNR_0*: represents the signal-to-noise ratio of the input spectrum. If a noise spectrum is available, it can be supplied with *errorfile=* instead than the SNR. This is a critical parameter, as an incorrect determination of the SNR leads to wrong age (and therefore, metallicity) distributions. We find that the best results are obtained with the `der_SNR` algorithm.

- *nMC*: indicates the number of Montecarlo simulations performed with every spectrum. In each MC experiment, the mock spectrum can be build using the data (with the tag *dMC*="data") or with the first best fit to the problem spectrum (*dMC*="bestmodel"). Also noise can be added or not using *MC_noise*="yes" or *MC_noise*="no".

A.4. Outputs

A.4.1. Quality of the fit

During the execution, `STECKMAP` prints some messages on the console. When the fit has finished, the following information appears on the screen.

The most relevant parameters here is the final value of *FUNC*. It represents the optimization parameter and behaves similarly to a reduced χ^2, this is, the fit is better when this parameter is close to 1. This parameter does not guarantee that the fit is good, but a good fit always has $FUNC \simeq 1$.

A.4.2. Velocity distribution

The line-of-sight velocity distribution (LOSVd) is, in fact, a broadening function including kinematics and instrumental effects. The instrumental effects can be avoided if the stellar population models are broadened with the PSF of the instrument.

This distribution is non-parametric and represents the fraction of stars (normalized to unity) with a given rotational velocity.

A.4.3. Stellar age distribution

The stellar age distribution (SAD) represents the contribution in flux to the total spectrum by the stars at a given age, normalized to sum 1. Again, this distribution is not parametric. The SAD is the basic distribution `STECKMAP` works with.

A.4.4. Age-Metallicity relation

The AMR gives the mean metallicity of the stars at a given age. The metallicity is expressed as Z, *i. e.* the fraction of elements heavier than He. The models included in `STECKMAP` are calibrated to have $Z_{\odot}$ =0.02.

A.4.5. Mass

In this file we can find the mass of the stars at a given age. This mass has to be interpreted as the mass that the stars at this age had at the beginning, without taking into account any loss of mass. The mass distribution can be related with the SAD with the following equation:

$$M_i = \frac{SAD_i}{M/L_i},$$

where M_i is the mass of the stellar population with age i, SAD_i is the fraction of flux in the spectrum due to these stars and M/L_i is the mass-to-luminosity ratio of the stellar population i. With this equation we can transform luminosity-weighted values into mass-weighted values.

In principle the mass distribution is given in solar masses, taking into account that the SAD is normalized to unity. More correct would be to say that the units are $M_{\odot}/L_{\odot}$. In any case, the relative masses are correct.

A.4.6. Star Formation Rate

The SFR is obtained by dividing the mass in the interval i by the length of the time interval. It is normalized arbitrarily, as it depends on the normalization of the mass. As in the mass distribution, the relative values of SFR between time intervals is correct, but not the absolute values. In fact, the profile given by the SFR can be considered as a sort of SFH.

A.4.7. MC simulations

As mentioned in Section A.3, `STECKMAP` is designed to perform MC simulations, each of them resulting in a different LOSVd, SAD, AMR, Mass

distribution and SFH. This is very useful to estimate the uncertainties of the parameters.

A.5. Calculating stellar parameters

A.5.1. Kinematics

The kinematics of the stellar populations are usually given assuming that it follows a Gaussian distribution. In the case of STECKMAP, the distribution is not even parametric, so a Gaussian (or a more complex Gauss-Hermite) curve may not describe it properly. We decided to calculate the mean rotational velocity and velocity dispersion as the weighted average and the weighted standard deviation of the distribution, this is:

$$\bar{v} = \frac{\Sigma_{i=1}^{N} w_i v_i}{\Sigma_{i=1}^{N} w_i}; \; \sigma = \sqrt{\frac{\Sigma_{i=1}^{N} w_i (v_i - \bar{v})^2}{\frac{M-1}{M} \Sigma_{i=1}^{N} w_i}},$$

where N is the number of points in the distribution, M is the number of nonzero weights, w_i are the weights, v_i is the velocity and $\bar{v}$ is the mean velocity. The mean velocity and the velocity dispersion are more correct calculated in this way than simpli fitting a Gaussian or a Gaus-Hermite curve to the LOSVd.

A.5.2. Age

The mean age of the stellar populations contributing to the spectrum can be obtained as the weighted average of the SAD, with the following equation:

$$\bar{Age} = \frac{\Sigma_{i=1}^{N} w_i Age_i}{\Sigma_{i=1}^{N} w_i},$$

which is the same as the equation in the previous section but changing the velocity by the age. It has to be taken into account that the age is expressed in a logarithmic way so, to avoid mistakes, we first convert it to a linear scale, calculate the weighted average of the distribution and finally calculate its decimal logarithm.

A.5.3. Metallicity

We do not have a distribution of the metallicity, but the metallicity of the stars at a given age.that age. From the SAD we have the fraction of stars at that age. We can calculate the mean metallicity as the average of the AMR weighted by the SAD:

$$\bar{Z} = \frac{\Sigma_{i=1}^{N} w(Age_i) Z(Age_i)}{\Sigma_{i=1}^{N} w(Age_i)},$$

A.5.4. Mass weighted parameters

We calculate luminosity-weighted values with the previous equations, which trace young stars. However, we may be interested in the old stars populations, which are better traced by the mass. So, we have to derive mass-weighted values. `STECKMAP` returns the mass of the stars at a given age. In all previous equations, replacing the weights by the mass allows to calculate mass-weighted values.

A.5.5. Uncertainties

We run, at least, 30 MC simulations in every run of `STECKMAP`. With each run we have a different distribution of each parameter. With this simulations we can calculate the dispersion of the values for each point in the distribution aound the value obtained in the first run (with the original spectrum). With this dispersion we can generate an infinite number of distributions which we can use to derive the uncertainties.

Appendix B

Comparison between spectral synthesis and Lick/IDS indices

Abstract:

Along this thesis we used in many ocasions the spectral synthesis to infer results about the properties of the stellar populations, and as a way to remove the stellar continuum for a correct measurment of the flux in the emission lines. This technique is in use for a relatively short time, and some scepticism still exists about its performance. In this appendix we compare the results obtained using spectral synthesis with those obtained using a more accepted technique like Lick/IDS indices. The conclusions are that spectral synthesis surpasses indices, as it allows to obtain more parameters simultaneously, and allows a more precise information about the stellar populations, not only average values.

B.1. Introduction

In this thesis we based much of our work on the full spectral fitting technique, in particular, with `STECKMAP` (Ocvirk et al., 2006a,b), which is a software which recovers a spectrum from a library of stellar populations models (in our case, Sánchez-Blázquez et al., 2006b; Vazdekis et al., 2010, with a Kroupa universal initial mass function, Kroupa 2001). This code allows us to calculate the properties of the stellar populations underlying the observed spectrum. To not to leave this comparison in hands of only one spectral synthesis code, we also calculate the parameters using `STARLIGHT` (Cid Fernandes et al., 2005), which also fits the spectrum but in a different way as `STECKMAP` does.

A very often used technique is Lick/IDS indices (Worthey et al., 1994). An index consists in three bands on the spectrum, of which two of them are used to estimate the flux of the stellar continuum and the one in the middle is used to estimate the absorption of the spectral features. After the indices are measured, index-index diagrams can be build in which, ideally, one of the indices is only sensitive to the stellar age and the other is sensitive only to the metallicity. In practice, indices are dependent of both age and metallicity (and some of them are sensitive to abundances of individual elements). Using models a grid can be built and, with the position of the galaxy in the grid, the age and metallicity can be estimated by interpolation of the grid. This technique also requires the use of stellar population libraries. In this work we use the diagram Hβ-Mgb and MILES stellar population library (Sánchez-Blázquez et al., 2006b; Vazdekis et al., 2010).

None of the techniques are exempt of issues, not owing to the technique itself, but to the lack of knowledge about several parameters related to stellar populations, like the initial mass function (IMF), star formation models, chemical evolution models, etc. Moreover, degeneracies exist between age and metallicity, or velocity dispersion and metallicity, for instance. We make the comparison between spectral synthesis and indices with the sample of galaxies used in Chapter 2.

B.2. STARLIGHT vs. STECKMAP

We compare here the results obtained by the two codes searching for differences between them, in order to have a higher capacity of decision in choosing one or another and to be able to enable comparisons with other authors.

Figure B.1 compares the mean ages and metallicities (weighted with both, mass and luminosity) obtained with `STARLIGHT` and `STECKMAP`. It can be seen that the values obtained for the ages with both codes are well correlated. However, the correlation is far from the equivalence. This has the consequence that, even when absolute values ages cannot be considered reliable, relative comparisons can be done. However, in the case of luminosity-weighted metallicities, the correlation is high (with a large scatter, but within uncertainties), and very close to equivalence between codes. In the case of mass-weighted values, the discrepancies are not negligible. `STARLIGHT` tends to return higher metallicites, saturating at [Z/H]$\sim$0.02. This effect is coupled to the lower ages returned by `STARLIGHT`

Because of the saturation in the metallicities of `STARLIGHT` and that it tends to return too low ages, we will use `STECKMAP` as spectral fitting software.

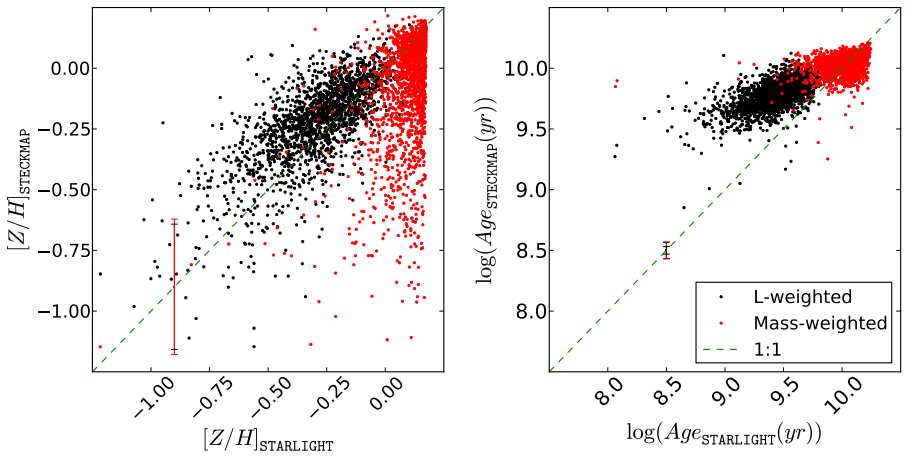

Figure B.1: Comparison of the values returned by STARLIGHT (horizontal axis) and STECKMAP (vertical axis). Red points show mas weighted values, while luminosity weighted values are plotted in black.

B.3. Spectral synthesis vs. Lick/IDS Indices

Finally we compare the results obtained using spectral synthesis with the results given by Indices. It has to be taken into account that the results represent different parameters: with indices, we calculate single-stellar population equivalent parameters, which are not exactly the same as the luminosity-weighted values obtained with spectral fitting (Serra and Trager, 2007); spectral synthesis calculates the mean age and metallicity of the stellar populations contributing to the observed galaxy spectrum.

The comparison between these methods is shown in Fig. B.2. Right panel shows that, for the metallicities, the correlation between spectral synthesis and indices is high, being almost equivalent, and independent of the synthesis code used. For the ages the correlation is worse, but it exists (attending to the Spearman correlation coefficients, shown in Table B.1), so we can establish the following relation between ages and metallicities obtained in different ways:

$$Age_{\mathrm{STARLIGHT}} = 2.90 \times Age_{indices} - 1.7e9$$
$$Age_{\mathrm{STECKMAP}} = 2.87 \times Age_{indices} + 1.7e9$$
$$[Z/H]_{\mathrm{STARLIGHT}} =$$
$$0.031 \times [Z/H]^3_{indices} + 0.24 \times [Z/H]^2_{indices} + 0.63 \times [Z/H]_{indices} - 0.17$$
$$[Z/H]_{\mathrm{STECKMAP}} =$$
$$0.017 \times [Z/H]^3_{indices} + 0.14 \times [Z/H]^2_{indices} + 0.44 \times [Z/H]_{indices} - 0.13$$

	Indices	STARLIGHT	STECKMAP
Indices	—	0.66 (10^{-147})	0.45 (10^{-57})
STARLIGHT	0.66 (10^{-147})	—	0.54 (10^{-90})
STECKMAP	0.45 (10^{-57})	0.54 (10^{-90})	—

Table B.1: Spearman correlation coefficients for the ages appearing in this paper. The closer the coefficient is to 1, the stronger the correlation is. Below each value, in brackets the P-alue can be found, which is the probability of finding the Spearman coefficient if the subsamples are not correlated.

B.4. Conclusions

In this Appendix we prove thar spectral synthesis is a very useful tool for the analysis of non resolved stellar populations in galaxies. Not only the results are compatible with those obtained using Lick/IDS indices, but also give more and better information (like kinematics), as it deals better with degeneracies in the determination of metallicities and ages.

We also confirm that, considering spectral synthesis, luminosity-weighted values are more robust than mass weighted values, as their dependence on the code is much smaller in the former than in the latter. This happens because low mass stars do not contribute much to the spectrum, and a large variation in their properties barely modifies the spectrum. Unless the opposite is said, we use luminosity weighted values.

Thanks to the spectral synthesis through STECKMAP we have been able to develop a technique (described in Chapter 3 which allows us to decouple the underlying stellar populations in galaxies obtaining, simultaneously, the kinematics, ages and metallicities of each of them with high precision.

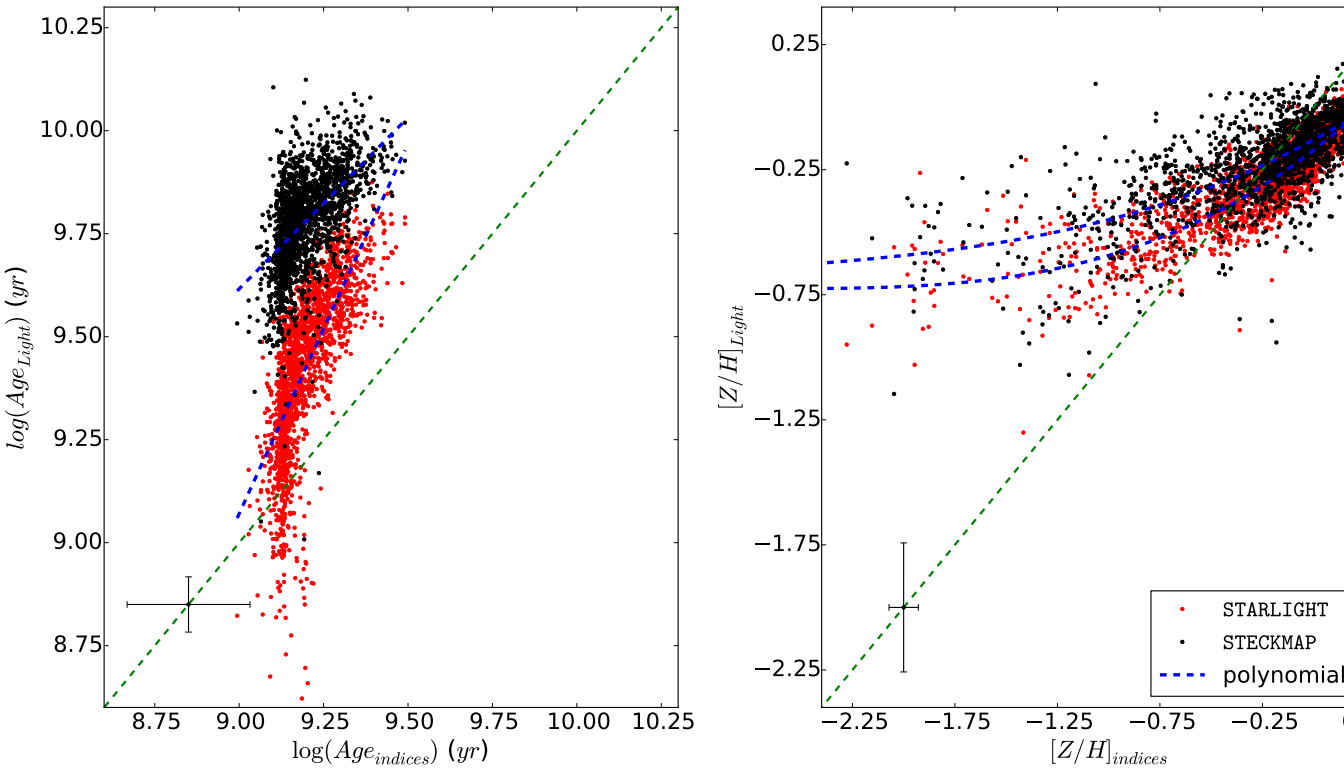

Figure B.2: Comparison of the ages (left panel) and metallicities (right panel) obtained by means of indices and full spectral fitting with both `STARLIGHT` (red points) and `STECKMAP` (black points). The green dashed lines represents the equivalence between indices and full spectral fitting, while the blue dashed lines represent the fit (linear for the ages, and a third order polynomial for the metallicities) The errorbars indicate the typical uncertainty of the derived ages and metallicities.

Appendix C

Robustness of results with redshift and inclination

Abstract:

In Chapter 2 we use redshift and inclination of galaxies as sample selection criteria, but they are not physical parameters, but they are determined by the position of the observer. This parameter, while have no effect on the evolution of galaxies, may alter the results. In this appendix we check that results do not depend on these parameters.

C.1. Redshift effects

When comparing the age of the two samples, as we did in Chapter 2, it is importatn that the redshift range distribution is similar. In our case the redshift range is not very large ($0.02 \leq z \leq 0.1$), however, we have considered cautious and convenient to check if results are independent of redshift. To do so, we separate the galaxies in the sample in redshift intervals and compare the metallicities of barred and unbarred galaxies in each one of those intervals.

Figure C.1 shows the mass-metallicity relations (separately for barred and unbarred galaxies) in each redshift interval, comapring them with the relations for the whole subsample. The first thing to be noticed is that mass grows with redshift. This happens because less massive galaxies are also less luminous, so they are more difficult to be detected at higher redshifts. We calculate the residuals of galaxies in each interval respect to a third order polynomial fit to the whole subsample of barred or unbarred galaxies (as appropriate) and compare them with the residuals of the subsample to the

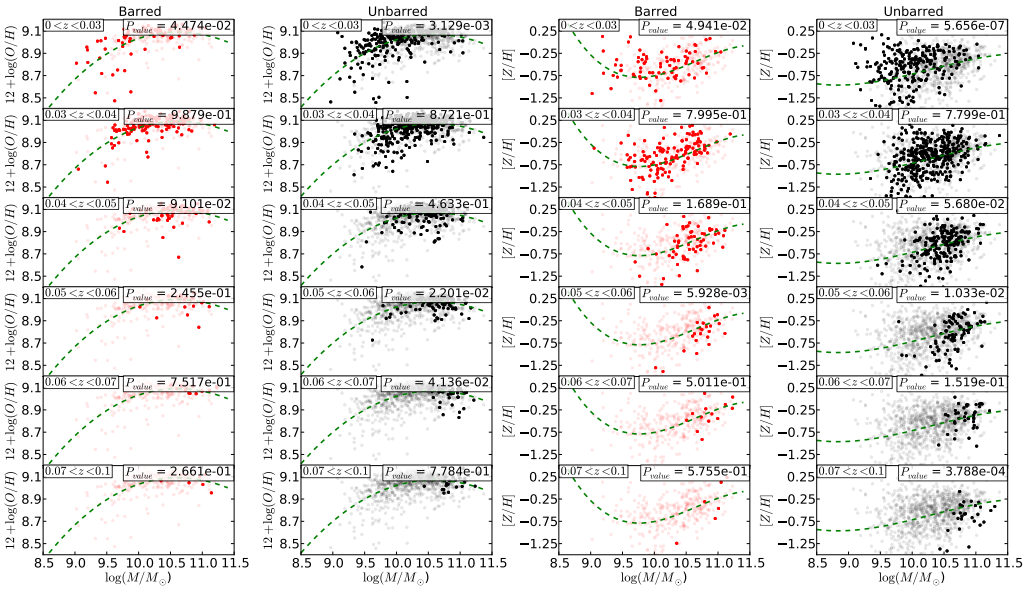

Figure C.1: Mass-metallicity relatiosn for barred (red) and unbarred (black) galaxies in different redshift intervals (shown in top left corner of each panel). Green dashed lines represent a polynomial fit to the barred or unbarred subsample (light points). On the top right corner, the P-value of the KS test comparing the residuals of the subsamples in the redshift interval is shown. The two columns on the left refer to gas-phase metallicity, while the two columns on the right refer to te stellar metallicity.

same fit using a KS test (3σ, P-value=0.0027). The distribution residuals have the same behaviour than the corresponding subsample in every case.

We just showed that the metallicity of galaxies has the same behaviour, however, this does not mean that the differences between them behave the same at different redshifts. To check this, we repeat the same analysis than that in Section 2.5.1 for each redshift interval, *i.e.* we compare the residuals of barred and unbarred galaxies from a polynomial fit to unbarred galaxies using a KS test. Fig. C.2 shows these differences along the P-values for the KS tests. In every case, the probability that the results owe to random effects is lower than the significance level, so we can conclude that our results are robust in terms of redshift.

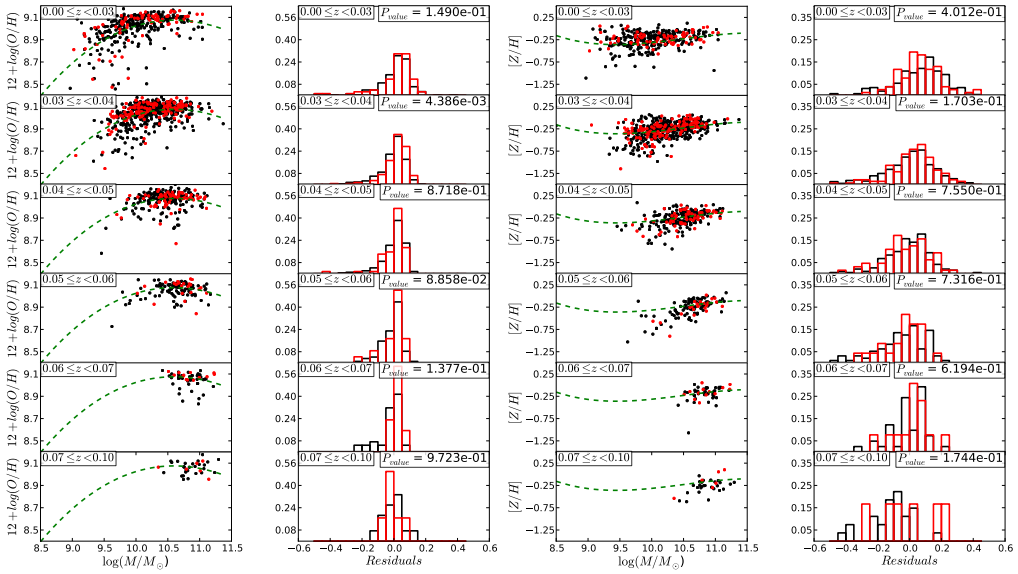

Figure C.2: Differences in the metallicity between barred and unbarred galaxies (red and black, respectively) in the redshift intervals described in the text and shown in top left corner of each panel. Columns 1 and 3 represent gaseous and stellar metallicities as a function of the stellar mass. Green dashed lines represent the polynomial fit to the shole sample points. Columns 2 and 4 represent the distributions of the residuals respect that polynomial fit of for barred and unbarred galaxies and the P-value of the KS test comparing the two distributions.

C.2. Inclination effects

Inclination is also a non-physical magnitude which can affect the results, as the disc contribution to the spectrum depends on the inclination of the galaxy. The inclination is a parameter which can be difficult to determine, owing to particular morphologies in galaxies. Usually the inclination (Nair and Abraham, 2010) is measured considering that the disc is completely flat and null ellipticity (which may not be always true), fitting elliptical isophotes and calculating the axial ratio, b/a, which is related to the inclination of the galaxy. We use this axial ratio as a proxy for the inclination, so we will use indifferently one or the other.

In the source catalogue of our sample (Nair and Abraham, 2010) a lower limit for this ratio is established, so the authors can rely on their determination of the morphology of the galaxies. We take the same lower limit for our sample, but we also check that this limit is valid and the results are robust and independent of the inclination in a similar way as we did for the redshift in Section C.1.

Figure C.3 shows the metallicity as a function of the stellar mass (for both gas and stars) in barred and unbarred galaxies binned according to their inclination. We compare the residuals of the galaxies in each inclination interval respect to a polynomial fit to the whole sample of galaxies. Only in one of the intervals ($0.4 \leq b/a < 0.5$) the unbarred galaxies have a different behaviour (P-value$= 1{,}47 \times 10^{-4}$) than the whole sample, so we have to pay special attention to the differences in this interval.

Following the same procedure as in Section C.1 (and more justified here, because of the different behaviour of unbarred galaxies found before), we analyse the differences in the metallicity in the same inclination intervals. We find that the differences in the metallicity are statistically significant only for galaxies with $0.5 \leq b/a < 0.6$ (P-value $= 1.046 \times 10^{-3}$). In order to check if these galaxies are biasing our results, we repeated the whole analysis considering only galaxies with $0.6 \leq b/a$, and the results do not vary significantly, so we keep the initial selection, using all galaxies with $b/a \geq 0.4$.

In this appendix we conclude that in Chapter 2, the selection criteria concerning redshift and inclination are not biasing our results. However, we think it is convenient to notice that both of them can play a role (but spurious) in the results, so it may be worth investing time in a safety check.

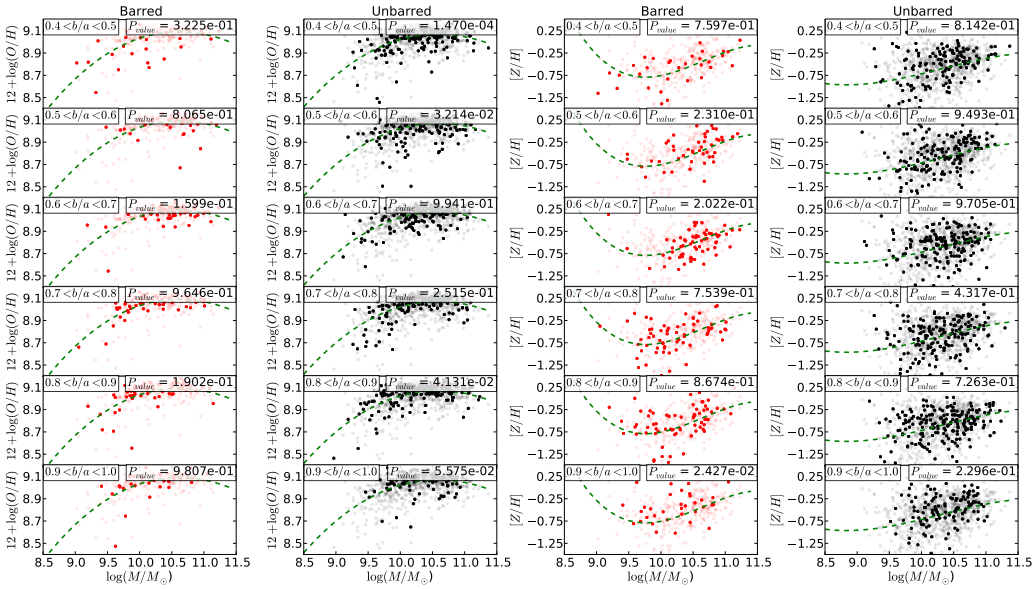

Figure C.3: Mass-metallicity relations for barred (red) and unbarred (black) galaxies for different inclination intervals (shown in the top left corner of each panel). Colours and coding are the same as in Fig. C.1

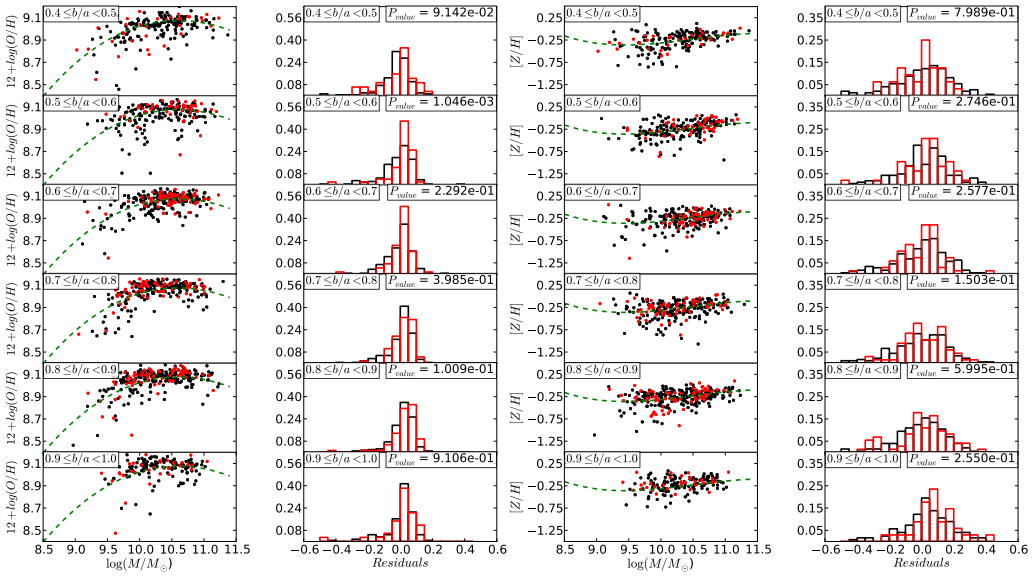

Figure C.4: Differences in the metallicity between barred and unbarred galaxies in each axial ratio interval. Symbols and colors have the same meaning as in Figure C.2

Bibliography

Y as, del mucho leer y del poco dormir,
se le sec el celebro de manera que vino a
perder el juicio.

Miguel de Cervantes Saavedra

Athanassoula, E. Dynamical Evolution Driven by Bars and Interactions: Input from Numerical Simulations. *AP&SS*, vol. 281, pages 39–47, 2002.

Athanassoula, E. On the nature of bulges in general and of box/peanut bulges in particular: input from N-body simulations. *MNRAS*, vol. 358, pages 1477–1488, 2005.

Babusiaux, C., Gómez, A., Hill, V. and 9 coauthors. Insights on the Milky Way bulge formation from the correlations between kinematics and metallicity. *AAP*, vol. 519, page A77, 2010.

Bacon, R., Accardo, M., Adjali, L. and 68 coauthors. The MUSE second-generation VLT instrument. In *Society of Photo-Optical Instrumentation Engineers (SPIE) Conference Series*, vol. 7735 of *Society of Photo-Optical Instrumentation Engineers (SPIE) Conference Series*, page 8. 2010.

Balcells, M. and Peletier, R. F. Colors and color gradients in bulges of galaxies. *AJ*, vol. 107, pages 135–152, 1994.

Baldwin, J. A., Phillips, M. M. and Terlevich, R. Classification parameters for the emission-line spectra of extragalactic objects. *PASP*, vol. 93, pages 5–19, 1981.

Balogh, M. L., Morris, S. L., Yee, H. K. C., Carlberg, R. G. and Ellingson, E. Differential Galaxy Evolution in Cluster and Field Galaxies at z˜0.3. *ApJ*, vol. 527, pages 54–79, 1999.

BELL, E. F. and DE JONG, R. S. The stellar populations of spiral galaxies. *MNRAS*, vol. 312, pages 497–520, 2000.

BENDER, R., BURSTEIN, D. and FABER, S. M. Dynamically hot galaxies. II - Global stellar populations. *ApJ*, vol. 411, pages 153–169, 1993.

BENSBY, T., YEE, J. C., FELTZING, S. and 20 COAUTHORS. Chemical evolution of the Galactic bulge as traced by microlensed dwarf and subgiant stars. V. Evidence for a wide age distribution and a complex MDF. *AAP*, vol. 549, page A147, 2013.

BERENTZEN, I., SHLOSMAN, I. and JOGEE, S. Stellar Bar Evolution in Cuspy and Flat-cored Triaxial CDM Halos. *ApJ*, vol. 637, pages 582–597, 2006.

BÖKER, T., FALCÓN-BARROSO, J., SCHINNERER, E., KNAPEN, J. H. and RYDER, S. A SINFONI View of Galaxy Centers: Morphology and Kinematics of Five Nuclear Star Formation-Rings. *AJ*, vol. 135, pages 479–495, 2008.

BORKOVA, T. V. and MARSAKOV, V. A. A Compiled Catalog of Spectroscopically Determined Elemental Abundances for Stars with Accurate Parallaxes; Magnesium. *Astronomy Reports*, vol. 49, pages 405–416, 2005.

BOURNAUD, F., JOG, C. J. and COMBES, F. Galaxy mergers with various mass ratios: Properties of remnants. *AAP*, vol. 437, pages 69–85, 2005.

BRUZUAL, G. and CHARLOT, S. Stellar population synthesis at the resolution of 2003. *MNRAS*, vol. 344, pages 1000–1028, 2003.

BUTA, R. and BLOCK, D. L. A Dust-penetrated Classification Scheme for Bars as Inferred from Their Gravitational Force Fields. *ApJ*, vol. 550, pages 243–252, 2001.

BUTA, R., CORWIN, H. G., JR. and ODEWAHN, S. C. The de Vaucouleurs Atlas of Galaxies. In *Disks of Galaxies: Kinematics, Dynamics and Peturbations* (edited by E. Athanassoula, A. Bosma and R. Mujica), vol. 275 of *Astronomical Society of the Pacific Conference Series*, page 102. 2002.

CACHO, R., SÁNCHEZ-BLÁZQUEZ, P., GORGAS, J. and PÉREZ, I. Gaseous-phase metallicities and stellar populations in the centres of barred galaxies. *MNRAS*, vol. 442, pages 2496–2510, 2014.

CAPPELLARI, M. and COPIN, Y. Adaptive spatial binning of integral-field spectroscopic data using Voronoi tessellations. *MNRAS*, vol. 342, pages 345–354, 2003.

CAPPELLARI, M. and EMSELLEM, E. Parametric Recovery of Line-of-Sight Velocity Distributions from Absorption-Line Spectra of Galaxies via Penalized Likelihood. *PASP*, vol. 116, pages 138–147, 2004.

CARDIEL, N. *Star Formation in Central Cluster Galaxies*. Doctoral Thesis, , Universidad Complutense de Madrid, Spain, (1999), 1999.

CENARRO, A. J., PELETIER, R. F., SÁNCHEZ-BLÁZQUEZ, P., SELAM, S. O., TOLOBA, E., CARDIEL, N., FALCÓN-BARROSO, J., GORGAS, J., JIMÉNEZ-VICENTE, J. and VAZDEKIS, A. Medium-resolution Isaac Newton Telescope library of empirical spectra - II. The stellar atmospheric parameters. *MNRAS*, vol. 374, pages 664–690, 2007.

CERVANTES, J. L. and VAZDEKIS, A. An optimized Hβ index for disentangling stellar population ages. *MNRAS*, vol. 392, pages 691–704, 2009.

CHAPELON, S., CONTINI, T. and DAVOUST, E. Starbursts in barred spiral galaxies. V. Morphological analysis of bars. *AAP*, vol. 345, pages 81–92, 1999.

CHEN, X., LUO, A. and YANG, H. Stellar population analysis of galaxies in SDSS and LAMOST Pilot Survey. In *IAU Symposium* (edited by S. Feltzing, G. Zhao, N. A. Walton and P. Whitelock), vol. 298 of *IAU Symposium*, pages 399–399. 2014.

CHEUNG, E., ATHANASSOULA, E., MASTERS, K. L. and 10 COAUTHORS. Galaxy Zoo: Observing Secular Evolution through Bars. *ApJ*, vol. 779, page 162, 2013.

CHIAPPINI, C., PELLEGRINI, P. S., RITÉ, C., MAIA, M. A. G., OGANDO, R., RAMOS, B., SCHIAVON, R. P., WILLMER, C. N. A., DA COSTA, L., BERNARDI, M., ALONSO, M. V. and WEGNER, G. Mg_2-σ in Early-Type Galaxies and Spiral Bulges. In *Chemical Enrichment of Intracluster and Intergalactic Medium* (edited by R. Fusco-Femiano and F. Matteucci), vol. 253 of *Astronomical Society of the Pacific Conference Series*, page 321. 2002.

CHILDRESS, M. J., VOGT, F. P. A., NIELSEN, J. and SHARP, R. G. PyWiFeS: a rapid data reduction pipeline for the Wide Field Spectrograph (WiFeS). *ApSS*, vol. 349, pages 617–636, 2014.

CHILINGARIAN, I. *Formation and Evolution of Dwarf Elliptical Galaxies*. Doctoral Thesis, PhD Thesis, 2006, 2006.

CID FERNANDES, R., MATEUS, A., SODRÉ, L., STASIŃSKA, G. and GOMES, J. M. Semi-empirical analysis of Sloan Digital Sky Survey galaxies - I. Spectral synthesis method. *MNRAS*, vol. 358, pages 363–378, 2005.

CLARKSON, W., SAHU, K., ANDERSON, J. and 11 COAUTHORS. Stellar Proper Motions in the Galactic Bulge from Deep Hubble Space Telescope ACS WFC Photometry. *ApJ*, vol. 684, pages 1110–1142, 2008.

COCCATO, L., IODICE, E. and ARNABOLDI, M. Spectral decomposition of the stellar kinematics in the polar disk galaxy NGC 4650A. *AAP*, vol. 569, page A83, 2014.

COCCATO, L., MORELLI, L., CORSINI, E. M., BUSON, L., PIZZELLA, A., VERGANI, D. and BERTOLA, F. Dating the formation of the counter-rotating stellar disc in the spiral galaxy NGC 5719 by disentangling its stellar populations. *MNRAS*, vol. 412, pages L113–L117, 2011.

COCCATO, L., MORELLI, L., PIZZELLA, A., CORSINI, E. M., BUSON, L. M. and DALLA BONTÀ, E. Spectroscopic evidence of distinct stellar populations in the counter-rotating stellar disks of NGC 3593 and NGC 4550. *AAP*, vol. 549, page A3, 2013.

COELHO, P., BRUZUAL, G., CHARLOT, S., WEISS, A., BARBUY, B. and FERGUSON, J. W. Spectral models for solar-scaled and α-enhanced stellar populations. *MNRAS*, vol. 382, pages 498–514, 2007.

COELHO, P. and GADOTTI, D. A. Bars Rejuvenating Bulges? Evidence from Stellar Population Analysis. *ApJL*, vol. 743, page L13, 2011.

CONROY, C. Modeling the Panchromatic Spectral Energy Distributions of Galaxies. *ARAA*, vol. 51, pages 393–455, 2013.

CONSIDÈRE, S., COZIOL, R., CONTINI, T. and DAVOUST, E. Starbursts in barred spiral galaxies. IV. On young bars and the formation of abundance gradients. *AAP*, vol. 356, pages 89–101, 2000.

CROCKER, D. A., BAUGUS, P. D. and BUTA, R. The Distribution and Properties of H II Regions in Early-to-Intermediate Hubble Type Ringed Galaxies. *ApJS*, vol. 105, page 353, 1996.

DADDI, E., BOURNAUD, F., WALTER, F. and 10 COAUTHORS. Very High Gas Fractions and Extended Gas Reservoirs in z = 1.5 Disk Galaxies. *ApJ*, vol. 713, pages 686–707, 2010.

DE JONG, R. S. Near-infrared and optical broadband surface photometry of 86 face-on disk dominated galaxies. III. The statistics of the disk and bulge parameters. *AAP*, vol. 313, pages 45–64, 1996.

DE LORENZO-CÁCERES, A., FALCÓN-BARROSO, J. and VAZDEKIS, A. Distinct stellar populations in the inner bars of double-barred galaxies. *MNRAS*, vol. 431, pages 2397–2418, 2013.

DE SOUZA, R. E., GADOTTI, D. A. and DOS ANJOS, S. BUDDA: A New Two-dimensional Bulge/Disk Decomposition Code for Detailed Structural Analysis of Galaxies. *ApJS*, vol. 153, pages 411–427, 2004.

DE VAUCOULEURS, G. Classification and Morphology of External Galaxies. *Handbuch der Physik*, vol. 53, page 275, 1959.

DEBATTISTA, V. P. and SELLWOOD, J. A. Dynamical Friction and the Distribution of Dark Matter in Barred Galaxies. *ApJl*, vol. 493, page L5, 1998.

DEBATTISTA, V. P. and SELLWOOD, J. A. Constraints from Dynamical Friction on the Dark Matter Content of Barred Galaxies. *ApJ*, vol. 543, pages 704–721, 2000.

DOPITA, M., HART, J., MCGREGOR, P., OATES, P., BLOXHAM, G. and JONES, D. The Wide Field Spectrograph (WiFeS). *APSS*, vol. 310, pages 255–268, 2007.

DOPITA, M., RHEE, J., FARAGE, C. and 10 COAUTHORS. The Wide Field Spectrograph (WiFeS): performance and data reduction. *ApSS*, vol. 327, pages 245–257, 2010.

DUTIL, Y. and ROY, J.-R. Chemical Evidence for Morphological Evolution of Spiral Galaxies. *ApJ*, vol. 516, pages 62–76, 1999.

EDVARDSSON, B., ANDERSEN, J., GUSTAFSSON, B., LAMBERT, D. L., NISSEN, P. E. and TOMKIN, J. The Chemical Evolution of the Galactic Disk - Part One - Analysis and Results. *AAP*, vol. 275, page 101, 1993a.

EDVARDSSON, B., ANDERSEN, J., GUSTAFSSON, B., LAMBERT, D. L., NISSEN, P. E. and TOMKIN, J. The Chemical Evolution of the Galactic Disk - Part Two - Observational Data. *AAPs*, vol. 102, page 603, 1993b.

ELICHE-MORAL, M. C., GONZÁLEZ-GARCÍA, A. C., BALCELLS, M., AGUERRI, J. A. L., GALLEGO, J., ZAMORANO, J. and PRIETO, M. A minor merger origin for stellar inner discs and rings in spiral galaxies. *AAP*, vol. 533, page A104, 2011.

ELLISON, S. L., NAIR, P., PATTON, D. R., SCUDDER, J. M., MENDEL, J. T. and SIMARD, L. The impact of gas inflows on star formation rates and metallicities in barred galaxies. *MNRAS*, vol. 416, pages 2182–2192, 2011.

ELMEGREEN, B. G. Starbursts by gravitational collapse in the inner Lindblad resonance rings of galaxies. *ApJL*, vol. 425, pages L73–L76, 1994.

ERWIN, P. Double-barred galaxies. I. A catalog of barred galaxies with stellar secondary bars and inner disks. *AAP*, vol. 415, pages 941–957, 2004.

ERWIN, P. How large are the bars in barred galaxies? *MNRAS*, vol. 364, pages 283–302, 2005.

ERWIN, P. and SPARKE, L. S. Double Bars, Inner Disks, and Nuclear Rings in Early-Type Disk Galaxies. *AJ*, vol. 124, pages 65–77, 2002.

ERWIN, P., VEGA BELTRÁN, J. C. and BECKMAN, J. E. Stellar Nuclear Rings in Barred Galaxies: Fossils of Past Circumnuclear Starbursts? In *The Central Kiloparsec of Starbursts and AGN: The La Palma Connection* (edited by J. H. Knapen, J. E. Beckman, I. Shlosman and T. J. Mahoney), vol. 249 of *Astronomical Society of the Pacific Conference Series*, page 171. 2001.

FABER, S. M., FRIEL, E. D., BURSTEIN, D. and GASKELL, C. M. Old stellar populations. II - an analysis of K-giant spectra. *ApJS*, vol. 57, pages 711–741, 1985.

FALCÓN-BARROSO, J., BACON, R., BUREAU, M. and 10 COAUTHORS. The SAURON project - VII. Integral-field absorption and emission-line kinematics of 24 spiral galaxy bulges. *MNRAS*, vol. 369, pages 529–566, 2006.

FALCÓN-BARROSO, J., PELETIER, R. F. and BALCELLS, M. Bulges on the Fundamental Plane of early-type galaxies. *MNRAS*, vol. 335, pages 741–752, 2002.

FALCÓN-BARROSO, J., SÁNCHEZ-BLÁZQUEZ, P., VAZDEKIS, A., RICCIARDELLI, E., CARDIEL, N., CENARRO, A. J., GORGAS, J. and PELETIER, R. F. An updated MILES stellar library and stellar population models. *AAP*, vol. 532, page A95, 2011.

FERRARESE, L. and MERRITT, D. A Fundamental Relation between Supermassive Black Holes and Their Host Galaxies. *ApJL*, vol. 539, pages L9–L12, 2000.

FINKELSTEIN, S. L., PAPOVICH, C., DICKINSON, M. and 18 COAUTHORS. A galaxy rapidly forming stars 700 million years after the Big Bang at redshift 7.51. *Nature*, vol. 502, pages 524–527, 2013.

FISHER, D., FRANX, M. and ILLINGWORTH, G. Line Strengths and Line-Strength Gradients in S0 Galaxies. *ApJ*, vol. 459, page 110, 1996.

FISHER, D. B. and DRORY, N. The Structure of Classical Bulges and Pseudobulges: the Link Between Pseudobulges and SÉRSIC Index. *AJ*, vol. 136, pages 773–839, 2008.

FISHER, D. B. and DRORY, N. Bulges of Nearby Galaxies with Spitzer: Scaling Relations in Pseudobulges and Classical Bulges. *ApJ*, vol. 716, pages 942–969, 2010.

FISHER, D. B. and DRORY, N. Demographics of Bulge Types within 11 Mpc and Implications for Galaxy Evolution. *ApJL*, vol. 733, page L47, 2011.

FLORIDO, E., ZURITA, A., PEREZ, I., PEREZ-MONTERO, E., COELHO, P. R. T. and GADOTTI, D. A. Central enhancement of the nitrogen-to-oxygen abundance ratio in barred galaxies. *ArXiv e-prints*, 2015.

FREBEL, A., SIMON, J. D., GEHA, M. and WILLMAN, B. High-Resolution Spectroscopy of Extremely Metal-Poor Stars in the Least Evolved Galaxies: Ursa Major II and Coma Berenices. *ApJ*, vol. 708, pages 560–583, 2010.

FRIEDLI, D., BENZ, W. and KENNICUTT, R. On the influence of bars and star formation on galactic abundance gradients. *ApJL*, vol. 430, pages L105–L108, 1994.

GADOTTI, D. A. Image decomposition of barred galaxies and AGN hosts. *MNRAS*, vol. 384, pages 420–439, 2008.

GADOTTI, D. A. Structural properties of pseudo-bulges, classical bulges and elliptical galaxies: a Sloan Digital Sky Survey perspective. *MNRAS*, vol. 393, pages 1531–1552, 2009.

GADOTTI, D. A. and DE SOUZA, R. E. NGC 4608 and NGC 5701: Barred Galaxies without Disks? *ApJL*, vol. 583, pages L75–L78, 2003.

GADOTTI, D. A. and DE SOUZA, R. E. The Vertical Stellar Kinematics in Face-On Barred Galaxies: Estimating the Ages of Bars. *ApJ*, vol. 629, pages 797–815, 2005.

GADOTTI, D. A. and DE SOUZA, R. E. On the Lengths, Colors, and Ages of 18 Face-on Bars. *ApJS*, vol. 163, pages 270–281, 2006.

GANDA, K., FALCÓN-BARROSO, J., PELETIER, R. F. and 5 COAUTHORS. Late-type galaxies observed with SAURON: two-dimensional stellar and emission-line kinematics of 18 spirals. *MNRAS*, vol. 367, pages 46–78, 2006.

GANDA, K., PELETIER, R. F., MCDERMID, R. M. and 10 COAUTHORS. Absorption-line strengths of 18 late-type spiral galaxies observed with SAURON. *MNRAS*, vol. 380, pages 506–540, 2007.

GARCÍA-BENITO, R., ZIBETTI, S., SÁNCHEZ, S. F. and 75 COAUTHORS. CALIFA, the Calar Alto Legacy Integral Field Area survey. III. Second public data release. *AAP*, vol. 576, page A135, 2015.

GEBHARDT, K., BENDER, R., BOWER, G., DRESSLER, A., FABER, S. M., FILIPPENKO, A. V., GREEN, R., GRILLMAIR, C., HO, L. C., KORMENDY, J., LAUER, T. R., MAGORRIAN, J., PINKNEY, J., RICHSTONE, D. and TREMAINE, S. A Relationship between Nuclear Black Hole Mass and Galaxy Velocity Dispersion. *ApJL*, vol. 539, pages L13–L16, 2000.

GORGAS, J., FABER, S. M., BURSTEIN, D., GONZALEZ, J. J., COURTEAU, S. and PROSSER, C. Old stellar populations. IV - Empirical functions for features in the spectra of G and K stars. *ApJs*, vol. 86, pages 153–198, 1993.

HAMEED, S. and DEVEREUX, N. Hα Imaging of Early-Type (SA-SAB) Spiral Galaxies. I. *AJ*, vol. 118, pages 730–751, 1999.

HAWARDEN, T. G., HUANG, J. H. and GU, Q. S. Infrared Emission from Barred Spiral Galaxies. In *IAU Colloq. 157: Barred Galaxies* (edited by R. Buta, D. A. Crocker and B. G. Elmegreen), vol. 91 of *Astronomical Society of the Pacific Conference Series*, page 54. 1996.

HAWARDEN, T. G., MOUNTAIN, C. M., LEGGETT, S. K. and PUXLEY, P. J. Enhanced star formation - The importance of bars in spiral galaxies. *MNRAS*, vol. 221, pages 41P–45P, 1986.

HENRY, R. B. C. and WORTHEY, G. The Distribution of Heavy Elements in Spiral and Elliptical Galaxies. *PASP*, vol. 111, pages 919–945, 1999.

HERNQUIST, L. An analytical model for spherical galaxies and bulges. *ApJ*, vol. 356, pages 359–364, 1990.

HERNQUIST, L. Structure of merger remnants. I - Bulgeless progenitors. *ApJ*, vol. 400, pages 460–475, 1992.

HO, L. C., FILIPPENKO, A. V. and SARGENT, W. L. W. The Influence of Bars on Nuclear Activity. *ApJ*, vol. 487, page 591, 1997.

HO, L. C., LI, Z.-Y., BARTH, A. J., SEIGAR, M. S. and PENG, C. Y. The Carnegie-Irvine Galaxy Survey. I. Overview and Atlas of Optical Images. *ApJS*, vol. 197, page 21, 2011.

HOLMBERG, J., NORDSTRÖM, B. and ANDERSEN, J. The Geneva-Copenhagen survey of the Solar neighbourhood II. New uvby calibrations and rediscussion of stellar ages, the G dwarf problem, age-metallicity diagram, and heating mechanisms of the disk. *AAP*, vol. 475, pages 519–537, 2007.

HOPKINS, P. F., BUNDY, K., CROTON, D. and 6 COAUTHORS. Mergers and Bulge Formation in ΛCDM: Which Mergers Matter? *ApJ*, vol. 715, pages 202–229, 2010.

HUANG, J. H., GU, Q. S., SU, H. J., HAWARDEN, T. G., LIAO, X. H. and WU, G. X. The bar-enhanced star-formation activities in spiral galaxies. *AAP*, vol. 313, pages 13–24, 1996.

HUMMEL, E., VAN DER HULST, J. M., KENNICUTT, R. C. and KEEL, W. C. Environmental impact on the nuclear radio activity in spiral galaxies. *AAP*, vol. 236, pages 333–345, 1990.

HUNT, L. K., MALKAN, M. A., MORIONDO, G. and SALVATI, M. The Disks of Galaxies with Seyfert and Starburst Nuclei. II. Near-Infrared Structural Properties. *ApJ*, vol. 510, pages 637–650, 1999.

IDIART, T. P., DE FREITAS PACHECO, J. A. and COSTA, R. D. D. Metallicity Indices for Multi-Population Models.II.Bulges of Galaxies. *AJ*, vol. 112, page 2541, 1996.

JABLONKA, P., GORGAS, J. and GOUDFROOIJ, P. Stellar population gradients in bulges along the Hubble sequence. II. Relations with galaxy properties. *AAP*, vol. 474, pages 763–776, 2007.

JOGEE, S. The Fueling and Evolution of AGN: Internal and External Triggers. In *Physics of Active Galactic Nuclei at all Scales* (edited by D. Alloin), vol. 693 of *Lecture Notes in Physics, Berlin Springer Verlag*, page 143. 2006.

JOGEE, S., KENNEY, J. D. P. and SMITH, B. J. A Gas-rich Nuclear Bar Fueling a Powerful Central Starburst in NGC 2782. *ApJ*, vol. 526, pages 665–682, 1999.

JOGEE, S., SCOVILLE, N. and KENNEY, J. D. P. The Central Region of Barred Galaxies: Molecular Environment, Starbursts, and Secular Evolution. *ApJ*, vol. 630, pages 837–863, 2005.

JOHNSON, C. I., RICH, R. M., FULBRIGHT, J. P., VALENTI, E. and MCWILLIAM, A. Alpha Enhancement and the Metallicity Distribution Function of Plaut's Window. *ApJ*, vol. 732, page 108, 2011.

JOHNSTON, E. J., MERRIFIELD, M. R., ARAGÓN-SALAMANCA, A. and CAPPELLARI, M. Disentangling the stellar populations in the counter-rotating disc galaxy NGC 4550. *MNRAS*, vol. 428, pages 1296–1302, 2013.

JORGENSEN, I., FRANX, M. and KJAERGAARD, P. The Fundamental Plane for cluster E and S0 galaxies. *MNRAS*, vol. 280, pages 167–185, 1996.

KAUFFMANN, G., HECKMAN, T. M., TREMONTI, C. and 10 COAUTHORS. The host galaxies of active galactic nuclei. *MNRAS*, vol. 346, pages 1055–1077, 2003a.

KAUFFMANN, G., HECKMAN, T. M., WHITE, S. D. M. and 19 COAUTHORS. Stellar masses and star formation histories for 10^5 galaxies from the Sloan Digital Sky Survey. *MNRAS*, vol. 341, pages 33–53, 2003b.

KEWLEY, L. J. and DOPITA, M. A. Using Strong Lines to Estimate Abundances in Extragalactic H II Regions and Starburst Galaxies. *ApJS*, vol. 142, pages 35–52, 2002.

KEWLEY, L. J., DOPITA, M. A., SUTHERLAND, R. S., HEISLER, C. A. and TREVENA, J. Theoretical Modeling of Starburst Galaxies. *ApJ*, vol. 556, pages 121–140, 2001.

KEWLEY, L. J. and ELLISON, S. L. Metallicity Calibrations and the Mass-Metallicity Relation for Star-forming Galaxies. *ApJ*, vol. 681, pages 1183–1204, 2008.

KNAPEN, J. H., BECKMAN, J. E., HELLER, C. H., SHLOSMAN, I. and DE JONG, R. S. The Central Region in M100: Observations and Modeling. *ApJ*, vol. 454, page 623, 1995.

KOLEVA, M., PRUGNIEL, P., BOUCHARD, A. and WU, Y. ULySS: a full spectrum fitting package. *AAP*, vol. 501, pages 1269–1279, 2009.

KOLEVA, M., PRUGNIEL, P. and DE RIJCKE, S. Sigma-drop in galaxies and the sigma-metallicity degeneracy. *Astronomische Nachrichten*, vol. 329, page 968, 2008a.

KOLEVA, M., PRUGNIEL, P., OCVIRK, P., LE BORGNE, D. and SOUBIRAN, C. Spectroscopic ages and metallicities of stellar populations: validation of full spectrum fitting. *MNRAS*, vol. 385, pages 1998–2010, 2008b.

KORMENDY, J. and KENNICUTT, R. C., JR. Secular Evolution and the Formation of Pseudobulges in Disk Galaxies. *ARAA*, vol. 42, pages 603–683, 2004.

KROUPA, P. On the variation of the initial mass function. *MNRAS*, vol. 322, pages 231–246, 2001.

KUNTSCHNER, H. The stellar populations of early-type galaxies in the Fornax cluster. *MNRAS*, vol. 315, pages 184–208, 2000.

LAURIKAINEN, E., SALO, H., BUTA, R. and KNAPEN, J. H. Properties of bars and bulges in the Hubble sequence. *MNRAS*, vol. 381, pages 401–417, 2007.

LE BORGNE, D., ROCCA-VOLMERANGE, B., PRUGNIEL, P., LANÇON, A., FIOC, M. and SOUBIRAN, C. Evolutionary synthesis of galaxies at high spectral resolution with the code PEGASE-HR. Metallicity and age tracers. *AAP*, vol. 425, pages 881–897, 2004.

LE BORGNE, J.-F., BRUZUAL, G., PELLÓ, R. and 6 COAUTHORS. STELIB: A library of stellar spectra at R ˜ 2000. *AAP*, vol. 402, pages 433–442, 2003.

LI, Z.-Y., HO, L. C., BARTH, A. J. and PENG, C. Y. The Carnegie-Irvine Galaxy Survey. II. Isophotal Analysis. *ApJS*, vol. 197, page 22, 2011.

LISKER, T., DEBATTISTA, V. P., FERRERAS, I. and ERWIN, P. Double-barred galaxies at intermediate redshifts: a feasibility study. *MNRAS*, vol. 370, pages 477–487, 2006.

MacArthur, L. A., Courteau, S., Bell, E. and Holtzman, J. A. Structure of Disk-dominated Galaxies. II. Color Gradients and Stellar Population Models. *ApJS*, vol. 152, pages 175–199, 2004.

MacArthur, L. A., González, J. J. and Courteau, S. Stellar population and kinematic profiles in spiral bulges and discs: population synthesis of integrated spectra. *MNRAS*, vol. 395, pages 28–63, 2009.

Madau, P., Ferguson, H. C., Dickinson, M. E., Giavalisco, M., Steidel, C. C. and Fruchter, A. High-redshift galaxies in the Hubble Deep Field: colour selection and star formation history to z˜4. *MNRAS*, vol. 283, pages 1388–1404, 1996.

Magris C., G., Bruzual A., G. and Mateu, J. Uncertainties in the galaxy mass and age determination from inverse population synthesis models. In *Revista Mexicana de Astronomia y Astrofisica Conference Series*, vol. 40 of *Revista Mexicana de Astronomia y Astrofisica, vol. 27*, pages 66–67. 2011.

Martel, H., Kawata, D. and Ellison, S. L. The connection between star formation and metallicity evolution in barred spiral galaxies. *MNRAS*, vol. 431, pages 2560–2575, 2013.

Martin, P. Quantitative Morphology of Bars in Spiral Galaxies. *AJ*, vol. 109, page 2428, 1995.

Martin, P. and Friedli, D. Star formation in bar environments. I. Morphology, star formation rates and general properties. *AAP*, vol. 326, pages 449–464, 1997.

Martinet, L. and Friedli, D. Bar strength and star formation activity in late-type barred galaxies. *AAP*, vol. 323, pages 363–373, 1997.

Méndez-Abreu, J., Debattista, V. P., Corsini, E. M. and Aguerri, J. A. L. Secular- and merger-built bulges in barred galaxies. *AAP*, vol. 572, page A25, 2014.

Mighell, K. J. Parameter Estimation in Astronomy with Poisson-distributed Data. I.The χ^2 Statistic. *ApJ*, vol. 518, pages 380–393, 1999.

Mighell, K. J. Parameter Estimation in Astronomy with Poisson-Distributed Data. II. The Modified Chi-Square-Gamma Statistic. *ArXiv Astrophysics e-prints*, 2000.

MILONE, A. D. C., SANSOM, A. E. and SÁNCHEZ-BLÁZQUEZ, P. Element abundances in the stars of the MILES spectral library: the Mg/Fe ratio. *MNRAS*, vol. 414, pages 1227–1252, 2011.

MOORTHY, B. K. and HOLTZMAN, J. A. Stellar populations in bulges of spiral galaxies. *MNRAS*, vol. 371, pages 583–608, 2006.

MORELLI, L., CORSINI, E. M., PIZZELLA, A., DALLA BONTÀ, E., COCCATO, L., MÉNDEZ-ABREU, J. and CESETTI, M. Structure and dynamics of galaxies with a low surface-brightness disc - II. Stellar populations of bulges. *MNRAS*, vol. 423, pages 962–982, 2012.

MORELLI, L., POMPEI, E., PIZZELLA, A., MÉNDEZ-ABREU, J., CORSINI, E. M., COCCATO, L., SAGLIA, R. P., SARZI, M. and BERTOLA, F. Stellar populations of bulges in 14 cluster disc galaxies. *MNRAS*, vol. 389, pages 341–363, 2008.

MOULTAKA, J., BOISSON, C., JOLY, M. and PELAT, D. Constraining the solutions of an inverse method of stellar population synthesis. *AAP*, vol. 420, pages 459–466, 2004.

MOULTAKA, J. and PELAT, D. Error analysis for stellar population synthesis as an inverse problem. *MNRAS*, vol. 314, pages 409–419, 2000.

MUÑOZ-MATEOS, J. C., GIL DE PAZ, A., BOISSIER, S., ZAMORANO, J., JARRETT, T., GALLEGO, J. and MADORE, B. F. Specific Star Formation Rate Profiles in Nearby Spiral Galaxies: Quantifying the Inside-Out Formation of Disks. *ApJ*, vol. 658, pages 1006–1026, 2007.

NAIR, P. B. and ABRAHAM, R. G. A Catalog of Detailed Visual Morphological Classifications for 14,034 Galaxies in the Sloan Digital Sky Survey. *ApJS*, vol. 186, pages 427–456, 2010.

NESS, M., FREEMAN, K., ATHANASSOULA, E. and 8 COAUTHORS. The Origin of the Split Red Clump in the Galactic Bulge of the Milky Way. *ApJ*, vol. 756, page 22, 2012.

NORDSTRÖM, B., MAYOR, M., ANDERSEN, J., HOLMBERG, J., PONT, F., JØRGENSEN, B. R., OLSEN, E. H., UDRY, S. and MOWLAVI, N. The Geneva-Copenhagen survey of the Solar neighbourhood. Ages, metallicities, and kinematic properties of $\sim$ 14 000 F and G dwarfs. *AAP*, vol. 418, pages 989–1019, 2004.

NORMAN, C. A. and SPAANS, M. Molecules at High Redshift: The Evolution of the Cool Phase of Protogalactic Disks. *ApJ*, vol. 480, pages 145–154, 1997.

OBREJA, A., DOMÍNGUEZ-TENREIRO, R., BROOK, C. and 5 COAUTHORS. A Two-phase Scenario for Bulge Assembly in ΛCDM Cosmologies. *ApJ*, vol. 763, page 26, 2013.

OCVIRK, P., PELETIER, R. and LANÇON, A. Extragalactic archeology in integrated light: A test case with NGC 4030. *Astronomische Nachrichten*, vol. 329, page 980, 2008.

OCVIRK, P., PICHON, C., LANÇON, A. and THIÉBAUT, E. STECKMAP: STEllar Content and Kinematics from high resolution galactic spectra via Maximum A Posteriori. *MNRAS*, vol. 365, pages 74–84, 2006a.

OCVIRK, P., PICHON, C., LANÇON, A. and THIÉBAUT, E. STECMAP: STEllar Content from high-resolution galactic spectra via Maximum A Posteriori. *MNRAS*, vol. 365, pages 46–73, 2006b.

OH, K., SARZI, M., SCHAWINSKI, K. and YI, S. K. Improved and Quality-assessed Emission and Absorption Line Measurements in Sloan Digital Sky Survey Galaxies. *ApJS*, vol. 195, page 13, 2011.

OKAMOTO, T. The origin of pseudo-bulges in cosmological simulations of galaxy formation. *MNRAS*, vol. 428, pages 718–728, 2013.

ORTOLANI, S., RENZINI, A., GILMOZZI, R., MARCONI, G., BARBUY, B., BICA, E. and RICH, R. M. Near-coeval formation of the Galactic bulge and halo inferred from globular cluster ages. *Nature*, vol. 377, pages 701–704, 1995.

PELETIER, R. F. and BALCELLS, M. Ages of Galaxies Bulges and Disks From Optical and Near-Infrared Colors. *AJ*, vol. 111, page 2238, 1996.

PELETIER, R. F., FALCÓN-BARROSO, J., BACON, R. and 10 COAUTHORS. The SAURON project - XI. Stellar populations from absorption-line strength maps of 24 early-type spirals. *MNRAS*, vol. 379, pages 445–468, 2007.

PÉREZ, I. and SÁNCHEZ-BLÁZQUEZ, P. Study of stellar populations in the bulges of barred galaxies. *AAP*, vol. 529, page A64, 2011.

PÉREZ, I., SÁNCHEZ-BLÁZQUEZ, P. and ZURITA, A. Study of the stellar line-strength indices and kinematics along bars. I. Bar age and metallicity gradients. *AAP*, vol. 495, pages 775–794, 2009.

PFENNIGER, D. and FRIEDLI, D. Structure and dynamics of 3D N-body barred galaxies. *AAP*, vol. 252, pages 75–93, 1991.

PICHON, C., SIEBERT, A. and BIENAYMÉ, O. On the kinematic deconvolution of the local neighbourhood luminosity function. *MNRAS*, vol. 329, pages 181–194, 2002.

PILYUGIN, L. S., LARA-LÓPEZ, M. A., GREBEL, E. K., KEHRIG, C., ZINCHENKO, I. A., LÓPEZ-SÁNCHEZ, Á. R., VÍLCHEZ, J. M. and MATTSSON, L. The metallicity-redshift relations for emission-line SDSS galaxies: examination of the dependence on the star formation rate. *MNRAS*, vol. 432, pages 1217–1230, 2013.

POMPEA, S. M. and RIEKE, G. H. Are bars essential for starbursts in noninteracting galaxies. In *NASA Conference Publication* (edited by D. J. Hollenbach and H. A. Thronson, Jr.), vol. 3084 of *NASA Conference Publication*, pages 305–306. 1990.

PROCTOR, R. N. and SANSOM, A. E. A comparison of stellar populations in galaxy spheroids across a wide range of Hubble types. *MNRAS*, vol. 333, pages 517–543, 2002.

PRUGNIEL, P. and SOUBIRAN, C. A database of high and medium-resolution stellar spectra. *AAP*, vol. 369, pages 1048–1057, 2001.

PRUGNIEL, P., SOUBIRAN, C., KOLEVA, M. and LE BORGNE, D. VizieR Online Data Catalog: ELODIE library V3.1 (Prugniel+ 2007). *VizieR Online Data Catalog*, vol. 3251, page 0, 2007.

REGAN, M. W. and TEUBEN, P. J. Bar-driven Mass Inflow: How Bar Characteristics Affect the Inflow. *ApJ*, vol. 600, pages 595–612, 2004.

ROEDIGER, J. C. and COURTEAU, S. On the uncertainties of stellar mass estimates via colour measurements. *MNRAS*, vol. 452, pages 3209–3225, 2015.

ROEDIGER, J. C., COURTEAU, S., SÁNCHEZ-BLÁZQUEZ, P. and MCDONALD, M. Stellar Populations and Radial Migrations in Virgo Disk Galaxies. *ApJ*, vol. 758, page 41, 2012.

SÁNCHEZ, S. F., GARCÍA-LORENZO, B., JAHNKE, K., MEDIAVILLA, E., GONZÁLEZ-SERRANO, J. I., CHRISTENSEN, L. and WISOTZKI, L. Decoupling the host and nuclear spectra of type I AGNs using integral field spectroscopy: A test on 3C 120. *NAR*, vol. 49, pages 501–507, 2006.

SÁNCHEZ, S. F., KENNICUTT, R. C., GIL DE PAZ, A. and 69 COAUTHORS. CALIFA, the Calar Alto Legacy Integral Field Area survey. I. Survey presentation. *AAP*, vol. 538, page A8, 2012.

SANCHEZ-BLAZQUEZ, P. *Star Formation History of early-type galaxies in different environments*. Doctoral Thesis, Universidad Complutense de Madrid, Spain, 2004.

SÁNCHEZ-BLÁZQUEZ, P., COURTY, S., GIBSON, B. K. and BROOK, C. B. The origin of the light distribution in spiral galaxies. *MNRAS*, vol. 398, pages 591–606, 2009.

SÁNCHEZ-BLÁZQUEZ, P., GORGAS, J., CARDIEL, N. and GONZÁLEZ, J. J. Stellar populations of early-type galaxies in different environments. I. Line-strength indices. Relations of line-strengths with σ. *AAP*, vol. 457, pages 787–808, 2006a.

SÁNCHEZ-BLÁZQUEZ, P., OCVIRK, P., GIBSON, B. K., PÉREZ, I. and PELETIER, R. F. Star formation history of barred disc galaxies. *MNRAS*, vol. 415, pages 709–731, 2011.

SÁNCHEZ-BLÁZQUEZ, P., PELETIER, R. F., JIMÉNEZ-VICENTE, J. and 6 COAUTHORS. Medium-resolution Isaac Newton Telescope library of empirical spectra. *MNRAS*, vol. 371, pages 703–718, 2006b.

SÁNCHEZ-BLÁZQUEZ, P., ROSALES-ORTEGA, F., DIAZ, A. and SÁNCHEZ, S. F. PPAK Wide field Integral Field Spectroscopy of NGC 628 - III. Stellar population properties. *MNRAS*, vol. 437, pages 1534–1548, 2014.

SANSOM, A. E., PROCTOR, R. N. and REID, N. Abundances in Spiral Bulges: Comparisons with Ellipticals. In *Abundance Profiles: Diagnostic Tools for Galaxy History* (edited by D. Friedli, M. Edmunds, C. Robert and L. Drissen), vol. 147 of *ASPC*, page 26. 1998.

SARZI, M., FALCÓN-BARROSO, J., DAVIES, R. L. and 10 COAUTHORS. The SAURON project - V. Integral-field emission-line kinematics of 48 elliptical and lenticular galaxies. *MNRAS*, vol. 366, pages 1151–1200, 2006.

SCHWARZ, G. Estimating the dimension of a model. *Ann. Statist.*, vol. 6(2), pages 461–464, 1978.

SEIDEL, M. K., CACHO, R., RUIZ-LARA, T. and 7 COAUTHORS. Dissecting galactic bulges in space and time - I. The importance of early formation scenarios versus secular evolution. *MNRAS*, vol. 446, pages 2837–2860, 2015.

SERRA, P. and TRAGER, S. C. On the interpretation of the age and chemical composition of composite stellar populations determined with line-strength indices. *MNRAS*, vol. 374, pages 769–774, 2007.

SIL'CHENKO, O. K. Stellar population properties in the nuclei and bulges of nearby lenticular galaxies. In *The Interplay Among Black Holes, Stars and ISM in Galactic Nuclei* (edited by T. Storchi-Bergmann, L. C. Ho and H. R. Schmitt), vol. 222 of *IAU Symposium*, pages 211–212. 2004.

SIMKIN, S. M., SU, H. J. and SCHWARZ, M. P. Nearby Seyfert galaxies. *ApJ*, vol. 237, pages 404–413, 1980.

SPAANS, M. and CAROLLO, C. M. Star Formation and Metal Production as a Function of Redshift: The Role of the Multiphase ISM. *ApJL*, vol. 482, pages L93–L96, 1997.

STOEHR, F., WHITE, R., SMITH, M., KAMP, I. and 13 COAUTHORS. DER-SNR: A Simple and General Spectroscopic Signal-to-Noise Measurement Algorithm. In *Astronomical Data Analysis Software and Systems XVII* (edited by R. W. Argyle, P. S. Bunclark and J. R. Lewis), vol. 394 of *Astronomical Society of the Pacific Conference Series*, page 505. 2008.

TERNDRUP, D. M., DAVIES, R. L., FROGEL, J. A., DEPOY, D. L. and WELLS, L. A. Infrared imaging of spiral galaxies: Colors and luminosity profiles. *ApJ*, vol. 432, pages 518–546, 1994.

THOMAS, D., MARASTON, C. and BENDER, R. New clues on the calcium underabundance in early-type galaxies. *MNRAS*, vol. 343, pages 279–283, 2003.

THOMAS, D., MARASTON, C., BENDER, R. and MENDES DE OLIVEIRA, C. The Epochs of Early-Type Galaxy Formation as a Function of Environment. *ApJ*, vol. 621, pages 673–694, 2005.

TOLSTOY, E., HILL, V. and TOSI, M. Star-Formation Histories, Abundances, and Kinematics of Dwarf Galaxies in the Local Group. *ARAA*, vol. 47, pages 371–425, 2009.

TRAGER, S. C., FABER, S. M., WORTHEY, G. and GONZÁLEZ, J. J. The Stellar Population Histories of Early-Type Galaxies. II. Controlling Parameters of the Stellar Populations. *AJ*, vol. 120, pages 165–188, 2000.

TREMONTI, C. A., HECKMAN, T. M., KAUFFMANN, G., BRINCHMANN, J., CHARLOT, S., WHITE, S. D. M., SEIBERT, M., PENG, E. W., SCHLEGEL, D. J., UOMOTO, A., FUKUGITA, M. and BRINKMANN, J. The Origin of the Mass-Metallicity Relation: Insights from 53,000 Star-forming Galaxies in the Sloan Digital Sky Survey. *ApJ*, vol. 613, pages 898–913, 2004.

VALDES, F., GUPTA, R., ROSE, J. A., SINGH, H. P. and BELL, D. J. The Indo-US Library of Coudé Feed Stellar Spectra. *ApJS*, vol. 152, pages 251–259, 2004.

VALE ASARI, N., STASIŃSKA, G., CID FERNANDES, R., GOMES, J. M., SCHLICKMANN, M., MATEUS, A. and SCHOENELL, W. The evolution of the mass-metallicity relation in SDSS galaxies uncovered by astropaleontology. *MNRAS*, vol. 396, pages L71–L75, 2009.

VAZDEKIS, A., CENARRO, A. J., GORGAS, J., CARDIEL, N. and PELETIER, R. F. Empirical calibration of the near-infrared CaII triplet - IV. The stellar population synthesis models. *MNRAS*, vol. 340, pages 1317–1345, 2003.

VAZDEKIS, A., SÁNCHEZ-BLÁZQUEZ, P., FALCÓN-BARROSO, J. and 5 COAUTHORS. Evolutionary stellar population synthesis with MILES - I. The base models and a new line index system. *MNRAS*, vol. 404, pages 1639–1671, 2010.

WALCHER, C. J., WISOTZKI, L., BEKERAITÉ, S. and 48 COAUTHORS. CALIFA: a diameter-selected sample for an integral field spectroscopy galaxy survey. *AAP*, vol. 569, page A1, 2014.

WEINBERG, M. D. Evolution of barred galaxies by dynamical friction. *MNRAS*, vol. 213, pages 451–471, 1985.

WEINZIRL, T., JOGEE, S., KHOCHFAR, S., BURKERT, A. and KORMENDY, J. Bulge n and B/T in High-Mass Galaxies: Constraints on the Origin of Bulges in Hierarchical Models. *ApJ*, vol. 696, pages 411–447, 2009.

WHITE, S. D. M. and REES, M. J. Core condensation in heavy halos - A two-stage theory for galaxy formation and clustering. *MNRAS*, vol. 183, pages 341–358, 1978.

WILLIAMS, M. J., BUREAU, M. and KUNTSCHNER, H. Secular evolution in action: central values and radial trends in the stellar populations of boxy bulges. *MNRAS*, vol. 427, pages L99–L103, 2012.

WORTHEY, G., FABER, S. M., GONZALEZ, J. J. and BURSTEIN, D. Old stellar populations. 5: Absorption feature indices for the complete LICK/IDS sample of stars. *ApJS*, vol. 94, pages 687–722, 1994.

WORTHEY, G. and OTTAVIANI, D. L. H gamma and H delta Absorption Features in Stars and Stellar Populations. *ApJS*, vol. 111, page 377, 1997.

ZOCCALI, M., LECUREUR, A., BARBUY, B. and 6 COAUTHORS. Oxygen abundances in the Galactic bulge: evidence for fast chemical enrichment. *AAP*, vol. 457, pages L1–L4, 2006.